



12-2008

## Calculations of K-Shell Fluorescence Yields and Photoabsorption Cross Sections for Carbon Ions at the K-Edge

Muhammet Fatih Hasoglu  
*Western Michigan University*

Follow this and additional works at: <https://scholarworks.wmich.edu/dissertations>

 Part of the Physics Commons

---

### Recommended Citation

Hasoglu, Muhammet Fatih, "Calculations of K-Shell Fluorescence Yields and Photoabsorption Cross Sections for Carbon Ions at the K-Edge" (2008). *Dissertations*. 776.  
<https://scholarworks.wmich.edu/dissertations/776>

This Dissertation-Open Access is brought to you for free and open access by the Graduate College at ScholarWorks at WMU. It has been accepted for inclusion in Dissertations by an authorized administrator of ScholarWorks at WMU. For more information, please contact [wmu-scholarworks@wmich.edu](mailto:wmu-scholarworks@wmich.edu).



CALCULATIONS OF K-SHELL FLUORESCENCE YIELDS AND PHOTOAB-  
SORPTION CROSS SECTIONS FOR CARBON IONS AT THE K-EDGE

by

Muhammet Fatih Hasoglu

A Dissertation  
Submitted to the  
Faculty of The Graduate College  
in partial fulfillment of the  
requirements for the  
Degree of Doctor of Philosophy  
Department of Physics  
Dr. Thomas W. Gorczyca, Advisor

Western Michigan University  
Kalamazoo, Michigan  
December 2008

UMI Number: 3340188

### INFORMATION TO USERS

The quality of this reproduction is dependent upon the quality of the copy submitted. Broken or indistinct print, colored or poor quality illustrations and photographs, print bleed-through, substandard margins, and improper alignment can adversely affect reproduction.

In the unlikely event that the author did not send a complete manuscript and there are missing pages, these will be noted. Also, if unauthorized copyright material had to be removed, a note will indicate the deletion.

**UMI**<sup>®</sup>

---

UMI Microform 3340188

Copyright 2009 by ProQuest LLC.

All rights reserved. This microform edition is protected against unauthorized copying under Title 17, United States Code.

ProQuest LLC  
789 E. Eisenhower Parkway  
PO Box 1346  
Ann Arbor, MI 48106-1346

Copyright by  
Muhammet Fatih Hasoglu  
2008

## ACKNOWLEDGMENTS

I would like to express my sincere gratitude to my advisor Prof. Thomas W. Gorczyca. I am in debt to him for his guidance, helpful comments, and his support during my dissertation. Without his support and encouragement, this work would not be possible. I would also like to thank Prof. Zikri Altun at Marmara University who guided me in atomic physics and persuaded me to come to WMU. I am grateful to my dissertation committee members for reviewing this dissertation and their valuable comments. I have learned a lot from Prof. Dean Halderson from the classes that he taught and valuable discussions on quantum and atomic physics. I also thank Prof. Steven Manson and Prof. Nigel Badnell for playing an important role in our fluorescence studies, Prof. Kirk Korista for his collaboration in our atomic physics research as an astrophysicist, and for discussing the important astrophysical phenomenon, and Prof. Nora Berrah for stimulating our interest in K-shell processes from an experimental point of view. I also want to thank my office mates Shahin Abdel-Naby and Dr. Dragan Nikolic for sharing their knowledge and their valuable comments.

The greatest thanks goes to, first, my parents and relatives for their continuous support, and second and most importantly, my lovely wife Nazik for her infinite patience while taking care of our two young twin boys during this long road for obtaining my Ph.D.

Muhammet Fatih Hasoglu

## TABLE OF CONTENTS

ACKNOWLEDGMENTS .....	ii
LIST OF TABLES .....	v
LIST OF FIGURES .....	vii
CHAPTER	
I INTRODUCTION .....	1
1.1 Overview .....	1
1.2 K-Shell Fluorescence Yields .....	3
1.3 K-Shell Photoabsorption Cross Sections .....	6
II THEORETICAL METHODOLOGY .....	9
2.1 Many-Body Atomic Description .....	10
2.1.1 Non-Relativistic Hamiltonian, Wave Function, and Schrödinger Equation .....	10
2.1.2 Relativistic Corrections .....	15
2.1.3 Relevant Atomic Transitions: Auger and Radiative Rates .....	18
2.2 Approximate Many-Body Wave Functions .....	21
2.2.1 Exchange, Antisymmetry, and Slater Determinants .....	21
2.2.2 Variational Method .....	22
2.2.3 Hartree-Fock and Hartree-Slater Methods for Bound States .....	24
2.2.4 Configuration Interaction .....	29

Table of Contents – Continued

CHAPTER	
2.2.5	Distorted Wave Approximation for Continuum Orbitals . . . . . 31
2.3	Multi-Configuration Breit-Pauli Method . . . . . 32
2.4	R-Matrix Method . . . . . 33
2.4.1	Smith Time-Delay Method . . . . . 39
III	RESULTS AND DISCUSSIONS . . . . . 40
3.1	K-Shell Fluorescence Yields for Isoelectronic Sequences . . . . . 40
3.1.1	Li-Like: Importance of Configuration Interaction . . . . . 40
3.1.2	B-Like: Breakdown of Configuration-Average Approximation . . . . . 44
3.1.3	C-Like: Anomalous Behavior . . . . . 48
3.1.4	Comprehensive 2 <sup>nd</sup> -Row Isoelectronic-Sequence Calculations . . . . . 56
3.2	Carbon K-Shell Photoabsorption Cross Section Results . . . . . 59
3.2.1	C: Abundant in the Interstellar Medium . . . . . 59
3.2.2	C <sup>+</sup> : Comparison with Laboratory Experiment . . . . . 64
3.2.3	C <sup>2+</sup> : Importance of Auger Broadening . . . . . 72
IV	SUMMARY AND FUTURE DIRECTIONS . . . . . 79
APPENDICES	
A	Atomic Units . . . . . 81
B	Z-Scaling of Relevant Physical Variables . . . . . 83
BIBLIOGRAPHY	. . . . . 89

## LIST OF TABLES

3.1	Fluorescence yield $\omega_K$ vs. nuclear charge $Z$ for the intermediate-coupling, CI-mixed Li-like $1s2s^2(^2S_{1/2})$ state. ....	44
3.2	Comparison of radiative rates in length and velocity gauge results of MCBP and MCDF calculations for ten levels of the $1s2s^22p^3$ C-like ions with selected nuclear charge, $Z$ . ....	52
3.3	The total K-shell radiative and Auger rates for the $1s2s^22p^5$ O-like isoelectronic sequence. ....	58
3.4	Criterion for determination of $C^+$ physical $1s$ , $2s$ , and $2p$ orbitals and correlation (or pseudo) $\overline{3s}$ , $\overline{3p}$ , and $\overline{3d}$ orbitals. ....	60
3.5	Comparison of Auger widths for the 17 $C^+$ autoionizing target states above the K-shell threshold. ....	62
3.6	Comparison of energies of the relevant C and $C^+$ states involved in the present investigation. ....	63
3.7	Criterion for determination of $C^{2+}$ physical $1s$ , $2s$ , and $2p$ orbitals and correlation (or pseudo) $\overline{3s}$ , $\overline{3p}$ , and $\overline{3d}$ orbitals. ....	65
3.8	Comparison of energies of the relevant $C^+$ and $C^{2+}$ states involved in the present investigation. ....	67
3.9	Same as Table 3.8, showing the $C^+$ metastable ground and K-shell excited states. ....	68
3.10	Comparison of Auger widths for the relevant $C^{2+}$ target states above the K-shell resonantly-excited states. ....	70
3.11	Criterion for determination of $C^{3+}$ physical $1s$ , $2s$ , and $2p$ orbitals and correlation (or pseudo) $\overline{3s}$ , $\overline{3p}$ , and $\overline{3d}$ orbitals. ....	73
3.12	Comparison of energies of the relevant $C^{2+}$ and $C^{3+}$ states involved in the present investigation. ....	73

List of Tables –Continued

3.13	Same as Table 3.12, showing the $C^{2+}$ metastable ground and K-shell excited states. ....	74
3.14	Auger width results obtained from different methods for the thresholds above the K-shell excited states.....	75

## LIST OF FIGURES

1.1	Relevant K-shell X-ray processes. ....	2
1.2	Hydrogenic behavior of the K-shell fluorescence yield as a function of nuclear charge $Z$ for three typical values of the ratio $a$ . ....	4
1.3	Observed X-ray spectrum of the bright extra-galactic X-ray source Blazar Mkn 421 near the carbon K-edge obtained from the Chandra X-ray Observatory. ....	7
3.1	Calculated fluorescence yields (circles) and fit formula (dashed line) for K-shell vacancy Li-like ions. ....	43
3.2	LSJ-dependent fluorescence yields for K-shell vacancy B-like ions. Comparison of fluorescence yields for ${}^2D_{3/2}$ and ${}^2D_{5/2}$ states. ....	46
3.3	LSJ-dependent fluorescence yields for K-shell vacancy of C-like ions. ....	49
3.4	Calculated MCDF (left) and MCBP (right) radiative rates $A_r$ for the ten K-shell vacancy levels $1s2s^22p^3({}^{2S+1}L_J)$ of the C-like isoelectronic sequence. ....	51
3.5	Calculated MCDF (left) and MCBP (right) Auger rates $A_a$ for the ten K-shell vacancy levels $1s2s^22p^3({}^{2S+1}L_J)$ of the C-like isoelectronic sequence. ....	51
3.6	The anomalous behavior of the fluorescence yields for ${}^3S_1$ and ${}^3P_1$ levels. ...	54
3.7	Calculated K-shell photoabsorption cross section of carbon at the K-edge in length and velocity gauges are compared to IP approximation results. ...	61
3.8	The $1s \rightarrow 2p$ photoabsorption for an admixture of 80% ground-state and 20% metastable state $C^+$ ions. ....	69
3.9	Calculated K-shell photoabsorption cross section for the ground state of $C^+$ at the K-edge compared to the oft-used, resonance-omitted, IP approximation results. ....	71

List of Figures – Continued

3.10	Experimental measurements and present and earlier R-matrix theoretical calculations of $1s \rightarrow 2p$ and $3p$ absorption resonances of $C^{2+}$ ions.....	77
3.11	Present R-matrix results with and without Auger broadening effects for the ground state photoabsorption of $C^{2+}$ at the K-edge. ....	78

# CHAPTER I

## INTRODUCTION

This dissertation describes the theoretical atomic physics research performed over the past five years devoted to improving the atomic data needed by astrophysical plasma modelers in their studies of the chemical composition and the evolution of the universe. In fact, a majority of funding for this work was received from NASA's Astronomy Physics Research and Analysis (APRA) and Solar and Heliospheric Physics (SHP) Supporting Research and Technology (SR&T) programs. As such, the relevance to astrophysical studies and the role of theoretical atomic physics are discussed before outlining the two main areas of research for this dissertation: the fluorescence yields of K-shell vacancy states and the K-shell photoabsorption spectra.

### 1.1 Overview

Since we are primarily concerned with the studies of photoionized plasmas - those in which low-temperature (energy) electrons and ions are subject to X-ray absorption and emission - there are two fundamental processes of interest for determining the physical environments of any photoionized astrophysical plasma. These are 1) the X-ray absorption itself, which is predominantly a K-shell process, and 2) the X-ray emission probabilities (fluorescence and Auger yields) from K-shell-vacancy states. All relevant K-shell processes are depicted in Fig. 1.1.

# X-Ray - K-Shell Atomic Processes

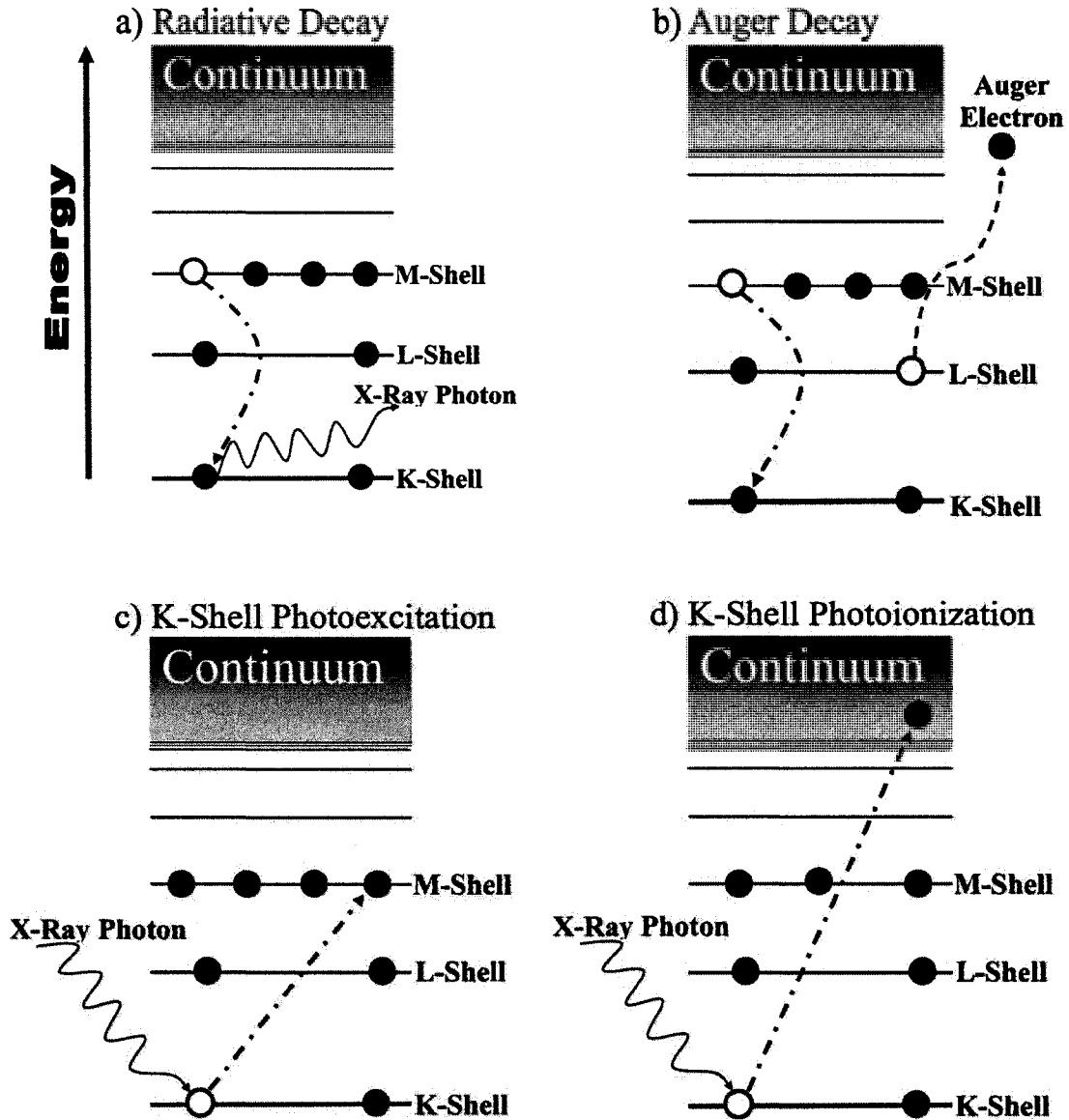


**Figure 1.1** Relevant K-shell X-ray processes: **a)** Emission of an X-ray photon via radiative decay to a K-shell vacancy state, **b)** Emission of an Auger electron via Auger decay to a K-shell vacancy state, **c)** Photoexcitation of a K-shell electron via X-ray photoabsorption, **d)** Photoionization of a K-shell electron via X-ray photoabsorption.

The primary focus of this dissertation work is on the second process, specifically the calculation of the various probabilities for radiative (see Fig. 1.1a) vs. Auger (see Fig. 1.1b) decay of the K-shell vacancy ions; these are predominantly produced in X-ray photoionized plasmas. The probabilities of these competing processes are crucial for determination of the fundamental characteristics of an astrophysical plasma, notably the ionization balance and the photoemission spectra. These data are of particular importance for the interpretation of the spectra of photoionized plasmas such as those produced in active galactic nuclei (AGN) and X-ray binaries, as well as for supernova remnants (SNR) under non-equilibrium ionization conditions.

The secondary part of this dissertation, initiated less than two years ago, involves the computation of the photoabsorption cross sections. These absorption features are ubiquitous in K-shell (or X-ray) astrophysical spectra [1] and aid in interpreting the elemental abundances in the Interstellar Medium (ISM).

## 1.2 K-Shell Fluorescence Yields

The K-shell fluorescence yield, from a given inner-shell-vacancy state, is a measure of the relative probability of spontaneous radiative (photon emission) decay vs. autoionization (electron emission):

$$\omega_{\text{K}} = \frac{A_r}{A_r + A_a} . \quad (1.1)$$

Here  $A_r$  is the total radiative rate and  $A_a$  is the total radiationless Auger decay rate of the K-shell vacancy state. Thus, the value of  $\omega_{\text{K}}$  is obviously bounded between 0 and 1:  $0 \leq \omega_{\text{K}} \leq 1$ .

Since the hydrogenic  $Z$ -scaling [2] (see also Appendix B) of the decay rates  $A_r = A_{r1}Z^4$  and  $A_a = A_{a1}Z^0$  is smooth, the resulting fluorescence yield can be written as

$$\omega_K = \left(1 + \frac{1}{aZ^4}\right)^{-1}, \quad (1.2)$$

where we have defined  $a \equiv A_{r1}/A_{a1}$ . In general, this hydrogenic model exhibits monotonically increasing behavior  $0 \leq \omega_K \xrightarrow{Z \rightarrow \infty} 1$  (see Fig. 1.2 for behavior using typical ratios  $10^{-7} \leq a \leq 10^{-5}$ ). Of course, the non-hydrogenic screening leads to additional

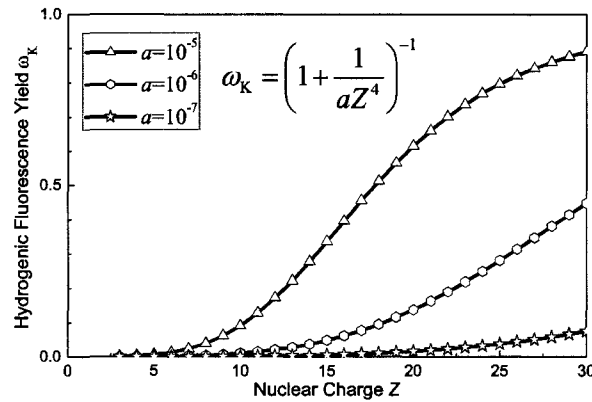


**Figure 1.2** Hydrogenic behavior of the K-shell fluorescence yield as a function of nuclear charge  $Z$  for three typical values of the ratio  $a$ .

$Z$ -dependent effects, but the smooth behavior depicted in Fig. 1.2 and Eq. 1.2 is generally found in most of our results (see Sec. 3.1).

The primary presently-recommended source of these data is the compilation of Kaastra and Mewe published in 1993 [3]\*. This comprehensive database considers the sequential multiple electron and/or photon ejections for all stages of all  $1s$ -vacancy ions in the periodic table up through Zn -the heaviest cosmically-abundant element. Those data are based upon single-particle central-field atomic calculations for singly-ionized atoms [4, 5, 6, 7, 8], and

\*Our main aim is to update this database [3] with more reliable results.

extrapolated for the remainder of each isoelectronic sequence. In that database, the electron and photon emission yields were computed using radiative and autoionization rates that were then configuration-averaged (see Sec. 3.1.2) over possible terms, and the fluorescence yield was then reported as a ratio of the averaged radiative rate to the sum of the averaged radiative and Auger rates. Those data are still used in various astrophysical modeling codes, e.g., CLOUDY [9], XSTAR [10] and the SNR code of Borkowski [11].

In an earlier work initiated at Western Michigan University, that in fact precipitated the entire present line of study, the accuracy of that widely-used fluorescence and Auger database [3] was investigated for Be- and F-like  $1s$ -vacancy sequences [12], and it was shown that the configuration-averaged method is incorrect for astrophysical and fusion-research-related plasma modeling purposes. In subsequent studies, that database [3] is shown to be inaccurate due to several deficiencies, as explained in Sec. 3.1.

We compute K-shell fluorescence yields for Li-, Be-, B-, C-, N-, O-like, and F-like  $1s$ -vacancy isoelectronic sequences up through Zn with nuclear charge  $Z = 30$  (see Sec. 3.1). For these cases, only single electron or photon emission processes need to be considered due to the L-shell simplification that there are no other inner-shells that can also make a transition to the K-shell. We first perform multi-configuration Breit-Pauli (MCBP) calculations using the atomic structure and collision package AUTOSTRUCTURE [13] and demonstrate the significance of properly including such physical effects as correct configuration averaging and semi-relativistic (i.e., spin-orbit (S.O.)) effects. Thus, we demonstrate that the extant database [3] in current use by CLOUDY [9] and XSTAR [10] is largely inaccurate and/or inapplicable for astrophysical modeling purposes.

### 1.3 K-Shell Photoabsorption Cross Sections

The ISM - that which fills the space between stars and other cosmic objects - is composed of mainly gas (99%) and also dust particles, and has a very low density, typically about  $10^{-17} - 10^{-19}$  times that of the air we breathe. Astronomers use bright background X-ray sources to probe the physical conditions and elemental abundances of gas clouds within the ISM of our galaxy. The inner-shell excitation and ionization features of the elements in the ISM can be easily detected in the X-ray spectra. The advent of new orbiting X-ray telescopes with high-spectral resolution has opened a new window to study the ISM. For instance, photoabsorption features found in the cosmologically abundant carbon through iron ions fall into the spectral range of data obtained from the Chandra (<http://chandra.harvard.edu/>) and XMM-Newton (<http://xmm.vilspa.esa.es/>) X-ray telescopes. Therefore, astrophysicists need reliable photoabsorption predictions to study the high-resolution X-ray spectra transmitted through the ISM. Also, it is suspected that neutral carbon within the detectors exhibits spectral features [1]. Therefore, the neutral carbon photoabsorption spectrum is needed for the calibration of X-ray spectra from the Chandra and XMM-Newton space telescopes (see, for example, the recently-observed Chandra X-ray spectra in the energy region below the carbon K-edge in Fig. 1.3).

The observed flux density,  $I$ , which is related to the emission flux density  $I_o$  as

$$I(\lambda) = I_o(\lambda) \exp [-\sigma^{\text{PA}}(E)N] , \quad (1.3)$$

is shown in Fig. 1.3. Here  $\lambda$  is the wavelength that is related to photon energy as  $E = hc/\lambda$  ( $h$  is Planck's constant and  $c$  is the speed of light),  $\sigma^{\text{PA}}$  is the photoabsorption cross section,

and  $N$  is the number of absorbers per unit area, known as the column density. In this figure, each dip in the observed flux,  $I$ , corresponds to a resonance peak in the photoabsorption cross,  $\sigma^{\text{PA}}$  (see, for example, Fig. 3.7).

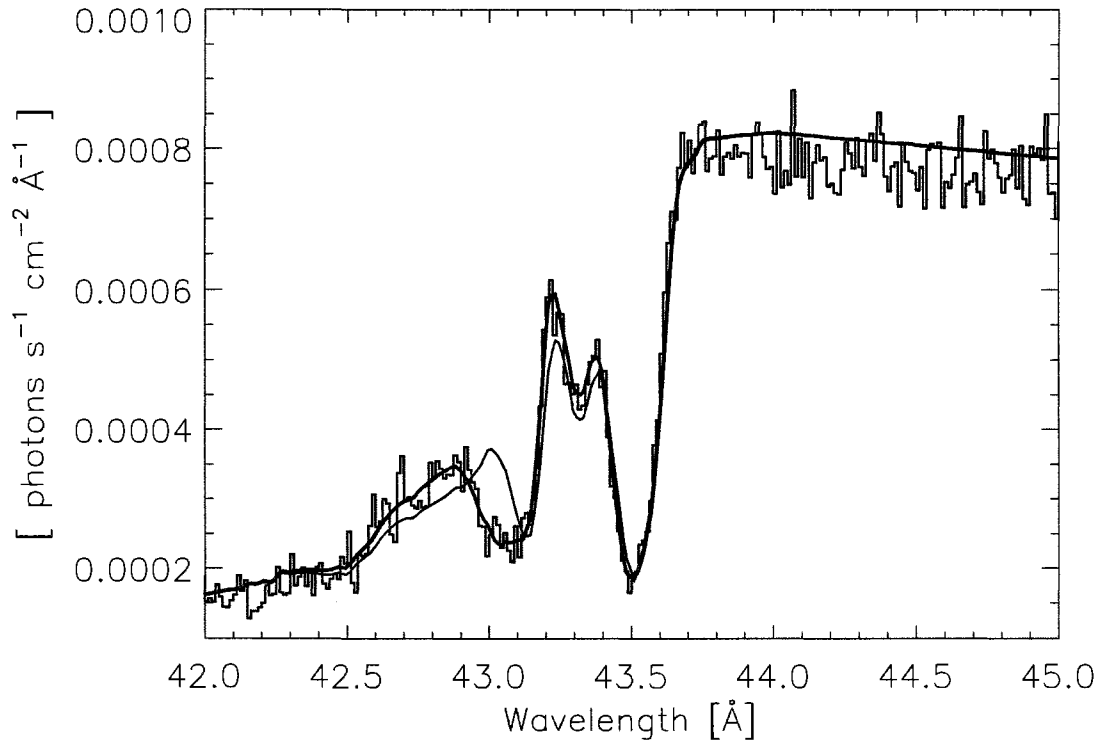


**Figure 1.3** Observed X-ray spectrum of the bright extra-galactic X-ray source Blazar Mkn 421 near the carbon K-edge obtained from the Chandra X-ray Observatory [1]. For these sources with a hydrogen ISM column density of about  $N_{\text{H}} = 1.5 \times 10^{20} \text{ cm}^{-2}$ , the edge absorption features are predominantly due to the instrument (in particular, a polyimide filter), but there is an expected  $\sim 10\%$  contribution from the ISM. The observational data are shown as the black line, the blue curve is a smoothed representation of the data, and the red curve is the latest model [1] using various sources of data including semi-empirical approximations (<http://chandra.harvard.edu/>).

In an earlier work at WMU, K-shell photoabsorption cross sections of neon [14, 15] and oxygen [16, 17] ions were computed. Those results were compared to high-resolution X-ray spectroscopy of ISM gas clouds [14, 18] to determine their abundances of oxygen and neon ions. We have calculated photoabsorption cross sections using an optical potential R-

matrix method (see Sec. 2.4). This method was shown to be successful in describing both experimental synchrotron measurements [15, 19, 20] and Chandra high-resolution spectroscopic observations [14, 16, 18]. The photoabsorption cross section of carbon, specifically the  $1s \rightarrow np$  (see Fig. 1.1c) absorption features and  $np \rightarrow \epsilon p$  (see Fig. 1.1d) above-threshold photoionization edge, has not, to our knowledge, been previously studied either theoretically or experimentally.

## CHAPTER II

### THEORETICAL METHODOLOGY

This part of the dissertation is devoted to explaining the theory behind the computational atomic physics codes that we have used in our calculations. First, as a background, the description of many electron systems is discussed briefly.

For computation of K-shell fluorescence yields, we use the multi-configuration Breit-Pauli (MCBP) perturbative method. Specifically, the atomic structure and collision code AUTOSTRUCTURE [13], an extension of SUPERSTRUCTURE [21], is utilized. This program calculates energy levels, autoionization rates, and radiative rates within a multi-configuration Breit-Pauli (MCBP) framework. The bound, resonance, and continuum atomic orbitals are generated internally within the AUTOSTRUCTURE code from a Slater-type of Hartree model potential (see Sec. 2.2.3). This approach has been further generalized to the use of non-orthogonal orbital bases, therefore including important  $1s$  relaxation effects that occur due to K-shell photoexcitation and/or ionization. The MCBP perturbative method is presented in Sec. 2.3.

For our computation of K-shell photoabsorption cross sections, on the other hand, we have found it more efficient and accurate to rely on the close-coupling R-matrix method [22, 23, 24] as implemented for many-channel atomic physics [25, 26]. Specifically, we use the R-MAX suit of codes [27] that has been further developed to eliminate unphysical pseudo-resonances, which otherwise would appear when including important orbital relaxation effects via addition of pseudo-orbitals [28], and spectator Auger decay broadening,

via an optical potential, which otherwise would not account for near-K-edge features correctly [19]. The application of standard R-matrix theory to many-electron systems in a non-relativistic LS-coupling scheme is presented in Sec. 2.4.

In the photoabsorption cross section calculations, the radial orbitals are generated by using Hartree-Fock (HF) and multi-configuration Hartree-Fock (MCHF) variational methods [29, 30, 31, 32], as discussed in Secs. 2.2.2 and 2.2.3.

We use atomic units ( $\hbar = m = e = k_e = 1$ , see Appendix A) except where specified in our mathematical derivations and equations.

## 2.1 Many-Body Atomic Description

### 2.1.1 Non-Relativistic Hamiltonian, Wave Function, and Schrödinger Equation

In the absence of external fields and relativistic effects, the Hamiltonian of an  $N$ -electron atomic system in SI units is given by

$$\mathcal{H} = \sum_{i=1}^N \left( -\frac{\hbar^2}{2m} \nabla_i^2 - k_e \frac{Ze^2}{r_i} \right) + \sum_{i<j}^N k_e \frac{e^2}{r_{ij}}.$$

Here the first term is the sum of kinetic energies of each electron, the second term is the Coulomb electron-nucleus interaction, and the third term is the electrostatic interaction between all two-electron pairs, where the restriction  $i < j$  on the summation is imposed to avoid double counting of electron pairs.

In atomic units, these terms becomes less clear, but mathematically free of physical constants, and reads as

$$\mathcal{H} = \sum_{i=1}^N \left( -\frac{1}{2} \nabla_i^2 - \frac{Z}{r_i} \right) + \sum_{i<j}^N \frac{1}{r_{ij}}. \quad (2.1)$$

The time-independent Schrödinger equation for an  $N$ -particle system, subject to this Hamiltonian, is

$$\mathcal{H}\psi(q_1, q_2, \dots, q_N) = E\psi(q_1, q_2, \dots, q_N), \quad (2.2)$$

where  $q_i = \{\vec{r}_i, \chi_i\}$  denotes the spatial and spin degrees of freedom of each of the  $N$  electrons. From a quantum mechanical point of view, because our Hamiltonian is symmetric upon interchange of any two electrons, mathematical solutions with certain even or odd parity are expected [33]. Furthermore, considering the Pauli exclusion principle, we desire solutions that are antisymmetric with respect to interchange of any two electrons: a corollary is that no two electrons can occupy the same quantum state.

As is known from one-electron hydrogenic systems, a one-electron wave function can be described by quantum numbers  $n, l, m_l$ , and  $m_s$  ( $s = 1/2$ ) as

$$\phi_{nlsm_l m_s}(\vec{r}, \chi) = \varphi_{nlm_l}(\vec{r})\chi_{m_s} = \frac{P_{nl}(r)}{r} Y_l^{m_l}(\Omega)\chi_{m_s}. \quad (2.3)$$

Here  $P_{nl}(r)$  are the radial orbitals,  $Y_l^{m_l}(\Omega)$  are normalized spherical harmonics, and  $\chi_{m_s}$  are the spin states ( $\chi_{\pm} = \chi_{\pm 1/2}$ , where the  $+$  stands for spin-up states and the  $-$  stands for spin-down states). These quantum numbers are related to physical operators that commute with the one-electron Hamiltonian. Here  $n$  is the principal quantum number that quantizes the energy,  $l$  and  $m_l$  are the total and  $z$ -component orbital angular momenta, and  $s$  and  $m_s$  correspond to the total and  $z$ -components of the spin. For the more complicated multi-electron case, due to the electron-electron interaction term, analytic solutions do not exist even for the simplest two-electron He case, and approximations must be made in order to

find approximate physical solutions of the system. The approximation methods used in our calculations are presented in Sec. 2.2.

We need to know the “good” quantum numbers describing our system from which we will build our wave functions. It is well known that, neglecting relativistic (spin-orbit, etc.) interactions, the total orbital angular momentum  $\vec{L} = \sum_{i=1}^N \vec{l}_i$  and total spin  $\vec{S} = \sum_{i=1}^N \vec{s}_i$  of the system both commute with our Hamiltonian:

$$[\vec{L}, \mathcal{H}] = [\vec{S}, \mathcal{H}] = [\vec{L}, \vec{S}] = 0. \quad (2.4)$$

The commutation relations between the components of orbital angular and spin momenta are given as

$$[L_i, L_j] = i\varepsilon_{ijk}L_k \quad \text{and} \quad [S_i, S_j] = i\varepsilon_{ijk}S_k, \quad (2.5)$$

where  $\varepsilon_{ijk}$  is the Levi-Civita symbol [34]. Thus our wave function can be expanded in terms of eigenstates of  $\mathcal{H}$ ,  $L^2$ ,  $L_z$ ,  $S^2$ , and  $S_z$  simultaneously. At this point, even though the non-relativistic Hamiltonian is independent of spin, we still need to consider the spin of each electron in order to fulfill the requirements for identical fermion systems (for  $s_i = 1/2$ , or half-integer, the Pauli Exclusion Principle). Such quantum states can be written in Dirac bra-ket notation as  $|\alpha LSM_L M_S\rangle$  with eigenvalues of  $L^2$ ,  $S^2$ ,  $L_z$ , and  $S_z$  that are  $L(L+1)$ ,  $S(S+1)$ ,  $M_L$ , and  $M_S$ , respectively. Here  $\alpha$  is an index representing additional information required to specify the state unambiguously, such as the radial part of the wave function, the parity, the (dominant) electronic configuration, etc.

The total wave function  $|\alpha LSM_L M_S\rangle$  can be obtained by coupling the orbital and spin angular momenta of each electron. This gives a linear combination of products of un-

coupled states with coupling coefficients that are obtained from angular momentum algebra [2, 35, 36, 37]. This coupling method is known as LS, or Russell-Saunders, coupling, and is *usually* sufficient for describing most properties of lighter atoms, where the Coulombic interaction is far greater than any relativistic effect, predominantly the spin-orbit interaction. However, as we will see, spin-orbit effects can nevertheless be prominent in many cases. The spectroscopic notation for this LS-quantum state is  $^{2S+1}L$ , where  $2S + 1$  is the spin multiplicity and  $L$  is the total orbital angular momentum of the system. A Slater determinant form can now be used to construct an antisymmetric wave function for the state  $|\alpha LM_L SM_S\rangle$  with appropriate coupling coefficients that ensure orthogonality.

Electron states with quantum numbers  $n_i$  and  $l_i$  are referred to as sub-shells. The number of possible states for a particular  $nl$  shell is  $2(2l + 1)$ ; note that  $m_s = \pm 1/2$  and  $-l \leq m_l \leq l$ . A set of  $n_i l_i$  is known as an electron configuration of an  $N$ -electron system and is written as an expansion

$$(n_1 l_1)^{w_1} (n_2 l_2)^{w_2} \dots (n_m l_m)^{w_m} , \quad (2.6)$$

where  $w_i$  denotes the total number of electrons occupying the sub-shell  $n_i l_i$ , giving a total number of electrons

$$N = \sum_{a=1}^m w_a .$$

Electrons occupying the same shell are said to be equivalent electrons. The orbital angular momentum quantum number of a shell usually uses the following letter code:

Value of  $l$ : 0 1 2 3 4 5 6 7 8 9 ...

Designation:  $s$   $p$   $d$   $f$   $g$   $h$   $i$   $j$   $l$   $m$  ...

Another important quantum number for an electron configuration is the parity  $\pi$ , which is defined as  $\pi = (-1)^{w_1 \times l_1} (-1)^{w_2 \times l_2} \dots (-1)^{w_m \times l_m}$ . States with parity of  $\pi = +1$  are said to be even and those with  $\pi = -1$  are said to be odd.

Up to now, the determination of the total wave function for an  $N$ -electron system is described within a non-relativistic approximation. At this point, let us look at the expectation value of the energy for the system. Our atomic Hamiltonian can be partitioned into one- and two-body operators via

$$\mathcal{H} = \sum_{i=1}^N f(i) + \sum_{i < j=1}^N g(i, j),$$

where the one-body and two-body operators are given by

$$f(i) = \frac{-\nabla_i^2}{2} - \frac{Z}{r_i} \quad \text{and} \quad g(i, j) = \frac{1}{|\vec{r}_i - \vec{r}_j|},$$

respectively.

By invoking Slater determinant properties [2, 37, 38], we obtain the expectation value of the Hamiltonian in terms of one- and two-body operator matrix elements:

$$\begin{aligned} \langle \mathcal{H} \rangle = & \sum_{i=1}^N \langle \varphi_{q_i}(1) | f(1) | \varphi_{q_i}(1) \rangle + \sum_{i < j=1}^N [\langle \varphi_{q_i}(1) \varphi_{q_j}(2) | g(1, 2) | \varphi_{q_i}(1) \varphi_{q_j}(2) \rangle \\ & - \delta_{m_{s_i} m_{s_j}} \langle \varphi_{q_i}(1) \varphi_{q_j}(2) | g(1, 2) | \varphi_{q_j}(1) \varphi_{q_i}(2) \rangle]. \end{aligned} \quad (2.7)$$

Here the first term represents the kinetic energy of the electrons and the electrostatic interaction of the electrons with the nucleus. The second term is called the Coulomb interaction

between all pairs of electrons. The third term is known as the exchange interaction originating from the indistinguishability of any two electrons, and exists only between electrons with the same spin,  $m_{s_i} = m_{s_j}$ .

The operators  $f(i)$  and  $g(i, j)$  carry both radial and angular dependence. The operator  $g(i, j)$  can be expanded using the addition theorem of spherical harmonics [34],

$$\frac{1}{|\vec{r}_1 - \vec{r}_2|} = \sum_{k=0}^{\infty} \frac{4\pi}{2k+1} \sum_{m=-k}^k \frac{r_{<}^k}{r_{>}^{k+1}} Y_{km}^*(\Omega_1) Y_{km}(\Omega_2), \quad (2.8)$$

where the smaller of  $r_1$  and  $r_2$  is  $r_{<}$  and the larger one is  $r_{>}$ . By using this expansion in Eq. 2.7, and considering the angular and spin algebra, the energy of the system can be shown to be composed of one- and two-electron radial integrals along with the appropriate angular coefficients. But the radial orbitals are yet to be determined. Approximation methods for determining the bound radial orbitals are described in Sec. 2.2.3.

### 2.1.2 Relativistic Corrections

In the previous section, the treatment of atomic systems in a non-relativistic framework was discussed. Although a non-relativistic approximation is good for light atoms, relativistic effects should be considered for heavier atomic systems to get a fuller description of the system. The importance of relativistic effects increases quickly for heavy atoms as  $Z^4$  for the predominant spin-orbit effects (see Appendix B). To treat relativistic effects properly, a fully-relativistic Dirac equation should be solved. This is a very time consuming and difficult task due to the increased dimensionality caused by the presence of four components [39]. For our calculations of astrophysical interest, it is sufficient to consider the first-order corrections via perturbing the non-relativistic Hamiltonian [21]. We have com-

pared our MCBP perturbative method results and other available fully relativistic MCDF results for fluorescence yield calculations [40, 41, 42] (see also Sec. 3.1). We have found good agreement between the two calculations, showing that inclusion of relativistic corrections perturbatively is sufficient for light atomic systems,  $Z \leq 30$ .

These additional relativistic effects can be derived by expanding the relativistic many-electron equation in powers of  $\alpha v$  to order of  $\alpha^2$ , where  $\alpha = 1/c \approx 1/137.036$  is known as the fine-structure constant and  $v$  is the speed of the electron. The resulting Hamiltonian, including corrections to order of  $\alpha^2$ , is known as the Breit-Pauli Hamiltonian [21, 30, 38]

$$\mathcal{H}_{BP} = \mathcal{H}_{NR} + \mathcal{H}_{Rel} . \quad (2.9)$$

The relativistic correction operator can be divided into two parts: a relativistic shift operator and a fine-structure operator,  $\mathcal{H}_{Rel} = \mathcal{H}_{RS} + \mathcal{H}_{FS}$ .

The relativistic shift operator includes five terms as follows:

$$\mathcal{H}_{RS} = H_{MC} + \mathcal{H}_{D1} + \mathcal{H}_{D2} + \mathcal{H}_{OO} + \mathcal{H}_{SSC}.$$

Here  $\mathcal{H}_{MC}$  is the mass correction term

$$\mathcal{H}_{MC} = -\frac{\alpha^2}{8} \sum_{i=1}^N (\vec{\nabla}_i^2)^\dagger \vec{\nabla}_i^2 ,$$

$\mathcal{H}_{D1}$  and  $\mathcal{H}_{D2}$  are the one- and two-body Darwin terms

$$\mathcal{H}_{D1} = -\frac{\alpha^2 Z}{8} \sum_{i=1}^N \vec{\nabla}_i^2 \left( \frac{1}{r_i} \right) , \text{ and}$$

$$\mathcal{H}_{D2} = \frac{\alpha^2}{4} \sum_{i < j=1}^N \vec{\nabla}_i^2 \left( \frac{1}{r_{ij}} \right) ,$$

$\mathcal{H}_{SSC}$  is the spin-spin contact term

$$\mathcal{H}_{SSC} = -\frac{8\pi\alpha^2}{3} \sum_{i<j=1}^N (\vec{s}_i \cdot \vec{s}_j) \delta(\vec{r}_i, \vec{r}_j),$$

and  $\mathcal{H}_{OO}$  is the orbit-orbit term

$$\mathcal{H}_{OO} = -\frac{\alpha^2}{2} \sum_{i<j=1}^N \left[ \frac{\vec{p}_i \cdot \vec{p}_j}{r_{ij}} + \frac{r_{ij} (\vec{r}_{ij} \cdot \vec{p}_i) \vec{p}_j}{r_{ij}^3} \right].$$

The fine-structure operator consists of three terms

$$\mathcal{H}_{FS} = \mathcal{H}_{SO} + \mathcal{H}_{SOO} + \mathcal{H}_{SS}.$$

The first term is the spin-orbit interaction

$$\mathcal{H}_{SO} = \frac{\alpha^2 Z}{2} \sum_{i=1}^N \frac{1}{r_i^3} \vec{l}_i \cdot \vec{s}_i,$$

the second term is known as the spin-other-orbit interaction

$$\mathcal{H}_{SOO} = -\frac{\alpha^2}{2} \sum_{i<j=1}^N \frac{\vec{r}_{ij} \times \vec{p}_i}{r_{ij}^3} (\vec{s}_i + 2\vec{s}_j),$$

the third terms is known as the spin-spin interaction

$$\mathcal{H}_{SS} = \alpha^2 \sum_{i<j=1}^N \frac{1}{r_{ij}^3} \left[ \vec{s}_i \cdot \vec{s}_j - 3 \frac{(\vec{s}_i \cdot \vec{r}_{ij})(\vec{s}_j \cdot \vec{r}_{ij})}{r_{ij}^2} \right].$$

In the relativistic Hamiltonian  $\mathcal{H}_{Rel}$ , the one-body operators scale as  $Z^4\alpha^2$  while the two-body operators scale as  $Z^3\alpha^2$ .

The relativistic shift Hamiltonian commutes with total orbital angular momentum  $\vec{L}$  and spin angular momentum  $\vec{S}$ , just like the non-relativistic Hamiltonian, whereas the fine-structure operator  $\mathcal{H}_{FS}$  does not. However, it does commute with the total angular momentum of the system,  $\vec{J} = \vec{L} + \vec{S}$  ( $[\mathcal{H}_{FS}, \vec{J}] = 0$ ). Consequently, considering fine-structure

effects in the Hamiltonian  $L, S, M_L$ , and  $M_S$  are no longer good quantum numbers. To include  $\mathcal{H}_{FS}$  in our Hamiltonian, we need to recouple from  $|LSM_LM_S\rangle$  states to  $|JM_J\rangle$  states. This can be achieved by addition of total angular  $\vec{L}$  and spin  $\vec{S}$  momenta as follows:

$$|JM_J\rangle = \sum_{M_L=M_L+M_S} \langle LSM_LM_S|JM_J\rangle |LSM_LM_S\rangle, \quad (2.10)$$

where  $\langle LSM_LM_S|JM_J\rangle$  are known as Clebsch-Gordan coefficients. This coupling method is called intermediate coupling (IC) [2, 37].

### 2.1.3 Relevant Atomic Transitions: Auger and Radiative Rates

Transitions between quantum states may take place due to a perturbing potential  $\mathcal{H}'$ . In quantum mechanics, the transition rate,  $\Gamma_{i \rightarrow f}$ , for a particular transition from an initial state  $|i\rangle$  to a final state  $|f\rangle$  can be determined using Fermi's golden rule [33, 37, 43] that can be derived from first-order time-dependent perturbation theory as

$$\Gamma_{i \rightarrow f} = 2\pi |\langle f|\mathcal{H}'|i\rangle|^2 \rho(f). \quad (2.11)$$

Here  $\rho(f)$  is the density of final states (the number of states per unit energy, which is usually taken to be one by normalizing the continuum wave functions appropriately\*) and  $\langle f|\mathcal{H}'|i\rangle$  is the transition matrix element.

### Radiative Rates

We are interested in the radiative transitions that occur between two atomic states, leading to the emission of a photon accompanied by an atomic transition from a higher-energy state to a lower-energy state, or conversely, absorption of a photon accompanied by an

---

\*Note that it can be shown [44] that  $\rho(f) = 1 \Leftrightarrow \int P_{\epsilon l}(r) P_{\epsilon' l'}(r) dr = \delta_{ll'} \delta(\epsilon - \epsilon')$ .

atomic transition from a lower state to a higher state. This follows from the well-known principle of detailed balance. In the electric dipole approximation, the radiative rate,  $A_r^{i \rightarrow f}$ , from an initial state  $|i\rangle$  to a final state  $|f\rangle$ , due to a weak field (assuming that the square of the vector potential is negligible,  $\vec{A}^2 \approx 0$ ), is given by Fermi's golden rule with quantization of electromagnetic field considerations [33, 43, 44]:

$$A_r^{i \rightarrow f} = \frac{4\alpha^3}{3} w^3 |\langle f | \mathcal{D} | i \rangle|^2. \quad (2.12)$$

Here  $w$  is energy of the photon, defined as the difference between the initial and the final state energies,  $w = w_f - w_i$ , and  $\mathcal{D} = \sum_{i=1}^N \vec{r}_i$  is the electric dipole operator. (Note that, in SI units,  $\sum_{i=1}^N e\vec{r}_i$  is readily identified as the electric dipole moment). In this transition, since  $\vec{r}$  is a tensor of rank one, the initial and final  $L$  must satisfy the triangular inequality  $|L_i - L_f| \leq 1$  (neglecting S.O. interactions), and since the electron-photon operator is independent of spin and has odd parity, we have the following *dipole selection rules* [2]:

$$\text{LS-coupling: } \left\{ \begin{array}{ll} \Delta\pi = \pm 1 & \\ \Delta S = 0 & \Delta M_S = 0 \\ \Delta L = 0, \pm 1 & \Delta M_L = 0, \pm 1 \\ \Delta L = 1 \text{ if } L_i = 0 & , \end{array} \right.$$

Similarly, for IC-coupling,

$$\text{IC-coupling: } \left\{ \begin{array}{ll} \Delta\pi = \pm 1 & \\ \Delta J = 0, \pm 1 & \Delta M_J = 0, \pm 1 \\ \Delta J = 1 \text{ if } J_i = 0 & . \end{array} \right.$$

In a non-relativistic (LS) approximation, and by using appropriate commutation relations, the dipole matrix element,  $\mathcal{D}_{if} = \langle f | \vec{r} | i \rangle$ , can be expressed in various forms as

$$\mathcal{D}_{if} = \begin{cases} \langle f | \sum_{i=1}^N \vec{r}_i | i \rangle & \text{Length Form} \\ -\frac{1}{w} \langle f | \sum_{i=1}^N \vec{\nabla}_i | i \rangle & \text{Velocity Form} \\ \frac{1}{w^2} \langle f | \sum_{i=1}^N \vec{\nabla}_i V | i \rangle & \text{Acceleration Form} . \end{cases}$$

The dipole matrix element can be calculated by using any of these forms. We typically compute only length and velocity forms of the dipole operator, allowing for comparison in output radiative data, and usually report results determined from the length form of the dipole operator. Comparison between different forms is an important consistency check for the quality and completeness of the wave function. The closer they are, in general, the better the wave functions are (it is a necessary, but not sufficient, condition) [2, 43]. Here we have only presented the different forms of the dipole operator in an LS-coupling scheme. In an IC-coupling scheme, the dipole operator can also be expressed in length, velocity, and acceleration forms.

### Auger Rates

An alternative process involving the transition between atomic states from an inner-shell-vacancy state is the so-called Auger decay. In this process, an outer electron may fill the inner-shell vacancy, instead of emitting a photon, and the additional energy can be transferred to another electron that departs the atom. The Auger rate from an initial atomic state  $|i\rangle$  to a final  $|f\rangle$  is also given by Fermi's golden rule [2, 33, 38] as

$$A_a^{i \rightarrow f} = 2\pi \left| \left\langle f \left| \sum_{m \neq n} \frac{1}{|\vec{r}_m - \vec{r}_n|} \right| i \right\rangle \right|^2 . \quad (2.13)$$

Note that, since  $|\vec{r}_m - \vec{r}_n|^{-1}$  is a scalar, then, in either LS- or IC-coupling schemes, both  $|i\rangle$  and  $|j\rangle$  atomic states must have the same symmetry. If  $E_o$  is the energy of the outer electron,  $E_v$  is the inner-shell vacancy energy, and  $E_b$  is the energy of the initial, then the vacated Auger electron is ejected with kinetic energy  $k^2/2 = E_o - E_v - E_b$ .

We treat the computation of radiative rates (in both length and velocity forms) and Auger rates, in both LS- and IC-coupling schemes, as follows. Following the determination of orbitals given in Sec 2.2.3, we then perform a configuration-interaction (CI) expansion for the wave functions (see Sec. 2.2.4). Since our relevant observables, for LS-terms and IC-levels, are unaligned states, we average over initial  $M_L$  and  $M_S$ , or  $M_J$ , magnetic levels, and sum over final  $M_L$  and  $M_S$ , or  $M_J$ , magnetic levels to get our term/level dependent, statistically-averaged rates.

## 2.2 Approximate Many-Body Wave Functions

### 2.2.1 Exchange, Antisymmetry, and Slater Determinants

Complications due to the non-local electron-electron interaction term in the Schrödinger equation for an  $N$ -electron Hamiltonian in Eq. 2.1 can be overcome by using a model central potential. In this *Central Field Approximation*, it is assumed that the electron moves in an averaged, spherically-symmetric potential due to the nucleus and all other  $(N - 1)$  electrons, simplifying the eigenvalue problem into  $N$  separable equations [2, 37, 38]. We then seek one-electron wave function solutions as given in Eq.2.3, yielding a radial equation for each orbital as

$$\left( \frac{d^2}{dr^2} - \frac{l_i(l_i + 1)}{r^2} - 2V_i(r) + 2E_i \right) P_{n_i l_i}(r) = 0. \quad (2.14)$$

A multi-electron wave function is then constructed as a product of single-electron wave functions with individual quantum numbers  $\lambda_i = \{n_i, l_i, m_{l_i}, m_{s_i}\}$ . However, antisymmetry is not, in general, satisfied by a single product wave function. Instead, Slater determinants [2, 37, 38] are used to construct antisymmetric multi-electron wave functions that satisfy the Pauli Exclusion principle,

$$\psi(q_1, q_2, \dots, q_N) = \frac{1}{\sqrt{N!}} \begin{vmatrix} \phi_{\lambda_1}(q_1) & \phi_{\lambda_1}(q_2) & \cdots & \phi_{\lambda_1}(q_N) \\ \phi_{\lambda_2}(q_1) & \phi_{\lambda_2}(q_2) & \cdots & \phi_{\lambda_2}(q_N) \\ \vdots & \vdots & \ddots & \vdots \\ \phi_{\lambda_N}(q_1) & \phi_{\lambda_N}(q_2) & \cdots & \phi_{\lambda_N}(q_N) \end{vmatrix} \quad (2.15)$$

where  $\phi_{\lambda_i}(q_j)$  is the one-electron wave function of the electron occupying quantum state  $\lambda_i = \{n_i, l_i, m_{l_i}, m_{s_i}\}$  (see Eq. 2.3) with  $j^{\text{th}}$  space and spin coordinates  $\vec{r}_j$  and  $\chi_j$ , respectively. Since determinants are antisymmetric with respect to interchange of any two columns or rows, we are guaranteed a completely antisymmetric wave function. This determinant also can be written in a shorthand notation with permutation operator,  $P$ , as

$$\psi(q_1, q_2, \dots, q_N) = \frac{1}{\sqrt{N!}} \sum_P (-1)^P P \phi_{\lambda_1}(q_1) \phi_{\lambda_2}(q_2) \cdots \phi_{\lambda_N}(q_N), \quad (2.16)$$

where the summation is over all permutations.

### 2.2.2 Variational Method

Given a trial wave function  $\psi$  which, in general, must be a linear combination of Slater determinants to ensure that it is also an eigenfunction of our  $N$ -electron Hamiltonian, we now proceed to seek solutions to our wave function. The optimization of our individual

orbitals  $\phi_{\lambda_i}(q_j)$  are obtained by using the variational principle for the "best" orbitals, as follows. Consider the energy of the system to be

$$E(\psi) = \frac{\langle \psi | \mathcal{H} | \psi \rangle}{\langle \psi | \psi \rangle}. \quad (2.17)$$

We seek solutions  $\psi$  such that the energy is stable under any infinitesimal variations  $\delta\psi$ , that is

$$\lim_{\delta\psi \rightarrow 0} \frac{\delta E}{\delta\psi} = 0. \quad (2.18)$$

Given that

$$\begin{aligned} \delta E = E(\psi + \delta\psi) - E(\psi) &= \frac{\langle \psi + \delta\psi | \mathcal{H} | \delta\psi + \psi \rangle}{\langle \psi + \delta\psi | \delta\psi + \psi \rangle} - \frac{\langle \psi | \mathcal{H} | \psi \rangle}{\langle \psi | \psi \rangle} \\ &= \frac{\langle \psi | \mathcal{H} | \delta\psi \rangle}{\langle \psi | \psi \rangle} - \frac{\langle \delta\psi | \mathcal{H} | \psi \rangle}{\langle \psi | \psi \rangle} + \mathcal{O}(\delta\psi^2), \end{aligned} \quad (2.19)$$

where we have imposed the variational condition  $\langle \delta\psi | \psi \rangle = 0$ , we must have that

$$\langle \delta\psi | \mathcal{H} - E | \psi \rangle = 0. \quad (2.20)$$

Here we have introduced a Langrange multiplier to ensure orthogonality of our trial wave function to infinitesimal variations, and this Langrange multiplier is easily identified as the total energy of the system. This is the most general variational principle that we use in treating both bound ( $E < 0$ ) and continuum ( $E > 0$ ) states. A similar derivation for continuum states can be performed, resulting in the same equation [25, 45].

## 2.2.3 Hartree-Fock and Hartree-Slater Methods for Bound States

### Hartree-Fock Method

Our aim is to find the radial orbitals  $P_{nl}(r)$  in Eq. 2.3 satisfying the orthonormality conditions; orbitals with different principal quantum number and the same orbital angular quantum numbers must be orthonormal,  $\int_0^\infty P_{nl}(r)P_{n'l}(r)dr = \delta_{nn'}$ . For simplicity, we deal with the spatial part of the wave functions,  $\varphi_i(\vec{r})$  in Eq. 2.3, rather than the radial orbitals,  $P_{n_i l_i}(r)$ . Then the orthonormality condition is given as  $\langle \varphi_i | \varphi_j \rangle = \int \varphi_i(\vec{r})\varphi_j(\vec{r})d^3r = \delta_{ij}$ .

We want the total energy of the system to be stable under variations of the single-electron orbitals, with the orthonormality conditions stated above. This can be achieved by using the variational method with Lagrange multipliers, as discussed in Section 2.2.2. As can be shown [30], our variational Eq. 2.20 takes a more general form considering Lagrange multipliers  $\Lambda_{ij}$  to impose orthogonality conditions,

$$\delta(\langle \mathcal{H} \rangle - \sum_{i < j=1}^N \Lambda_{ii} \langle \varphi_i(1) | \varphi_i(1) \rangle + \delta_{m_{s_i} m_{s_j}} \Lambda_{ij} \langle \varphi_i(1) | \varphi_j(1) \rangle) = 0,$$

where a variation with respect to the orbital  $|\varphi_i\rangle$  is considered. This can be rewritten as

$$\begin{aligned} & \sum_{i=1}^N \{ \langle \delta\varphi_i(1) | f(1) | \varphi_i(1) \rangle + \langle \varphi_i(1) | f(1) | \delta\varphi_i(1) \rangle \} + \\ & \sum_{i < j=1}^N \{ \langle \delta\varphi_i(1) \varphi_j(2) | g(1, 2) | \varphi_i(1) \varphi_j(2) \rangle + \langle \varphi_i(1) \varphi_j(2) | g(1, 2) | \delta\varphi_i(1) \varphi_j(2) \rangle \} - \\ & \sum_{i < j=1}^N \{ \langle \delta\varphi_i(1) \varphi_j(2) | g(1, 2) | \varphi_j(1) \varphi_i(2) \rangle + \langle \varphi_i(1) \varphi_j(2) | g(1, 2) | \varphi_j(1) \delta\varphi_i(2) \rangle \} = \\ & \sum_{i=1}^N \Lambda_{ii} \{ \langle \delta\varphi_i(1) | \varphi_i(1) \rangle + \langle \varphi_i(1) | \delta\varphi_i(1) \rangle \} + \sum_{i < j=1}^N \delta_{m_{s_i} m_{s_j}} \Lambda_{ij} \langle \delta\varphi_i(1) | \varphi_j(1) \rangle, \end{aligned}$$

that can be further split into two terms that are complex conjugate of each other, giving

$$\begin{aligned}
f(1)|\varphi_i(1)\rangle &+ \sum_{j \neq i=1}^N \{ \langle \varphi_j(2) | g(1,2) | \varphi_j(2) \rangle |\varphi_i(1)\rangle \\
&- \delta_{m_{s_i} m_{s_j}} \langle \varphi_i(2) | g(1,2) | \varphi_j(2) \rangle |\varphi_j(1)\rangle \} \\
&= \Lambda_{ii} |\varphi_i(1)\rangle + \sum_{j \neq i=1}^N \delta_{m_{s_i} m_{s_j}} \Lambda_{ij} |\varphi_j(1)\rangle . \quad (2.21)
\end{aligned}$$

If  $\Lambda_{ij}$  represents elements of the matrix  $\Lambda$ , and since  $\Lambda_{ji}^* = \Lambda_{ij}$ , then  $\Lambda$  is Hermitian. Thus, there exists a unitary transformation that diagonalizes the matrix of Lagrange multipliers,  $U\Lambda U^{-1} = \varepsilon$ , where  $\varepsilon$  is a diagonal matrix with eigenvalues  $\varepsilon_i$ . Our wave function transforms as  $\Psi = U\psi$ . This transformation of spin-orbitals doesn't alter the Slater determinantal wave function due to unitarity. Therefore, this equation is invariant under the above unitary diagonalizing transformation, and this operation will eliminate non-diagonal  $\Lambda_{ij}$  terms. In this new representation, Eq. 2.21 now reads as

$$\begin{aligned}
f(1)|\varphi_i(1)\rangle &+ \sum_{j \neq i=1}^N \{ \langle \varphi_j(2) | g(1,2) | \varphi_j(2) \rangle |\varphi_i(1)\rangle \\
&- \delta_{m_{s_i} m_{s_j}} \langle \varphi_i(2) | g(1,2) | \varphi_j(2) \rangle |\varphi_j(1)\rangle \} = \varepsilon_i |\varphi_i(1)\rangle . \quad (2.22)
\end{aligned}$$

These are the well-known Hartree-Fock equations [30, 31, 32, 46, 47, 48]. A further simplification arises if we define the following operators

$$I(1)|\varphi_i(1)\rangle = \langle \varphi_i(1) | f(1) | \varphi_i(1) \rangle \quad \text{the one-electron operator,}$$

$$J_j(1,2)|\varphi_i(1)\rangle = \langle \varphi_j(2) | g(1,2) | \varphi_j(2) \rangle |\varphi_i(1)\rangle \quad \text{the direct/Coulomb operator,}$$

$$K_j(1,2)|\varphi_i(1)\rangle = \langle \varphi_j(2) | g(1,2) | \varphi_i(2) \rangle |\varphi_j(1)\rangle \quad \text{the exchange operator.}$$

Here,  $I(1)$  represents the kinetic energy and electron-nucleus interaction operator,  $J_j(1,2)$  can be interpreted as the electrostatic potential of the electron  $i$  due to electron  $j$ , and

$K_j(1, 2)$  has no classical interpretation and owes its existence to the required antisymmetry of the wave function (or, equivalently, the indistinguishability of the electrons). In terms of these operators, the Fock operator is defined as  $\mathcal{F}(1) = I(1) + \sum_{j \neq i} \{J_j(1, 2) - \delta_{m_{s_i}, m_{s_j}} K_j(1, 2)\}$ , and Eq 2.22 becomes an eigenvalue equation for all one electron energies  $\varepsilon_i$ ,

$$\mathcal{F}(1)|\varphi_i(1)\rangle = \varepsilon_i|\varphi_i(1)\rangle,$$

with eigenvectors  $\varphi_i(1)$ . Since the Hartree-Fock method is based on a variational principle, it only provides an upper limit to the energy of the state. And since the HF equations are coupled, non-linear integro-differential equations, they can only be solved numerically by using iterative methods. This requires an initial "seed" of basis orbitals, and these are chosen to be hydrogenic. In the iterative procedure,  $I(1)$ ,  $J_j(1, 2)$ ,  $K_j(1, 2)$ , and  $\mathcal{F}(1)$  are first calculated, and with these calculated values, Eq. 2.23 is solved for new  $\varepsilon_i$  and new  $\varphi_i$ . The new spin-orbitals are now used as the initial orbitals in a new iteration and a new energy is computed, continuing until desired convergence is obtained. This general method of solution is known as the Hartree-Fock self-consistent field (HF-SCF) method [30]: each electron is an eigensolution of a potential due to the nucleus and the charge distribution of all other (N-1) electrons.

### **Hartree-Slater Method**

Following Zener's pioneering work on the analytic wave functions with variational parameters [49], Slater developed an empirical approximation for the screening of electrons in an atom that can then be used to determine the radial orbitals [50]. The spin orbital of an

electron in a shell  $i = \{n_i l_i\}$  can be written as

$$P_i(r) = c \rho_i^{n_i} e^{\rho_i r/2}, \quad (2.23)$$

where  $c$  is a normalization factor and  $\rho_i = 2z_i r/n_i$ . The *effective charge* seen by the electron in the  $i$ -shell is given by

$$z_i = Z - \frac{(w_i - 1)}{2} - \sum_{j < i} w_j. \quad (2.24)$$

Here,  $Z$  is the nuclear charge,  $w_j$  is the number of electrons occupying the  $j^{\text{th}}$  shell, and thus the second term represents the approximate screening of all other  $w_i - 1$  equivalent electrons, each of which screens on average by a charge of  $1/2$ . The third term with the  $j < i$  restriction represents the full approximate screening from all more tightly bound electrons. Note that we assume the average energies and radii are ordered numerically ( $E_i < E_{i+1}$  and  $\langle r_i \rangle < \langle r_{i+1} \rangle$ ).

Using these orbitals, the effective spherical potential for an electron due to the nucleus and all other electrons can be determined as follows [21, 51, 52, 53]. The screening at any radius  $r$  due to an electron  $j$  can be calculated by using the charge density of the electron,  $\int |\varphi_j(\vec{r})|^2 d\Omega = P_j^2(r)$ . The total screening due to all other electrons then can be written as

$$S_i(r) = \sum_{j \neq i=1}^N \frac{\int_0^r P_j^2(r') dr' + r \int_r^\infty r'^{-1} P_j^2(r') dr'}{\int_0^\infty P_j(r') dr'}, \quad (2.25)$$

where the two terms are attributed to inner ( $r' < r$ ) and outer ( $r' > r$ ) screenings, respectively. The relation between effective nuclear charge and the potential for one electron can

be written as

$$V_i(r) = -\frac{Z_i^{eff}(r)}{r} = -\frac{(Z - S_i(r))}{r}. \quad (2.26)$$

The screening factors are now determined for each shell by evaluating the integrals\* in Eq. 2.25 by using the orbitals from Eq. 2.23 with the screening parameters from Eq. 2.24. The effective potential, including the influence of the nuclear charge and the other electrons for electron  $i$ , is determined as

$$V_i(r) = -\frac{1}{r} \left\{ Z - \sum_j (w_j - \delta_{ij}) \left[ 1 - \frac{e^{-\rho_j}}{2n_j} \sum_{m=0}^{2n_j-1} \frac{(2n_j - m)}{m} \rho_j^m \right] \right\},$$

a local potential that is used to determine the radial orbitals within the central-field approximation.

To gain greater flexibility and control over the determination of the radial orbitals, scaling parameters [51] can be defined for the STO-Hartree-Slater potentials,  $V_i(\zeta) = V_i(r, \alpha_i)$ .

These parameters are defined as

$$\zeta_i = \frac{r}{\alpha_i}$$

and can be used as additional variational parameters in the energy-optimization procedure.

In our calculations, we have opted not to use scaling parameters, but instead we use  $\alpha_i = 1$ .

In order to determine the bound orbitals,  $P_i(r)$ , this STO-Hartree model potential may be replaced with the electron-nucleus and electron-electron Coulomb potentials in Eq. 2.1 as demonstrated in Sec. 2.2.1 within a central-field approximation. The radial equation for

---

\*  $\int F_m(x) e^{-ax} dx = -\frac{e^{-ax}}{a} \sum_{k=0}^m \frac{F_m^{(k)}(x)}{a^k}$ , where  $F_m(x)$  is a polynomial function of  $x$  of degree  $m$  and  $F^{(k)}(x)$  is the  $k^{\text{th}}$  derivative of  $F_m(x)$  with respect to  $x$ .

any given  $i = nl$  shell orbital described by  $P_{nl}(r)$  is

$$\left[ \frac{d^2}{dr^2} - \frac{l(l+1)}{r^2} + \frac{2Z_{nl}^{eff}(r)}{r} + 2E_{nl} \right] P_{nl}(r) = 0. \quad (2.27)$$

Let us now look for the solutions of this equation near the origin ( $r \rightarrow 0$ ) and at asymptotic ( $r \rightarrow \infty$ ) values. The solution of the equation at large  $r$  values is

$$\lim_{r \rightarrow \infty} P_{nl}(r) = z r^{\nu_{nl}-1} e^{-zr/\nu_{nl}}$$

where  $E_{nl} = -\frac{z^2}{2\nu_{nl}^2}$  and  $z = Z_{nl}^{eff}(\infty) = Z - (N - 1)$ , where  $N - 1$  is the number of other electrons. The solution in the neighborhood of the origin is

$$\lim_{r \rightarrow 0} P_{nl}(r) = \bar{P}_{nl}(0) r^{l+1} \left\{ 1 - \frac{Z_{nl}^{eff}(0)r}{l+1} + \mathcal{O}(r^2) \right\},$$

with normalization condition

$$\int_0^\infty P_{nl}(r) P_{nl}(r) dr = 1.$$

The orbitals  $P_{nl}(r)$  can be determined by matching asymptotic ( $r \rightarrow \infty$ ) and inner-region ( $r \rightarrow 0$ ) solutions at intermediate  $r$ , yielding an eigenvalue equation for the allowed bound states  $E_{nl} < 0$ , thereby quantizing energies according to nodal behavior ( $n - l + 1$ ) and angular behavior encompassed in the  $Y_l^{ml}(\Omega)$  term and the  $l(l+1)/r^2$  centrifugal term for  $P_{nl}(r)$ . This iteration procedure is terminated when desired convergence is obtained for  $E_{nl}$ .

#### 2.2.4 Configuration Interaction

Up to this point, we have considered only what is known as a single-configuration (SC) approximation: the wave function is a single Slater determinant for simpler cases but a

linear combination of Slater determinants involving permutations within one set of *configuration* orbitals. For instance, the excited state  $1s2s(^1S)$  in He is described as

$$\psi^{\text{SC}}(1s2s(^1S)) = \frac{1}{\sqrt{2}} \left\{ \frac{1}{\sqrt{2}} \begin{vmatrix} \phi_{1s}\chi_+(1) & \phi_{1s}\chi_+(1) \\ \phi_{2s}\chi_-(2) & \phi_{2s}\chi_-(2) \end{vmatrix} + \frac{1}{\sqrt{2}} \begin{vmatrix} \phi_{1s}\chi_-(1) & \phi_{1s}\chi_-(1) \\ \phi_{2s}\chi_+(2) & \phi_{2s}\chi_+(2) \end{vmatrix} \right\}.$$

Note that these all include the single configuration permutations of spatial  $1s$  and  $2s$  space and  $\chi_{+,-}$  spin assignments within the configuration.

However, there also exist the important *configuration interaction* (CI). For instance, the ground state of Be-like ions is described as  $1s^22s^2$  in a SC description whereas the most important CI involves the  $2s^2 - 2p^2$  intra-shell correlation, giving a CI wave function

$$\psi^{\text{CI}}(1s^22s^2(^1S)) = c_1 \psi^{\text{SC}}(1s^22s^2(^1S)) + c_2 \psi^{\text{SC}}(1s^22p^2(^1S)),$$

where we find that the mixing ratio  $|c_2/c_1|^2 \approx 0.08$  in our calculations along the isoelectronic sequence  $4 \leq Z \leq 30$ .

In general, CI wave functions can be taken as a mixture of states from different configurations with the same final symmetry as

$$\Psi_i = \sum_{j=1}^K c_{ij} \psi_j, \quad \text{where } c_{ij} = \langle \psi_j | \Psi_i \rangle. \quad (2.28)$$

Here,  $c_{ij}$  are the mixing coefficients and  $\psi_i$  are the eigenfunctions of the Hamiltonian,  $\mathcal{H}$ .

Hence, they are orthonormal:  $\langle \psi_i | \psi_j \rangle = \delta_{ij}$ .

One can include these (sometimes very important, see Sec. 3.1) additional configurations in one of two ways. In the multi-configuration Hartree-Fock (MCHF) approach, the

expansion coefficients  $c_i$ , in addition to the orbitals  $\phi_i(\vec{r})$ , are optimized simultaneously. As a second approximation, the orbitals are determined from HF or HS methods, and then further variations are only considered for the mixing coefficients, as follows. The variation with respect to mixing coefficients  $c_{ij}$ , to minimize the energies  $E_i$ , yield the following eigenvalue equations

$$\sum_{j=1}^K (H_{ij} - \delta_{ij} E_i) c_{ij} = 0, \quad (2.29)$$

where  $H_{ij} = \langle \psi_i | \mathcal{H} | \psi_j \rangle$ . The energies  $E_i$  can be determined from the determinantal equation

$$|H_{ij} - E_i \delta_{ij}| = 0.$$

These energies  $E_i$  are then used in Eq. 2.29 to solve for the mixing coefficients  $c_{ij}$ . In our calculations, the CI expansion is considered for both LS- and IC-coupling wave functions.

### 2.2.5 Distorted Wave Approximation for Continuum Orbitals

In the so-called distorted wave approximation, the continuum (scattered) electron is assumed to move in a spherically symmetric potential due to the  $(N - 1)$ -electron target electrons and the nucleus (“distortion” refers to the short-range, non-Coulombic inter-electron interaction). In our MCBP calculations, this potential is chosen to be a STO-Hartree potential as given in Eq. 2.27. The radial equation for a continuum electron with angular momentum  $l_i$  and wavenumber  $k_i$  can be written as

$$\left[ \frac{d^2}{dr^2} - \frac{l_i(l_i + 1)}{r^2} - 2V_i(r) + k_i^2 \right] F_{k_i l_i}(r) = 0. \quad (2.30)$$

where the index  $i$  is used to define the electron configuration of the target state,  $V_i(r)$  is the local potential due to the nucleus and all  $(N - 1)$  target electrons,  $k_i$  is the wavenumber, defined as  $k_i^2 = 2E > 0$ , and  $E$  is the energy of the continuum electron. The asymptotic solutions of these equations are

$$\lim_{r \rightarrow 0} F_{k_i l_i}(r) = \bar{F}_{k_i l_i}(0) r^{l_i+1}$$

$$\lim_{r \rightarrow \infty} F_{k_i l_i}(r) = k_i^{-1/2} \sin \left\{ k_i r + \frac{z}{k_i} \ln(2k_i r) - \frac{l_i \pi}{2} + \arg \Gamma(l_i + 1 - \frac{iz}{k_i}) + \delta \right\}$$

where  $z$  is the ionic charge defined as  $z = Z - (N - 1)$  and the  $\delta$  is the distorted-wave phase-shift. Note that, for a purely Coulombic potential,  $V_i(r) = (Z - N + 1)/r$ , the distorted wave phaseshift is zero,  $\delta = 0$ . As we have described in Sec. 2.2.3 for bound states, these continuum distorted wave solutions are determined by using a similar integration method and imposing the orthogonality conditions  $\langle F_{k_i l_i} | P_{n l_i} \rangle = 0$ .

### 2.3 Multi-Configuration Breit-Pauli Method

In our multi-configuration Breit-Pauli method, the  $N$ -electron Hamiltonian includes both non-relativistic and additional relativistic terms as given in Eq. 2.9. The final wave functions are described in an IC-coupling scheme (see Eq. 2.10) and taken in the form of a multi-configuration expansion to include electron correlation effects

$$\Psi(\gamma_i J M_J) = \sum_{j=1}^{N_c} c_{ij} \psi(\gamma_j J M_J) . \quad (2.31)$$

Here, the SC states  $\psi(\gamma_j J M_J)$  are determined from a HS method in a non-orthogonal basis\*,  $N_c$  is the number of states included in the expansion, and  $c_{ij}$  are the mixing co-

---

\*A separate non-orthogonal set of orbitals is used for each configuration, thereby accounting for orbital relaxation effects.

efficients. The energies and mixing coefficients are obtained from the minimization of the energy with respect to the mixing coefficients (see Sec. 2.2.4 for CI), yielding the CI form of the variational equation as given in Eq. 2.29. If we define  $\mathbf{c}$  as a  $N_c \times N_c$  matrix whose elements are the mixing coefficients  $c_{ij}$  and  $\mathbf{H}$  as a  $N_c \times N_c$  matrix whose elements are the Hamiltonian matrix elements,  $H_{ij} = \langle \psi(\gamma_i JM_J) | \mathcal{H}_{BP} | \psi(\gamma_j JM_J) \rangle$ , the variational equation reads as

$$(\mathbf{H} - \mathbf{E} \mathbf{I})\mathbf{c} = \mathbf{0}, \quad (2.32)$$

where  $\mathbf{I}$  is the  $N_c \times N_c$  unit matrix. The eigenvalues  $E_i$  are determined from the determinantal equation,  $|\mathbf{H} - \mathbf{E} \mathbf{I}| = 0$ , giving eigenvectors in the columns of the matrix  $\mathbf{c}$ .

In our calculations, the code AUTOSTRUCTURE calculates the energies of these CI-levels (terms in an LS-coupling scheme) and the corresponding mixing coefficients. Then, level to level dipole transition rates, using both length and velocity forms of the dipole operator (see Sec. 2.1.3), and Auger transition rates are computed.

Another challenge of our calculations is in the use of non-orthogonal sets of orbitals, one set for each configuration. Thus, relaxation effects due to different screening in the initial and final states are taken into account. In this method, the only approximation involved is that overlap integrals are assumed to be unity or zero,  $\int_0^\infty P_{nl}^i(r) P_{n'l}^j(r) dr \approx \delta_{nn'}$ , where  $i$  defines the configuration for which the orbital is optimized.

## 2.4 R-Matrix Method

The R-matrix method was first introduced to study the resonance reactions in nuclear physics [22, 23] and subsequently developed and widely used in nuclear physics [24]. Later

application to atomic physics was pioneered by Burke and coworkers [25, 26, 27, 54, 55, 56].

In this method, configuration space is divided into two regions by a sphere of radius  $r = a$ , where  $r$ , for electron-ion interactions, refers to the position of the scattering electron relative to the nucleus. The R-matrix boundary,  $r = a$ , is chosen such that all electron orbitals in the target vanish at the boundary,  $r = a$ . In the internal region  $r < a$ , the interaction between the scattering electron and the target electrons is the strongest and the most complicated. In the external region  $r > a$ , on the other hand, the interaction between the scattering electron and all target electrons is given by a simple long-range multiple potential of the target. The wave functions are solved in both regions, and inverse logarithmic boundary conditions (continuity of inner and outer R-matrices) are used to match the inner and outer solutions in order to determine the scattering or bound wave functions.

The wave function  $\Psi(q_1, q_2, \dots, q_{N+1})$  for the  $(N + 1)$ -electron system, including  $N$ -electron target states coupled to the scattered electron, is a variational approximation to the Schrödinger equation

$$\mathcal{H}^{N+1}\Psi(q_1, q_2, \dots, q_{N+1}) = E\Psi(q_1, q_2, \dots, q_{N+1}), \quad (2.33)$$

where  $\mathcal{H}^{N+1}$  is the  $(N + 1)$ -electron Hamiltonian ( $N$  is replaced with  $N + 1$  in Eq. 2.1).

Let us first look at the  $N$ -electron target and the  $(N + 1)$ -electron scattering solutions in the inner region. The wave functions for  $N$ -electron targets state are considered in the

form of a CI expansion in terms of a chosen basis of configurations as

$$\Phi_i(q_1, q_2, \dots, q_N) = \sum_j b_{ij} \phi_j(q_1, q_2, \dots, q_N). \quad (2.34)$$

Here,  $\phi_j$  are the SC electron wave functions of Slater determinant form as discussed in Sec.2.2.1. The mixing coefficients  $b_{ij}$  can be determined from the following eigenvalue equation along with the energies

$$\langle \Phi_i | \mathcal{H}^N | \Phi_j \rangle = \delta_{ij} E_i^N, \quad (2.35)$$

where  $\mathcal{H}^N$  is the  $N$ -electron Hamiltonian given in Eq. 2.1 (here we use  $\mathcal{H}^N$  to distinguish from the  $(N + 1)$ -electron Hamiltonian,  $\mathcal{H}^{N+1}$ ).

For the solutions  $\Psi$ , we need to solve Eq. 2.33 in this region. However, due to the surface terms that are involved due to the  $\frac{d^2}{dr^2}$  kinetic energy operator, the Hamiltonian  $\mathcal{H}^{N+1}$  is non-Hermitian for the interval  $0 \leq r \leq a$ , that is,  $\mathcal{H}^{N+1} \neq \mathcal{H}^{N+1\dagger}$ . To cancel these surface terms, the Bloch operator [24, 57] is introduced as

$$L^{N+1} = \sum_{i=1}^{N+1} \frac{1}{2} \delta(r_i - a) \left( \frac{d}{dr_i} - \frac{b-1}{r_i} \right),$$

where  $b$  is an arbitrary constant, and can be used in conjunction with  $\mathcal{H}^{N+1}$  to yield a Hermitian-operator eigenvalue equation

$$(\mathcal{H}^{N+1} + L^{N+1} - E)\Psi = L^{N+1}\Psi. \quad (2.36)$$

In order to solve this equation, we look for solutions that satisfy the following eigenvalue equation,

$$(\psi_i | \mathcal{H}^{N+1} + L^{N+1} | \psi_j) = E_i \delta_{ij}. \quad (2.37)$$

Since we must have an antisymmetric wave function with respect to interchange of two electrons, we antisymmetrize, and include additional  $(N + 1)$ -electron "correlation" configurations as

$$\psi_k = \mathcal{A} \sum_{ij} c_{ijk} \bar{\Phi}_i(q_1, q_2, \dots, q_N; q_{N+1}) \frac{1}{r_{N+1}} u_{ij}(r_{N+1}) + \sum_j d_{jk} \Theta_j(q_1, q_2, \dots, q_{N+1}),$$

where  $\mathcal{A}$  is the antisymmetrization operator. The channel wave functions  $\bar{\Phi}_i$  are constructed by coupling target wave functions  $\Phi_i$  to a scattered electron orbital  $u_{ij}(r)$ . The  $\Theta_j$  are additional  $(N + 1)$ -electron wave functions constructed from the bound  $P_{nl}(r)$  basis, and are included to compensate for the enforced orthogonality condition  $\langle P_{nl} | u_{il} \rangle = 0$ . The continuum/valance basis orbitals  $u_{ij}(r)$  for each angular momentum  $l_i$  are typically taken to satisfy the physically-motivated model-potential equation

$$\left( \frac{d^2}{dr^2} - \frac{l_i(l_i + 1)}{r^2} + V_0(r) + k_{ij}^2 \right) u_{ij}(r) = \sum_n \Lambda_{inl} P_{nl}(r), \quad (2.38)$$

with the following boundary conditions,

$$\begin{aligned} u_{ij}(0) &= 0, \\ \left( \frac{a}{u_{ij}(a)} \right) \left( \frac{du_{ij}(r)}{dr} \right)_{r=a} &= b. \end{aligned} \quad (2.39)$$

Here  $\Lambda_{inl}$  are Langrange multipliers used to ensure the orthogonality between the continuum and the bound orbitals,  $\langle P_{nl} | u_{il} \rangle = 0$ , and  $b$  is an arbitrary constant. The expansion coefficients  $c_{ijk}$  and  $d_{ik}$  are determined from the eigenvalue equation (Eq. 2.37). We note that this  $M \times M$  equation constitutes  $2M$  linearly-independent solutions, but given the  $\Psi \xrightarrow{r \rightarrow 0} 0$  boundary conditions, we only have  $M$  remaining.

Following Wigner's one channel case [22], computation of the R-matrix can be generalized to  $M$  channels [24] as follows. Surface amplitudes are defined as the projection of the basis functions on the target states,  $a^{-1}w_{ik} = \langle \bar{\Phi} | \psi_k \rangle'_{r=a}$ , where the prime is used to indicate that the integrals are limited to bound orbitals in the target state. In terms of the surface amplitudes, the R-matrix is analytically shown to take the simple form

$$R_{ij}(E) = \frac{1}{2r} \sum_k \frac{w_{ik}(r)w_{kj}(r)}{E_k - E}, \quad (2.40)$$

where the sum is taken over each channel  $k$ . In the outer region, since the scattered electron and the target electrons interact weakly, the outer solution can be written without antisymmetrization in the form of a CI expansion as

$$\Psi_{out}(q_1, q_2, \dots, q_N; q_{N+1}) = \sum_i \bar{\Phi}_i(q_1, q_2, \dots, q_N; q_{N+1}) \frac{1}{r_{N+1}} F_i(r_{N+1}). \quad (2.41)$$

We seek solutions by substituting  $\Psi_{out}$  into the Schrödinger equation, yielding the following radial equation for each channel  $i$ :

$$\left( \frac{d^2}{dr^2} - \frac{l_i(l_i + 1)}{r^2} + \frac{2Z}{r} + k_i^2 \right) F_{ij}(r) = 2 \sum_{j=1}^M V_{ij}(r) F_{ij}(r). \quad (2.42)$$

Here,  $k_i$  is the channel energy and defined in terms of the target energies as  $k_i^2 = 2(E - E_i^N)$ , and  $V_{ij}$  is the potential matrix, determined from the electrostatic Coulomb potential induced by the target states as

$$V_{ij}(r) = \langle \bar{\Phi}_i | \sum_{m=1}^N \frac{1}{r_{N+1}} | \bar{\Phi}_j \rangle. \quad (2.43)$$

The external solutions  $F_{ij}(r)$  are obtained by solving Eq. 2.42 subject to the following

asymptotic solutions

$$F_{ij}(r) \underset{r \rightarrow \infty}{\sim} \begin{cases} k_i^{-1/2} [\sin(\theta_i) + \cos(\theta_i)K_{ij}] & k_i^2 > 0 \text{ open channels} \\ e^{-\phi_i} \delta_{ij} & k_i^2 < 0 \text{ closed channels,} \end{cases}$$

where  $\mathbf{K}$  is defined as the reactance matrix, and  $\theta_i$  and  $\phi_i$  are defined as

$$\theta_i = k_i r - \frac{1}{2} l_i + \pi \frac{z}{k_i} \ln 2k_i r + \arg \Gamma(l_i + 1 - i \frac{z}{k_i})$$

$$\phi_i = |k_i| r - \frac{z}{|k_i|} \ln(2|k_i| r).$$

Here  $z$  is the ionic charge defined as  $z = Z - N$ .

Since the R-matrix must match smoothly between the inner and outer regions solutions at the boundary  $r = a$ , we have

$$\mathbf{R}_{in}(E, r = a) [a \Psi'_{out}(E, a)] = \Psi_{out}(E, a). \quad (2.44)$$

This boundary condition gives us the solution for the reactance matrix  $\mathbf{K}$ , from which the scattering matrix is determined as

$$\mathbf{S} = \frac{1 + i\mathbf{K}}{1 - i\mathbf{K}}. \quad (2.45)$$

Knowledge of S-matrix-normalization of the continuum states  $\Psi_f$  allows the photoabsorption cross section [58] to be computed from an initial state  $\Psi_i$  as

$$\sigma^{\text{PA}}(E) = \frac{4\pi^2 w}{3c} |\langle \Psi_f | \mathcal{D} | \Psi_i \rangle|^2. \quad (2.46)$$

For  $E < 0$ , on the other hand, we get an eigenvalue equation for the binding energy and the wavefunction  $\Psi_i$  of the initial state.

### 2.4.1 Smith Time-Delay Method

The method we use for determining the Auger width of a decaying resonance from our R-matrix calculations relies on studying the analytical properties of the Smith time-delay matrix [59]. In this method, the lifetime matrix  $\mathbf{Q}$  is defined in terms of the scattering matrix  $\mathbf{S}$  in Eq. 2.45 as

$$\mathbf{Q} = -i\mathbf{S}^\dagger \frac{d\mathbf{S}}{dE}. \quad (2.47)$$

The trace of this matrix has an analytic Lorentzian form

$$\text{Tr}\{\mathbf{Q}(E)\} = \frac{\Gamma}{(E - E_R)^2 + \left(\frac{\Gamma}{2}\right)^2}, \quad (2.48)$$

where  $\Gamma$  is the width of the decaying resonance and  $E_R$  is the position of the resonance. We have used the R-matrix method to study the scattering of electrons from an  $N$ -electron target state to determine the decay widths of the corresponding  $(N+1)$ -electron resonances. By using the computed reactance matrix  $\mathbf{K}$  in Eq. 2.45, the  $\mathbf{S}$  matrix is determined, from which the  $\mathbf{Q}$  matrix is computed using Eq. 2.47. The Auger width  $\Gamma$  is then determined from the Lorentzian fit of  $\text{Tr}\{\mathbf{Q}\}$  for a particular resonance near its position  $E_R$ , as given in Eq. 2.48. In this method, identification of the resonance and determination of  $\Gamma$  can be difficult when overlapping resonances occur. In such cases, multi-resonance fitting must be considered.

## CHAPTER III

### RESULTS AND DISCUSSIONS

#### 3.1 K-Shell Fluorescence Yields for Isoelectronic Sequences

We have calculated the fluorescence yields of the 2<sup>nd</sup> row-like ions up through Zn. MCBP calculations are carried out using the atomic structure code AUTOSTRUCTURE [13]. The wave functions are described in a non-relativistic framework (see Sec. 2.1.1) and subsequently recoupled to an IC-coupling scheme to include additional relativistic effects as described in Sec. 2.3. The atomic states are taken in the form of non-orthogonal configuration expansions to treat important orbital relaxation and electron correlation effects as described in Sec. 2.2.4. By using these multi-configuration wave functions, level to level radiative and Auger rates are calculated (see Sec. 2.1.3 and Sec. 2.3). By using these level to level transition data, we have found the total radiative and Auger rates for a particular level of interest that influences the fluorescence yields as given in Eq. 1.1. Our results for each of the Li-like, B-like, and C-like isoelectronic sequences are presented in a subsection for each (see Sec. 3.1.1, 3.1.2, and 3.1.3). The rest of the series is not treated in this dissertation, but future plans for the entire series are discussed in Sec. 3.1.4.

##### 3.1.1 Li-Like: Importance of Configuration Interaction

Following the initial survey of Be-like and F-like isoelectronic sequences [12], it became apparent that the Li-like case might be an important sequence as well. This was the first theoretical and computational problem addressed in this dissertation work. In the absence of electron correlation, the Li-like K-shell vacancy system is often described by a

single-configuration (SC) description

$$\Psi^{SC} = 1s2s^2(^2S_{1/2}) \quad . \quad (3.1)$$

Such states are formed either by K-shell ionization of the four-electron  $1s^22s^2$  Be-like system or by inner shell  $1s \rightarrow 2s$  excitation of the three-electron  $1s^22s$  Li-like system.

Since the wave function contains no  $p$ -electrons, decay via an ordinary (electric dipole) transition is not allowed. Thus, the K-shell fluorescence yield is zero at this level of approximation \*

$$\omega_K^{SC} = 0 \quad . \quad (3.2)$$

Indeed, the widely-used database [3] reports a value of zero for the fluorescence yield of every Li-like (K-shell ionized Be-like)  $1s2s^2(^2S_{1/2})$  state.

However, considering many-body interactions in the form of configuration interaction (CI), a more accurate wavefunction is obtained by including the important intra-shell mixing of  $1s2s^2$  and  $1s2p^2$  configurations,

$$\Psi^{CI} = c_1 1s2s^2(^2S_{1/2}) + c_2 1s2p^2(^2S_{1/2}) \quad . \quad (3.3)$$

The crucial aspect of this deviation from the single-configuration wavefunction is that the mixing coefficient  $c_2$  is not small compared to unity. Using AUTOSTRUCTURE [13], our calculations reveal that the mixing coefficient  $c_2$  varies from 0.34 for  $\text{Be}^+$  to 0.32 for  $\text{Zn}^{27+}$ . It is of interest to note that the mixing is nearly constant over a broad range

---

\*Note that a highly-forbidden magnetic dipole transition is in fact possible, but the probability is so small that it is essentially ignorable in this situation.

of ions along the isoelectronic sequence. The result of this significant mixing with the  $1s2p^2$  configuration is that now there can be a substantial probability for this state to decay radiatively via  $1s2p^2 \rightarrow 1s^22p$  radiation, i.e.,  $\omega_K^{CI} \neq 0$ .

The results of our calculations for the K-shell fluorescence yield,  $\omega_K$ , are shown in Fig. 3.1 and tabulated in Table 3.1. Our results show that at the low- $Z$  end, the fluorescence yield remains negligible, although not quite zero. With increasing nuclear charge  $Z$ ,  $\omega_K$  is no longer negligible, rising to a value of almost 0.18 for  $\text{Zn}^{27+}$ . In addition, a significant value of 0.118 is seen for the astrophysically important  $\text{Fe}^{23+}$  ion. This is in good agreement with the multi-configuration Breit-Pauli result of 0.116 [60] using the same code AUTOSTRUCTURE and in fair agreement ( $\approx 10\%$ ) with the multi-configuration Dirac-Fock (MCDF) result of 0.105 [61]. These results are in stark contrast to the currently-used values [3], which are all zero.

We have also developed a two-parameter fitting formula to our theoretical results for easy usage in astrophysical purposes [40] (see also Fig. 3.1 and Table 3.1). The physics underlying the  $Z$ -dependence of  $\omega_K$ , seen in Fig. 3.1, can be explained by considering the modification of expected high- $Z$  scaling of the radiative rate  $A_r$  and the Auger rate  $A_a$  by significant spin-orbit mixing [2]. To begin with, the Auger rate,  $A_a$ , is approximately independent of  $Z$  whereas the radiative rate,  $A_r$ , scales as  $\sim Z^4$ , within the framework of LS-coupling [2] (see also Appendix B for the derivation of the  $Z$ -scaling of the relevant physical variables). With increasing  $Z$ , however, the spin-orbit interaction becomes increasingly important, and perturbs the  $Z^4$  dependence of  $A_r$  with a small, negative contribution which scales as  $\sim Z^7$ . This suggests that the fluorescence yield,

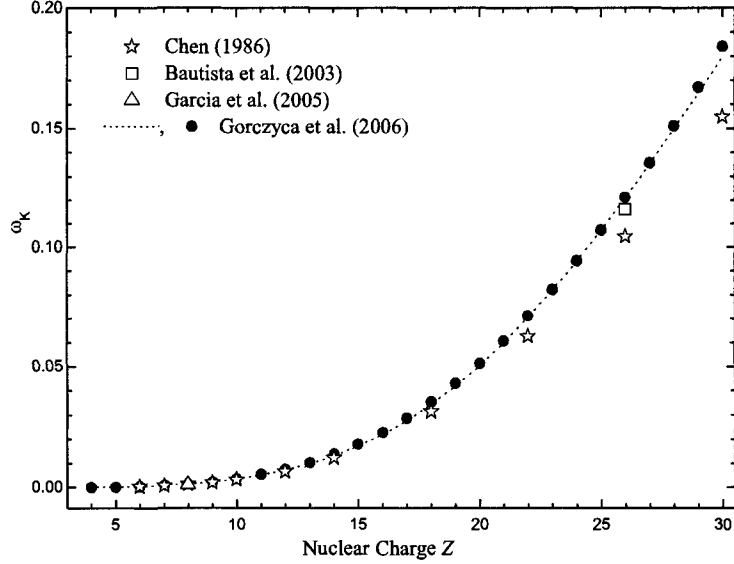


**Figure 3.1** Calculated fluorescence yields (circles) and fit formula (dashed line) for K-shell vacancy Li-like ions. Available data from other theoretical sources [16, 60, 61] are also shown, indicating the generally-good agreement between our complete-series results and the selected ions computed by other theorists.

$\omega_K \equiv A_r / (A_r + A_a) = (1 + 1/[A_r/A_a])^{-1}$ , can be well approximated by the fitting formula

$$\omega_K^{fit} \approx \left(1 + \frac{1}{aZ^4 - bZ^7}\right)^{-1}. \quad (3.4)$$

Fitting the above functional form to our calculated  $\omega_K^{CI}$ , we obtain  $a = 3.57 \times 10^{-7}$  and  $b = 3.2 \times 10^{-12}$ . The resulting  $\omega_K^{fit}$  is shown in Fig. 3.1 and tabulated in Table 3.1. The agreement with  $\omega_K^{CI}$  is seen to be quite good except at very low  $Z$  where the fluorescence yield is negligible anyway. This disagreement occurs because the approximate scaling is invalid at such low  $Z$ . It should be emphasized that this fitting is based on the important physics for  $Z \leq 30$ ; for higher  $Z$ , the above perturbative approach for the spin-orbit interaction is inaccurate and the fitting formula, Eq. 3.4, breaks down. In any event, since the  $1s2p^2 \rightarrow 1s^22p$  radiative rate eventually dominates the Auger rate, the asymptotic  $Z \rightarrow \infty$

fluorescence yield,  $\omega_K$ , is equal to unity, in sharp contradiction to the latest database in use that reports all these values as zero [3].

**Table 3.1** Fluorescence yield  $\omega_K$  vs. nuclear charge  $Z$  for the intermediate-coupling, CI-mixed Li-like  $1s2s^2(^2S_{1/2})$  state.

$Z$	$\omega_K^{CI}$	$\omega_K^{fit}$	$Z$	$\omega_K^{CI}$	$\omega_K^{fit}$
4	0.000076	0.000091	18	0.035187	0.034299
5	0.000210	0.000223	19	0.042622	0.041837
6	0.000459	0.000462	20	0.050939	0.050354
7	0.000874	0.000854	21	0.060142	0.059855
8	0.001512	0.001453	22	0.070221	0.070327
9	0.002437	0.002322	23	0.081161	0.081733
10	0.003718	0.003526	24	0.092939	0.094012
11	0.005427	0.005138	25	0.105530	0.107081
12	0.007640	0.007235	26	0.118905	0.120832
13	0.010427	0.009897	27	0.133037	0.135136
14	0.013859	0.013201	28	0.147898	0.149844
15	0.018000	0.017224	29	0.163462	0.164787
16	0.022906	0.022041	30	0.179705	0.179781
17	0.028623	0.027714			

### 3.1.2 B-Like: Breakdown of Configuration-Average Approximation

The five-electron K-shell vacancy  $1s2s^22p^2$  state can couple to one of four LS-terms. These are approximately energy-ordered according to Hund's rule as  $^4P, ^2D, ^2P$  and  $^2S$ . Furthermore, the  $^2P$  term can couple to the  $J = 1/2$  or  $3/2$  IC-levels, the  $^2D$  can couple to the  $J = 3/2$  or  $5/2$  IC-levels, the  $^4P$  term can couple to the  $J = 1/2, 3/2,$  or  $5/2$  IC-levels, and the  $^2S$  LS-term can only couple to the  $J = 1/2$  IC-level. Thus, the  $1s2s^22p^2$  configuration can be in any of eight LSJ-levels. The possible radiative and autoionization

decay pathways for these states are

$$\begin{aligned}
1s2s^22p^2(^{2S+1}L_J) &\xrightarrow{A_{r1}} 1s^22s^22p(^2P_{J'}) + h\nu \\
&\xrightarrow{A_{r2}} 1s^22p^3([^4S, ^2D, ^2P]_{J'}) + h\nu \\
&\xrightarrow{A_{a1}} 1s^22s^2(^1S_0) + e^- \\
&\xrightarrow{A_{a2}} 1s^22s2p(^{1,3}P_{J''}) + e^- \\
&\xrightarrow{A_{a3}} 1s^22p^2([^1S, ^3P, ^1D]_{J'''}) + e^- .
\end{aligned} \tag{3.5}$$

Within a single-configuration description, the radiative rate  $A_{r1}$  equals zero for the initial  $^4P_J$  level due to spin conservation for electric dipole transitions, and the radiative rate  $A_{r2}$  is zero for all LSJ initial levels since this involves a two-electron transition. Also, in the single-configuration approximation, the partial Auger rate  $A_{a1}$  equals zero for the initial  $^4P_J$  and  $^2P_J$  levels due to parity conservation.

We have calculated these decay rates by including  $2s^2 \rightarrow 2p^2$  intrashell correlation - the most important CI effect - as well as semi-relativistic effects, such as the all-important spin-orbit interaction. Our results revealed that the forbidden decay pathway  $A_{r1}$  becomes non-negligible when we take configuration-interaction and semi-relativistic effects into account. Also, we have showed that the fluorescence yields of the eight K-shell vacancy states are strongly LSJ-dependent over the entire isoelectronic sequence [12, 40, 41] (see also Fig. 3.2). To emphasize the strong state dependence, we look at  $Z = 20$ . The lowest fluorescence yield is close to zero, while the largest is seen to be about 0.6. Considering that the fluorescence yield can only vary between 0 and 1, this amounts to an extremely large difference.

Fortunately, other calculations have been performed, allowing us to check the accuracy of our calculations: the fully relativistic MCDF calculations [62] and other MCBP calculations [63], that were performed for certain members of the five-electron isoelectronic sequence. Good agreement is found with MCDF and other MCBP results both qualitatively and quantitatively (see Fig. 3.2 for the particular  $^2D_{3/2}$  and  $^2D_{5/2}$  states).

Note that there is nothing special about the five-electron K-shell-vacancy system. The same general phenomenology should be true for other isoelectronic sequences with fewer than ten electrons (see, for example, Fig. 3.3 for the C-like isoelectronic sequence). The

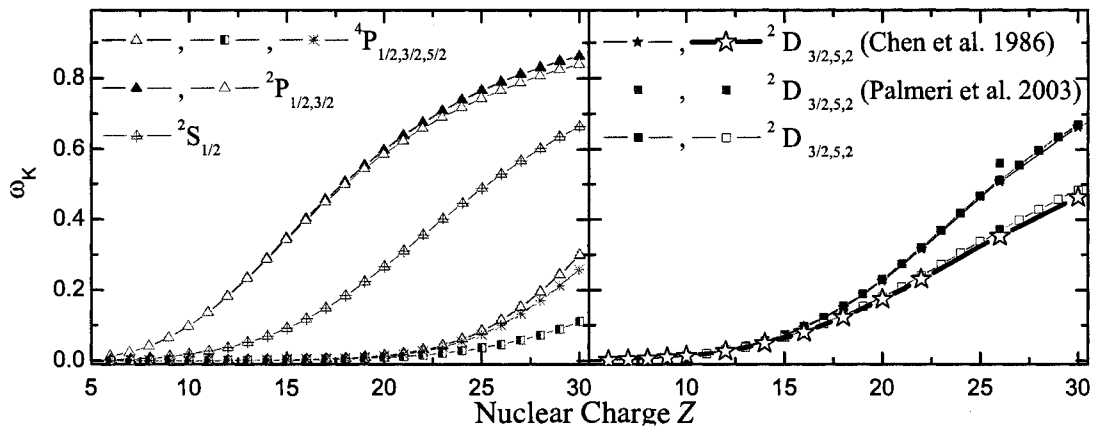


**Figure 3.2** LSJ-dependent fluorescence yields for K-shell vacancy B-like ions. Comparison of fluorescence yields for  $^2D_{3/2}$  and  $^2D_{5/2}$  states.

widely used data compilation [3] contains configuration-averaged fluorescence yields, and these are quite inappropriate for most astrophysical situations. For use in astrophysical modeling codes, then, fluorescence yields, and the radiative and Auger rates associated with them, need to be given for individual LSJ-states; these data can be combined as appropriate for each astrophysical situation. Our aim for future astrophysics-related atomic physics calculations is the compilation, publication, and electronic database creation of all

such rates for all ions of all isoelectronic sequences through the  $2^{nd}$ -row elements. This is because, for a given situation, if configuration averages are sought they cannot be general but must be tailored to the specific astrophysical situation being considered.

For example, we can create a B-like K-shell vacancy state by photoexcitation of  $1s \rightarrow 2p$  in B-like ions or by photoionization of  $1s \rightarrow \varepsilon p$  in C-like ions. To emphasize importance of specific configuration-averaging, let's consider the population of K-shell states following X-ray absorption. For the sake of simplicity, a single-configuration, non-relativistic LS-coupling scheme is considered.

The population of final K-shell vacancy states after  $1s \rightarrow 2p$  photoexcitation of B-like ions, and  $1s \rightarrow \varepsilon p$  photoionization of ground state of C-like ions, yields the following:

*Photoexcitation of B – like Ions :*

$$h\nu + 1s^2 2s^2 2p [^2P]^o \rightarrow 1s 2s^2 2p^2 [^2S, ^2P, ^2D] \quad (3.6)$$

*Photoionization of C – like Ions :*

$$h\nu + 1s^2 2s^2 2p^2 [^3P] \rightarrow 1s 2s^2 2p^2 ({}^2, {}^4P) \varepsilon p [{}^3D, {}^3P, {}^3S]^o . \quad (3.7)$$

Here the ground state of B-like ions and C-like ions are the  ${}^2P$  and  ${}^3P$  terms, respectively. Because a photon is absorbed in either process, the change in total angular momentum of the system will be  $\pm 1$  or 0 and total spin is conserved (see Sec. 2.1.3 for dipole selection rules). For photoexcitation, the  ${}^4P$  term cannot be populated, and specific configuration-averaging should be done over only the doublet terms. For photoionization, only  ${}^4P$  and  ${}^2P$  K-shell-vacancy terms can be populated, and specific configuration-averaging should likewise be considered over only these terms.

### 3.1.3 C-Like: Anomalous Behavior

For C-like K-shell vacancy states, the relevant electronic configuration is  $1s2s^22p^3$ . In an intermediate-coupling scheme, this can be found in one of the ten  $^1P_1^o$ ,  $^3P_{0,1,2}^o$ ,  $^1D_2^o$ ,  $^3D_{1,2,3}^o$ ,  $^3S_1^o$ , and  $^5S_2^o$  levels. The possible decay pathways of these states are

$$\begin{aligned}
 1s2s^22p^3(^{3,5}S_J^o, ^{1,3}P_J^o, ^{1,3}D_J^o) &\xrightarrow{A_{r1}} 1s^22s^22p^2([^1D, ^1S, ^3P]_{J'}) + h\nu \\
 &\xrightarrow{A_{r2}} 1s^22p^4([^1S, ^1D, ^3P]_{J'}) + h\nu \\
 &\xrightarrow{A_{a1}} 1s^22s^22p(^2P_{J''}^o) + e^- \\
 &\xrightarrow{A_{a2}} 1s^22s2p^2([^2S, ^2,4P, ^2D]_{J''''}) + e^- \\
 &\xrightarrow{A_{a3}} 1s^22p^3([^2P, ^2D, ^4S]_{J''''}^o) + e^- . \quad (3.8)
 \end{aligned}$$

Similar to the B-like case, if many-body interaction effects are neglected, some of the decay channels are closed due to selection rules for angular momentum and/or parity;  $A_{r1}$  equals zero for the initial  $^5S_2^o$  level due to spin conservation,  $A_{r2}$  is zero for all initial LSJ levels due to the fact that a two-electron transition is forbidden via an electric dipole interaction, and  $A_{a1}$  is zero for the initial  $^{3,5}S_J^o$  levels due to parity conservation. In our calculations, we have included the strongest electron correlation such as the  $1s \rightarrow 2s$ ,  $1s2s \rightarrow 2p^2$ , and  $2s^2 \rightarrow 2p^2$  promotions. We have performed calculations for all initial levels of the C-like K-shell-vacancy isoelectronic sequence (see Fig. 3.3). The fluorescence yields of each level are again strongly LSJ-dependent, similar to the case of the B-like isoelectronic sequence. For fluorescence yields of C-like K-shell vacancy states, monotonically increasing smooth curves as a function of nuclear charge  $Z$  are found as expected (see Fig 1.2) except for the

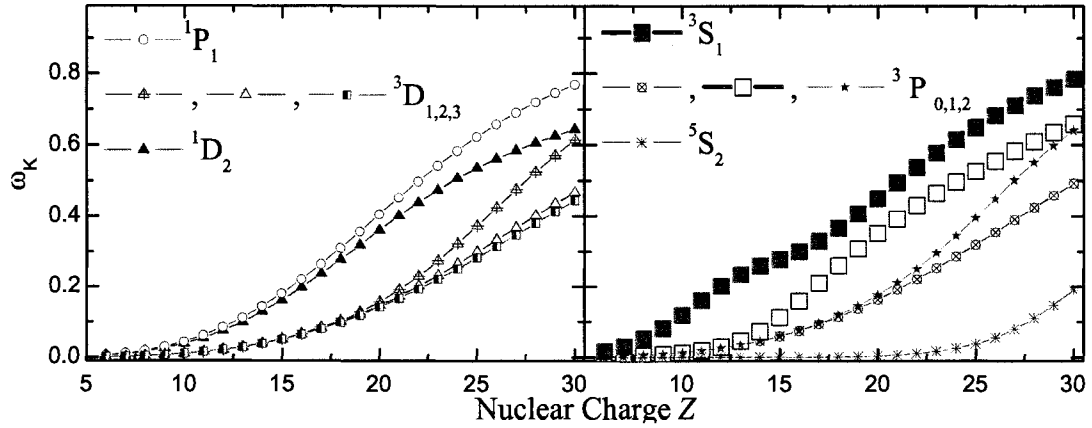


**Figure 3.3** LSJ-dependent fluorescence yields for K-shell vacancy of C-like ions.

$^3P_1$  and  $^3S_1$  states (see Fig. 3.3). The  $^3P_1$  and  $^3S_1$  results exhibit *anomalous* behavior as a function of nuclear charge  $Z$  [42]. This anomalous behavior is more pronounced in the  $A_r$  and  $A_a$  rates of these states (see Fig. 3.4 and Fig. 3.5).

Before proceeding, a second, independent multi-configuration Dirac-Fock (MCDF) method was used to calculate the  $A_r$  and  $A_a$  rates for some members of the K-shell vacancy C-like ions [64]. These calculations were performed using an improved code [65] to treat the low- $Z$  region better [42]. As this approach is based on the full Dirac-Fock equation, including large and small component wave functions, it implicitly includes all one-electron and two-electron relativistic effects. In addition to all relativistic corrections that are introduced perturbatively in the MCBP method, the MCDF method also accounts for the frequency-dependent generalized Breit interaction, and quantum electrodynamics (QED) corrections. For heavy elements, our present MCBP approach using non-relativistic wave functions will be inappropriate since not all relativistic effects can be treated perturbatively.

The new MCDF calculations are carried out using an extended-averaged level scheme [65, 66] for the initial and final states separately, including the same CI expansion from the  $n = 2$  complex as is used for the MCBP calculations (all possible  $2s^i 2p^j$  configurations are included in the CI of both initial and final states of the system). In this extended-averaged level scheme, the orbital wave functions are obtained by minimizing the statistical-weight-averaged energy of all the levels in the MCDF expansion. Since the initial and final states are treated separately, relaxation effects are included in this method as well as the MCBP method. The transition energies and eigenvectors also include contributions from the generalized Breit interaction and quantum electrodynamic corrections. For the lighter elements of astrophysical importance,  $Z \leq 30$ , we have found that these two approaches are usually in quite good agreement for fluorescence yield calculations [12, 40, 41] and dielectronic recombination of numerous ions (see, for example, Refs. [67, 68, 69]).

We have found that our MCBP results and the new MCDF results exhibit the same qualitative behavior (see Fig. 3.4 and Fig. 3.5). Furthermore, at higher  $Z$ , the MCBP and MCDF results for  $A_r$  and  $A_a$  differ by not more than about 5%. Since relativistic effects become increasingly important as  $Z$  is increased, this suggests strongly that the inclusion of relativistic effects perturbatively in the MCBP approach works well for  $Z \leq 30$ . However, larger differences at lower  $Z$  are found. We attribute this discrepancy to differences in the specifics of the wave functions employed.

A useful measure of the quality of multi-configuration calculations of radiative rates can be obtained by performing the calculations in both "length" and "velocity" gauges [70] (see Sec. 2.1.3) which *must* be equal for exact wave functions. Usually, the closer they are,

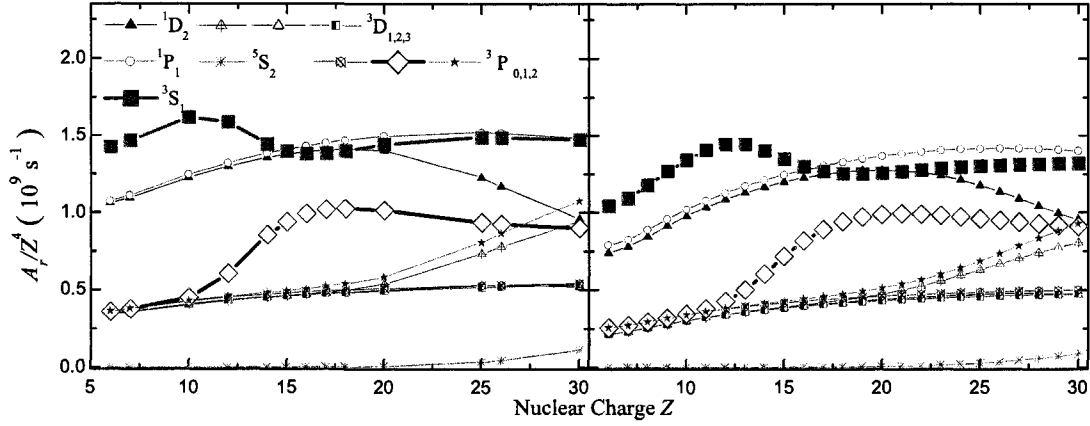


**Figure 3.4** Calculated MCDF (left) and MCBP (right) radiative rates  $A_r$  for the ten K-shell vacancy levels  $1s2s^2 2p^3 (2S+1 L_J)$  of the C-like isoelectronic sequence. Note that  $A_r$  is scaled by  $1/Z^4$  to factor out the strong  $Z^4$  dependence.

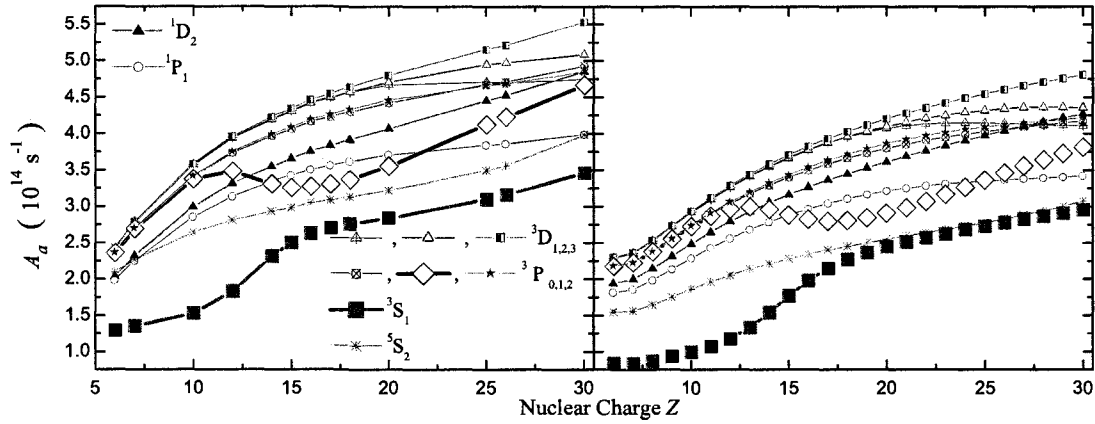


**Figure 3.5** Calculated MCDF (left) and MCBP (right) Auger rates  $A_a$  for the ten K-shell vacancy levels  $1s2s^2 2p^3 (2S+1 L_J)$  of the C-like isoelectronic sequence.

the more accurate the calculation. This has been done for both the MCBP and MCDF results, and comparison between the two is performed (see Table 3.2) for five selected values of  $Z$  from 7 to 30. For  $Z = 7$ , it is found that the MCBP rates differ by up to about 10%, while the MCDF values show up to about 70% discrepancies. At the higher values of  $Z$ , the comparison improves in both calculations; the length-velocity agreement for the MCBP rates is within about 5%, and for the MCDF rates, it is seen to be better than 10%. Unfor-

tunately, while this length-velocity agreement is a good indicator for calculations based on the Schrödinger equation, such as our MCBP method, it is less useful for calculations based

**Table 3.2** Comparison of radiative rates ( $s^{-1}$ ) in length and velocity gauge results of MCBP and MCDF calculations for ten levels of the  $1s2s^22p^3$  C-like ions with selected nuclear charge,  $Z$ .

$Z$	Level	MCBP <sup>L</sup>	MCBP <sup>V</sup>	MCDF <sup>L</sup>	MCDF <sup>V</sup>	$Z$	Level	MCBP <sup>L</sup>	MCBP <sup>V</sup>	MCDF <sup>L</sup>	MCDF <sup>V</sup>
7	<sup>5</sup> S <sub>2</sub>	$8.54 \times 10^6$	$8.21 \times 10^6$	$3.98 \times 10^7$	$5.08 \times 10^7$	12	<sup>5</sup> S <sub>2</sub>	$3.75 \times 10^9$	$3.68 \times 10^9$	$5.99 \times 10^9$	$5.26 \times 10^9$
	<sup>3</sup> D <sub>1</sub>	$5.62 \times 10^{11}$	$5.87 \times 10^{11}$	$8.61 \times 10^{11}$	$5.05 \times 10^{11}$		<sup>3</sup> D <sub>1</sub>	$7.12 \times 10^{12}$	$7.32 \times 10^{12}$	$8.92 \times 10^{12}$	$7.25 \times 10^{12}$
	<sup>3</sup> D <sub>2</sub>	$5.62 \times 10^{11}$	$5.87 \times 10^{11}$	$8.64 \times 10^{11}$	$5.09 \times 10^{11}$		<sup>3</sup> D <sub>2</sub>	$7.10 \times 10^{12}$	$7.31 \times 10^{12}$	$8.93 \times 10^{12}$	$7.27 \times 10^{12}$
	<sup>3</sup> D <sub>3</sub>	$5.62 \times 10^{11}$	$5.87 \times 10^{11}$	$8.68 \times 10^{11}$	$5.13 \times 10^{11}$		<sup>3</sup> D <sub>3</sub>	$7.09 \times 10^{12}$	$7.31 \times 10^{12}$	$8.96 \times 10^{12}$	$7.30 \times 10^{12}$
	<sup>3</sup> S <sub>1</sub>	$2.63 \times 10^{12}$	$2.36 \times 10^{12}$	$3.52 \times 10^{12}$	$2.04 \times 10^{12}$		<sup>3</sup> S <sub>1</sub>	$2.99 \times 10^{13}$	$2.83 \times 10^{13}$	$3.30 \times 10^{13}$	$2.66 \times 10^{13}$
	<sup>3</sup> P <sub>0</sub>	$6.53 \times 10^{11}$	$6.06 \times 10^{11}$	$9.04 \times 10^{11}$	$5.28 \times 10^{11}$		<sup>3</sup> P <sub>0</sub>	$7.83 \times 10^{12}$	$7.53 \times 10^{12}$	$9.38 \times 10^{12}$	$7.50 \times 10^{12}$
	<sup>3</sup> P <sub>1</sub>	$6.54 \times 10^{11}$	$6.06 \times 10^{11}$	$9.06 \times 10^{11}$	$5.31 \times 10^{11}$		<sup>3</sup> P <sub>1</sub>	$8.88 \times 10^{12}$	$8.51 \times 10^{12}$	$1.26 \times 10^{13}$	$1.01 \times 10^{13}$
	<sup>3</sup> P <sub>2</sub>	$6.53 \times 10^{11}$	$6.06 \times 10^{11}$	$9.08 \times 10^{11}$	$5.33 \times 10^{11}$		<sup>3</sup> P <sub>2</sub>	$7.87 \times 10^{12}$	$7.57 \times 10^{12}$	$9.47 \times 10^{12}$	$7.59 \times 10^{12}$
	<sup>1</sup> D <sub>2</sub>	$1.88 \times 10^{12}$	$1.77 \times 10^{12}$	$2.63 \times 10^{12}$	$1.53 \times 10^{12}$		<sup>1</sup> D <sub>2</sub>	$2.25 \times 10^{13}$	$2.19 \times 10^{13}$	$2.70 \times 10^{13}$	$2.18 \times 10^{13}$
	<sup>1</sup> P <sub>1</sub>	$1.99 \times 10^{12}$	$1.79 \times 10^{12}$	$2.66 \times 10^{12}$	$1.55 \times 10^{12}$		<sup>1</sup> P <sub>1</sub>	$2.34 \times 10^{13}$	$2.22 \times 10^{13}$	$2.74 \times 10^{13}$	$2.21 \times 10^{13}$
16	<sup>5</sup> S <sub>2</sub>	$8.86 \times 10^{10}$	$8.81 \times 10^{10}$	$1.20 \times 10^{11}$	$1.06 \times 10^{11}$	20	<sup>5</sup> S <sub>2</sub>	$9.89 \times 10^{11}$	$9.96 \times 10^{11}$	$1.27 \times 10^{12}$	$1.15 \times 10^{12}$
	<sup>3</sup> D <sub>1</sub>	$2.65 \times 10^{13}$	$2.72 \times 10^{13}$	$3.11 \times 10^{13}$	$2.70 \times 10^{13}$		<sup>3</sup> D <sub>1</sub>	$7.61 \times 10^{13}$	$7.79 \times 10^{13}$	$8.67 \times 10^{13}$	$7.82 \times 10^{13}$
	<sup>3</sup> D <sub>2</sub>	$2.62 \times 10^{13}$	$2.69 \times 10^{13}$	$3.08 \times 10^{13}$	$2.69 \times 10^{13}$		<sup>3</sup> D <sub>2</sub>	$7.04 \times 10^{13}$	$7.23 \times 10^{13}$	$8.01 \times 10^{13}$	$7.25 \times 10^{13}$
	<sup>3</sup> D <sub>3</sub>	$2.60 \times 10^{13}$	$2.68 \times 10^{13}$	$3.08 \times 10^{13}$	$2.70 \times 10^{13}$		<sup>3</sup> D <sub>3</sub>	$6.91 \times 10^{13}$	$7.15 \times 10^{13}$	$7.93 \times 10^{13}$	$7.20 \times 10^{13}$
	<sup>3</sup> S <sub>1</sub>	$8.52 \times 10^{13}$	$8.25 \times 10^{13}$	$9.05 \times 10^{13}$	$7.86 \times 10^{13}$		<sup>3</sup> S <sub>1</sub>	$2.01 \times 10^{14}$	$1.99 \times 10^{14}$	$2.31 \times 10^{14}$	$2.08 \times 10^{14}$
	<sup>3</sup> P <sub>0</sub>	$2.82 \times 10^{13}$	$2.75 \times 10^{13}$	$3.21 \times 10^{13}$	$2.76 \times 10^{13}$		<sup>3</sup> P <sub>0</sub>	$7.40 \times 10^{13}$	$7.33 \times 10^{13}$	$8.21 \times 10^{13}$	$7.33 \times 10^{13}$
	<sup>3</sup> P <sub>1</sub>	$5.36 \times 10^{13}$	$5.21 \times 10^{13}$	$6.51 \times 10^{13}$	$5.64 \times 10^{13}$		<sup>3</sup> P <sub>1</sub>	$1.58 \times 10^{14}$	$1.56 \times 10^{14}$	$1.63 \times 10^{14}$	$1.46 \times 10^{14}$
	<sup>3</sup> P <sub>2</sub>	$2.90 \times 10^{13}$	$2.84 \times 10^{13}$	$3.33 \times 10^{13}$	$2.87 \times 10^{13}$		<sup>3</sup> P <sub>2</sub>	$8.23 \times 10^{13}$	$8.22 \times 10^{13}$	$9.36 \times 10^{13}$	$8.40 \times 10^{13}$
	<sup>1</sup> D <sub>2</sub>	$8.05 \times 10^{13}$	$7.94 \times 10^{13}$	$9.14 \times 10^{13}$	$7.96 \times 10^{13}$		<sup>1</sup> D <sub>2</sub>	$2.05 \times 10^{14}$	$2.04 \times 10^{14}$	$2.25 \times 10^{14}$	$2.03 \times 10^{14}$
	<sup>1</sup> P <sub>1</sub>	$8.38 \times 10^{13}$	$8.12 \times 10^{13}$	$9.38 \times 10^{13}$	$8.14 \times 10^{13}$		<sup>1</sup> P <sub>1</sub>	$2.19 \times 10^{14}$	$2.16 \times 10^{14}$	$2.40 \times 10^{14}$	$2.16 \times 10^{14}$
25	<sup>5</sup> S <sub>2</sub>	$1.09 \times 10^{13}$	$1.11 \times 10^{13}$	$1.38 \times 10^{13}$	$1.27 \times 10^{13}$	30	<sup>5</sup> S <sub>2</sub>	$7.24 \times 10^{13}$	$7.57 \times 10^{13}$	$9.26 \times 10^{13}$	$8.70 \times 10^{13}$
	<sup>3</sup> D <sub>1</sub>	$2.48 \times 10^{14}$	$2.54 \times 10^{14}$	$2.87 \times 10^{14}$	$2.66 \times 10^{14}$		<sup>3</sup> D <sub>1</sub>	$6.55 \times 10^{14}$	$6.80 \times 10^{14}$	$7.68 \times 10^{14}$	$7.23 \times 10^{14}$
	<sup>3</sup> D <sub>2</sub>	$1.85 \times 10^{14}$	$1.92 \times 10^{14}$	$2.07 \times 10^{14}$	$1.92 \times 10^{14}$		<sup>3</sup> D <sub>2</sub>	$3.82 \times 10^{14}$	$4.02 \times 10^{14}$	$4.22 \times 10^{14}$	$3.98 \times 10^{14}$
	<sup>3</sup> D <sub>3</sub>	$1.79 \times 10^{14}$	$1.88 \times 10^{14}$	$2.02 \times 10^{14}$	$1.88 \times 10^{14}$		<sup>3</sup> D <sub>3</sub>	$3.85 \times 10^{14}$	$4.09 \times 10^{14}$	$4.32 \times 10^{14}$	$4.08 \times 10^{14}$
	<sup>3</sup> S <sub>1</sub>	$5.09 \times 10^{14}$	$5.12 \times 10^{14}$	$5.82 \times 10^{14}$	$5.39 \times 10^{14}$		<sup>3</sup> S <sub>1</sub>	$1.07 \times 10^{15}$	$1.10 \times 10^{15}$	$1.19 \times 10^{15}$	$1.13 \times 10^{15}$
	<sup>3</sup> P <sub>0</sub>	$1.90 \times 10^{14}$	$1.92 \times 10^{14}$	$2.07 \times 10^{14}$	$1.90 \times 10^{14}$		<sup>3</sup> P <sub>0</sub>	$4.06 \times 10^{14}$	$4.17 \times 10^{14}$	$4.39 \times 10^{14}$	$4.10 \times 10^{14}$
	<sup>3</sup> P <sub>1</sub>	$3.76 \times 10^{14}$	$3.78 \times 10^{14}$	$3.66 \times 10^{14}$	$3.38 \times 10^{14}$		<sup>3</sup> P <sub>1</sub>	$7.37 \times 10^{14}$	$7.58 \times 10^{14}$	$7.29 \times 10^{14}$	$6.85 \times 10^{14}$
	<sup>3</sup> P <sub>2</sub>	$2.69 \times 10^{14}$	$2.74 \times 10^{14}$	$3.16 \times 10^{14}$	$2.92 \times 10^{14}$		<sup>3</sup> P <sub>2</sub>	$7.52 \times 10^{14}$	$7.81 \times 10^{14}$	$8.72 \times 10^{14}$	$8.22 \times 10^{14}$
	<sup>1</sup> D <sub>2</sub>	$4.60 \times 10^{14}$	$4.68 \times 10^{14}$	$4.80 \times 10^{14}$	$4.45 \times 10^{14}$		<sup>1</sup> D <sub>2</sub>	$7.73 \times 10^{14}$	$8.00 \times 10^{14}$	$7.76 \times 10^{14}$	$7.30 \times 10^{14}$
	<sup>1</sup> P <sub>1</sub>	$5.54 \times 10^{14}$	$5.57 \times 10^{14}$	$5.95 \times 10^{14}$	$5.50 \times 10^{14}$		<sup>1</sup> P <sub>1</sub>	$1.14 \times 10^{15}$	$1.17 \times 10^{15}$	$1.20 \times 10^{15}$	$1.13 \times 10^{15}$

on the Dirac equation, such as the MCDF method, where it is known that the velocity form is generally to be preferred [71] and that length-form convergence is slow. As corroboration of these ideas, note that in almost every case shown in Table 3.2, the MCDF-velocity result

is in much better agreement with the MCBP results than the MCDF-length rates. In any case, based upon the comparison of length and velocity gauges, it appears that the MCBP results are reasonably accurate.

To understand the physics behind this anomalous behavior - the non-smooth behavior of the  ${}^3S_1$  and  ${}^3P_1$  radiative and Auger rates- we note first that the two states exhibiting anomalous behavior are both  $J = 1$  states. Since they have the same  $J = 1$  values for total momentum, these states can interact via the spin-orbit interaction. But, the spin-orbit coupling matrix element increases rapidly with increasing  $Z$  (see Appendix B). This suggests that any effect arising from spin-orbit coupling between the states should be largest at the highest  $Z$ , which is *not* what is seen. However, from a perturbation theory point of view, the full mixing coefficient is related to the overlap matrix element divided by the energy difference of two unmixed states,  $\left| \frac{c_1}{c_2} \right| \approx \left| \frac{V_{SO}}{E_2 - E_1} \right|$ , thus suggesting that the anomalous behavior is due to abnormally-strong spin-orbit mixing due to an energy crossing, as a function of  $Z$ , of the LS-energies of the two levels, similar to the well-known Von Neumann-Wigner [38, 72] avoided crossings phenomena. In fact, there is an energy crossing between the  $1s2s^22p^3({}^3P)$  and  $1s2s^22p^3({}^3S)$  LS-states. It is very interesting that the energy crossing doesn't appear in the single-configuration (SC) calculations. The energy of the SC  $1s2s^22p^3({}^3S)$  term lies below the energy of the SC  $1s2s^22p^3({}^3P)$  term along the sequence. We should note that after the inclusion of CI effects, the energy of the  ${}^3S$  CI state stays about same as the  ${}^3S$  SC energy whereas the  ${}^3P$  CI energy gets lower and causes the crossing (see Fig. 3.6a).

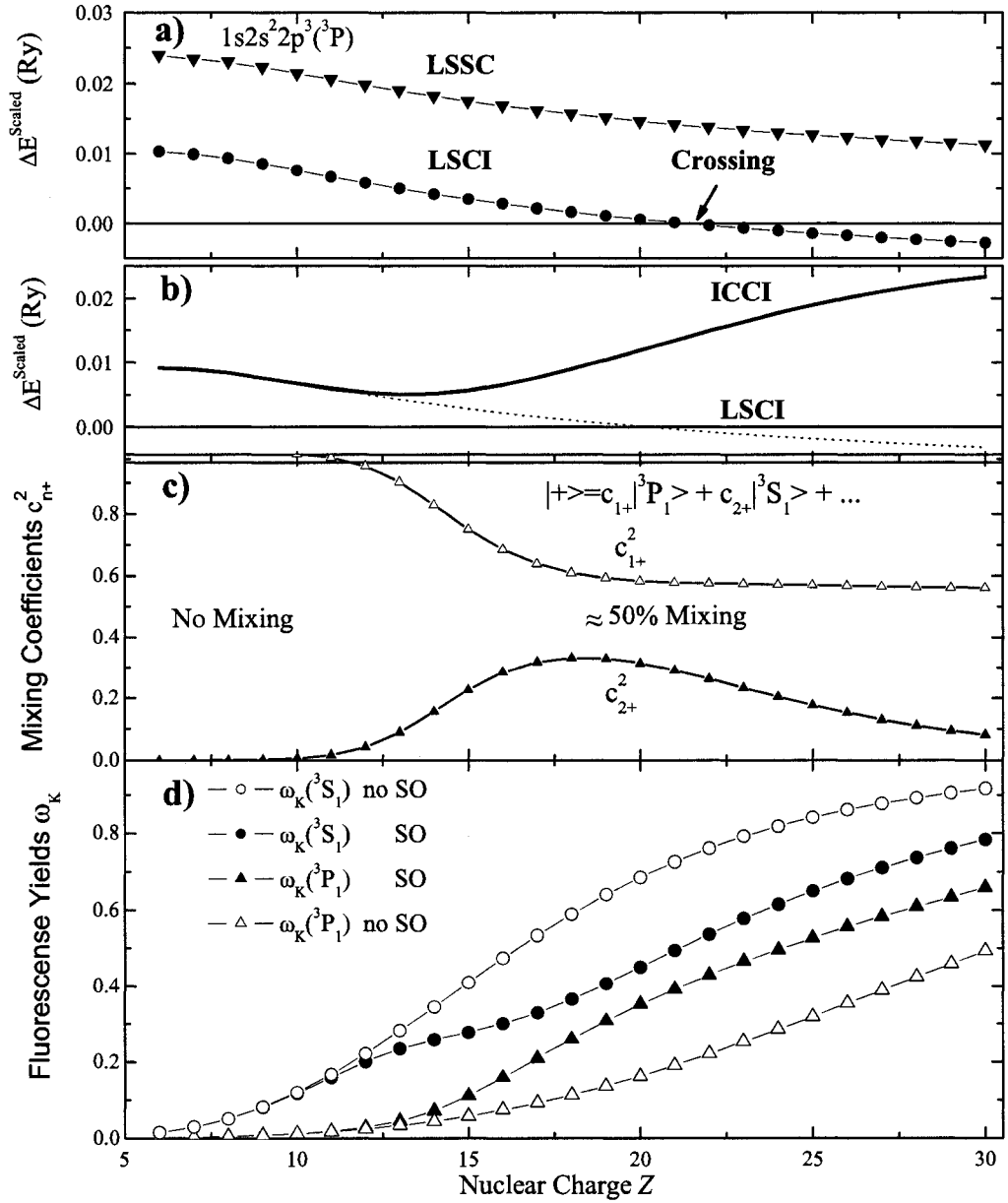


**Figure 3.6** The anomalous behavior of the fluorescence yields for  $^3S_1$  and  $^3P_1$  levels. **a)**  $(E(^3P) - E(^3S))/Z$  within the  $1s2s^2 2p^3$  configuration at the nonrelativistic single configuration (LSSC) and configuration interaction (LSCI) levels. **b)** Same as a) with nonrelativistic LSCI (dashed line) and full calculation including CI and relativistic effects in an intermediate coupling scheme (ICCI, solid curve). **c)** Mixing coefficients for the relativistically (spin-orbit) mixed  $^3P_1$  and  $^3S_1$  states of the  $1s2s^2 2p^3$  configuration. **d)** Fluorescence yields excluding and including spin-orbit effects for the  $1s2s^2 2p^3(^3P_1)$  and  $1s2s^2 2p^3(^3S_1)$  states. The anomalous fluorescence yield behavior is seen to occur once there is appreciable spin-orbit mixing  $c_{2+}^2 \lesssim c_{1+}^2$ .

To explain the occurrence of this energy crossing quantitatively, it is sufficient to concentrate on the interaction of the  $1s2s^22p^3(^3P)$  SC state and the two-electron,  $2s^2 \rightarrow 2p^2$ , intra-shell promotion. In a SC description, we denote the two states as  $|^3P_-\rangle \leftrightarrow 1s2s^22p^3(^3P)$  and  $|^3P_+\rangle \leftrightarrow 1s2p^5(^3P)$  that interact through the electron-electron repulsion term in the Hamiltonian. In this CI-mixed representation, we get

$$|^3P_{\pm}\rangle^{CI} = a_{\pm}|^3P_{\pm}\rangle + b_{\pm}|^3P_{\pm}\rangle.$$

Our calculated results show that the mixing coefficients are approximately constant along the isoelectronic sequence, that is  $a \leftrightarrow a_{\pm} \approx 0.99$  and  $b \leftrightarrow \pm b_{\pm} \approx 0.1$ . The energies of these mixed states will be

$$E(^3P_{\pm}^{CI}) = a^2 E(^3P_{\pm}) \pm 2ab \langle ^3P_- | \sum_{i<j} \frac{1}{r_{ij}} | ^3P_+ \rangle + b^2 E(^3P_{\pm}).$$

Considering the hydrogenic energy scaling  $(E_+ - E_-) \sim Z$ , a perturbative approximation gives  $c_b/c_a = \langle ^3P_- | \sum_{i<j} \frac{1}{r_{ij}} | ^3P_+ \rangle / |(E_+ - E_-)| \approx 0.1$ , independent of  $Z$ . And since the non-diagonal matrix element scales as  $Z$ , our calculated results have verified the linear  $Z$  dependence of this matrix element. Because the second term dominates the third term, if we  $Z$ -scale the change in the energies then we should get a constant energy shifting along an isoelectronic sequence. This behavior is shown in our computed results (see Fig. 3.6a).

Furthermore, with the inclusion of relativistic effects, there is a non-zero matrix element between the  $^3P_1$  and  $^3S_1$  states, principally through the spin-orbit interaction. This, of course, leads to an avoided crossing, as shown in Fig. 3.6b; note the striking similarity with Fig. 10-2 of Ref. [2]. Considering two spin-orbit-mixed states interacting through the (relatively weak) spin-orbit interaction,  $|\pm\rangle = c_{1\pm}|^3S_1\rangle + c_{2\pm}|^3P_1\rangle$ , we obtain the (non-

perturbative) determinantal equation for the eigenvalues  $E_{\pm}$  and eigenvalues  $c_{i\pm}$ :

$$\begin{pmatrix} E(^3S_1) - E_{\pm} & V_{SO} \\ V_{SO} & E(^3P_1) - E_{\pm} \end{pmatrix} \begin{pmatrix} c_{1\pm} \\ c_{2\pm} \end{pmatrix} = \begin{pmatrix} 0 \\ 0 \end{pmatrix}.$$

For closely degenerate, unperturbed states, the eigenvalues of the mixed states, assuming  $\delta = E(^3P_1) - E(^3S_1) \approx 0$ , and with  $\epsilon = \frac{E(^3P_1) + E(^3S_1)}{2}$ , are given by  $E_{\pm} = \epsilon \pm V_{SO}/2$ . For this perturbed energy, our determinantal equation yields approximate 50-50 mixing between the closely degenerate states, that is,  $c_{i\pm}^2 \approx 1/2$ .

Our computed mixing coefficients are shown in Fig. 3.6c, where it is evident that there is essentially no mixing of these two states at low- $Z$  and nearly 50-50 mixing around  $Z = 20$ , the well-known result for near-degeneracy. In this region, the maximum mixing of  $^3S_1$  and  $^3P_1$  signatures in each state occurs and, therefore, a “sharing” of radiative and Auger rates and a strong deviation from the otherwise-smooth behavior results (the sum remains smooth by unitarity, as can also be inferred from Fig. 3.4 and Fig. 3.5).

Finally, we have recalculated the fluorescence yields by excluding spin-orbit interactions and obtained well-behaved curves for the  $^3S_1$  and  $^3P_1$  levels (see Fig. 3.6d). It is found that the anomalous behavior in the fluorescence yields occurs when there is an appreciable mixing due to spin-orbit effects.

### 3.1.4 Comprehensive 2<sup>nd</sup>-Row Isoelectronic-Sequence Calculations

As a completion of the present fluorescence yield investigation, we have calculated level energies and level to level radiative and Auger decay rates for the K-shell-excited states of all Li-like through F-like 2<sup>nd</sup>-row isoelectronic sequences (equivalently, K-shell-

photoionized states of all Be-like through Ne-like ions). This amounts to a total number of ions in terms of the number of electrons in the ion,  $N_e$ , and the nuclear charge,  $Z$ , that is

$$N_{ion} \approx \sum_{N_e=3}^9 \sum_{Z=N_e+1}^{30} 1 = 168 . \quad (3.9)$$

Furthermore, for each series of these ionic K-shell vacancies there exists multiple radiative and/or Auger decay processes, leading to an “*astronomical*” number of energies and transition rates. These complete 2<sup>nd</sup>-row computed energies and transition rates have been systematically evaluated [73] and comprehensively tabulated [74] for future publications.

As a simple example, we tabulate the total radiative and total Auger rate results along with the comparison with earlier theoretical calculations [63], for the  $^3P_2$ ,  $^3P_1$ ,  $^3P_0$ , and  $^1P_1$  K-shell vacancy states of the  $1s2s^22p^5$  oxygen-like isoelectronic sequence in Table 3.3. From these rates, one can compute the fluorescence yields,  $\omega_K$ , for any states using Eq. 1.1.

**Table 3.3** The total K-shell radiative and Auger rates for the  $1s2s^22p^5$  O-like isoelectronic sequence.

$Z$	Radiative Rates $A_r$ ( $s^{-1}$ )				Auger Rates $A_a$ ( $s^{-1}$ )			
	$^3P_2$	$^3P_1$	$^3P_0$	$^1P_1$	$^3P_2$	$^3P_1$	$^3P_0$	$^1P_1$
9 <sup>a</sup>	$3.7492 \times 10^{12}$	$3.7507 \times 10^{12}$	$3.7510 \times 10^{12}$	$7.9773 \times 10^{12}$	$4.4362 \times 10^{14}$	$4.4340 \times 10^{14}$	$4.4242 \times 10^{14}$	$4.0343 \times 10^{14}$
10 <sup>a</sup>	$5.8765 \times 10^{12}$	$5.8800 \times 10^{12}$	$5.8799 \times 10^{12}$	$1.2413 \times 10^{13}$	$4.5757 \times 10^{14}$	$4.5729 \times 10^{14}$	$4.5604 \times 10^{14}$	$4.1680 \times 10^{14}$
10 <sup>b</sup>	$5.50 \times 10^{12}$	$5.50 \times 10^{12}$	$5.50 \times 10^{12}$	$1.16 \times 10^{13}$	$3.65 \times 10^{14}$	$3.65 \times 10^{14}$	$3.65 \times 10^{14}$	$3.38 \times 10^{14}$
11 <sup>a</sup>	$8.9643 \times 10^{12}$	$8.9722 \times 10^{12}$	$8.9705 \times 10^{12}$	$1.8825 \times 10^{13}$	$4.7889 \times 10^{14}$	$4.7854 \times 10^{14}$	$4.7694 \times 10^{14}$	$4.3696 \times 10^{14}$
12 <sup>a</sup>	$1.3259 \times 10^{13}$	$1.3277 \times 10^{13}$	$1.3270 \times 10^{13}$	$2.7710 \times 10^{13}$	$5.0357 \times 10^{14}$	$5.0313 \times 10^{14}$	$5.0114 \times 10^{14}$	$4.6013 \times 10^{14}$
12 <sup>b</sup>	$1.31 \times 10^{13}$	$1.31 \times 10^{13}$	$1.31 \times 10^{13}$	$2.72 \times 10^{13}$	$4.59 \times 10^{14}$	$4.59 \times 10^{14}$	$4.59 \times 10^{14}$	$4.26 \times 10^{14}$
13 <sup>a</sup>	$1.9036 \times 10^{13}$	$1.9075 \times 10^{13}$	$1.9055 \times 10^{13}$	$3.9621 \times 10^{13}$	$5.2913 \times 10^{14}$	$5.2857 \times 10^{14}$	$5.2612 \times 10^{14}$	$4.8406 \times 10^{14}$
14 <sup>a</sup>	$2.6601 \times 10^{13}$	$2.6683 \times 10^{13}$	$2.6631 \times 10^{13}$	$5.5163 \times 10^{13}$	$5.5432 \times 10^{14}$	$5.5361 \times 10^{14}$	$5.5066 \times 10^{14}$	$5.0765 \times 10^{14}$
14 <sup>b</sup>	$2.71 \times 10^{13}$	$2.72 \times 10^{13}$	$2.72 \times 10^{13}$	$5.60 \times 10^{13}$	$5.34 \times 10^{14}$	$5.34 \times 10^{14}$	$5.34 \times 10^{14}$	$4.96 \times 10^{14}$
15 <sup>a</sup>	$3.6283 \times 10^{13}$	$3.6450 \times 10^{13}$	$3.6331 \times 10^{13}$	$7.4990 \times 10^{13}$	$5.7855 \times 10^{14}$	$5.7766 \times 10^{14}$	$5.7416 \times 10^{14}$	$5.3037 \times 10^{14}$
16 <sup>a</sup>	$4.8443 \times 10^{13}$	$4.8772 \times 10^{13}$	$4.8516 \times 10^{13}$	$9.9793 \times 10^{13}$	$6.0155 \times 10^{14}$	$6.0043 \times 10^{14}$	$5.9636 \times 10^{14}$	$5.5200 \times 10^{14}$
16 <sup>b</sup>	$5.03 \times 10^{13}$	$5.07 \times 10^{13}$	$5.03 \times 10^{13}$	$1.03 \times 10^{14}$	$5.97 \times 10^{14}$	$5.96 \times 10^{14}$	$5.97 \times 10^{14}$	$5.54 \times 10^{14}$
17 <sup>a</sup>	$6.3466 \times 10^{13}$	$6.4090 \times 10^{13}$	$6.3574 \times 10^{13}$	$1.3029 \times 10^{14}$	$6.2325 \times 10^{14}$	$6.2182 \times 10^{14}$	$6.1718 \times 10^{14}$	$5.7247 \times 10^{14}$
18 <sup>a</sup>	$8.1761 \times 10^{13}$	$8.2909 \times 10^{13}$	$8.1918 \times 10^{13}$	$1.6723 \times 10^{14}$	$6.4364 \times 10^{14}$	$6.4183 \times 10^{14}$	$6.3661 \times 10^{14}$	$5.9180 \times 10^{14}$
18 <sup>b</sup>	$8.63 \times 10^{13}$	$8.78 \times 10^{13}$	$8.64 \times 10^{13}$	$1.75 \times 10^{14}$	$6.46 \times 10^{14}$	$6.46 \times 10^{14}$	$6.46 \times 10^{14}$	$6.01 \times 10^{14}$
19 <sup>a</sup>	$1.0376 \times 10^{14}$	$1.0581 \times 10^{14}$	$1.0399 \times 10^{14}$	$2.1133 \times 10^{14}$	$6.6278 \times 10^{14}$	$6.6047 \times 10^{14}$	$6.5472 \times 10^{14}$	$6.1009 \times 10^{14}$
20 <sup>a</sup>	$1.2994 \times 10^{14}$	$1.3349 \times 10^{14}$	$1.3025 \times 10^{14}$	$2.6332 \times 10^{14}$	$6.8075 \times 10^{14}$	$6.7780 \times 10^{14}$	$6.7158 \times 10^{14}$	$6.2741 \times 10^{14}$
20 <sup>b</sup>	$1.38 \times 10^{14}$	$1.43 \times 10^{14}$	$1.38 \times 10^{14}$	$2.77 \times 10^{14}$	$6.87 \times 10^{14}$	$6.86 \times 10^{14}$	$6.87 \times 10^{14}$	$6.40 \times 10^{14}$
21 <sup>a</sup>	$1.6076 \times 10^{14}$	$1.6674 \times 10^{14}$	$1.6119 \times 10^{14}$	$3.2384 \times 10^{14}$	$6.9762 \times 10^{14}$	$6.9388 \times 10^{14}$	$6.8727 \times 10^{14}$	$6.4389 \times 10^{14}$
22 <sup>a</sup>	$1.9675 \times 10^{14}$	$2.0652 \times 10^{14}$	$1.9732 \times 10^{14}$	$3.9348 \times 10^{14}$	$7.1349 \times 10^{14}$	$7.0876 \times 10^{14}$	$7.0189 \times 10^{14}$	$6.5962 \times 10^{14}$
23 <sup>a</sup>	$2.3842 \times 10^{14}$	$2.5397 \times 10^{14}$	$2.3918 \times 10^{14}$	$4.7271 \times 10^{14}$	$7.2845 \times 10^{14}$	$7.2251 \times 10^{14}$	$7.1552 \times 10^{14}$	$6.7473 \times 10^{14}$
24 <sup>a</sup>	$2.8633 \times 10^{14}$	$3.1039 \times 10^{14}$	$2.8733 \times 10^{14}$	$5.6188 \times 10^{14}$	$7.4257 \times 10^{14}$	$7.3519 \times 10^{14}$	$7.2824 \times 10^{14}$	$6.8930 \times 10^{14}$
25 <sup>a</sup>	$3.4105 \times 10^{14}$	$3.7727 \times 10^{14}$	$3.4235 \times 10^{14}$	$6.6126 \times 10^{14}$	$7.5592 \times 10^{14}$	$7.4686 \times 10^{14}$	$7.4013 \times 10^{14}$	$7.0340 \times 10^{14}$
26 <sup>a</sup>	$4.0318 \times 10^{14}$	$4.5619 \times 10^{14}$	$4.0484 \times 10^{14}$	$7.7104 \times 10^{14}$	$7.6858 \times 10^{14}$	$7.5760 \times 10^{14}$	$7.5125 \times 10^{14}$	$7.1711 \times 10^{14}$
26 <sup>c</sup>	$4.03 \times 10^{14}$	$4.61 \times 10^{14}$	$4.04 \times 10^{14}$	$7.61 \times 10^{14}$	$7.45 \times 10^{14}$	$7.32 \times 10^{14}$	$7.25 \times 10^{14}$	$6.99 \times 10^{14}$
27 <sup>a</sup>	$4.7332 \times 10^{14}$	$5.4882 \times 10^{14}$	$4.7543 \times 10^{14}$	$8.9143 \times 10^{14}$	$7.8061 \times 10^{14}$	$7.6751 \times 10^{14}$	$7.6167 \times 10^{14}$	$7.3045 \times 10^{14}$
28 <sup>a</sup>	$5.5210 \times 10^{14}$	$6.5680 \times 10^{14}$	$5.5475 \times 10^{14}$	$1.0227 \times 10^{15}$	$7.9207 \times 10^{14}$	$7.7668 \times 10^{14}$	$7.7145 \times 10^{14}$	$7.4343 \times 10^{14}$
29 <sup>a</sup>	$6.4017 \times 10^{14}$	$7.8170 \times 10^{14}$	$6.4347 \times 10^{14}$	$1.1652 \times 10^{15}$	$8.0300 \times 10^{14}$	$7.8521 \times 10^{14}$	$7.8064 \times 10^{14}$	$7.5605 \times 10^{14}$
30 <sup>a</sup>	$7.3820 \times 10^{14}$	$9.2496 \times 10^{14}$	$7.4227 \times 10^{14}$	$1.3195 \times 10^{15}$	$8.1346 \times 10^{14}$	$7.9321 \times 10^{14}$	$7.8929 \times 10^{14}$	$7.6831 \times 10^{14}$

<sup>a</sup> Present MCBP results.

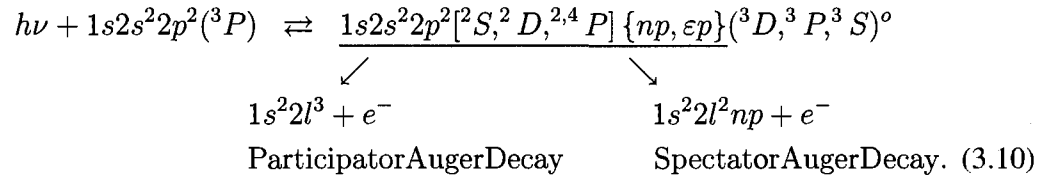
<sup>b</sup> Recent MCBP results [75].

<sup>c</sup> Earlier MCBP results [63].

## 3.2 Carbon K-Shell Photoabsorption Cross Section Results

### 3.2.1 C: Abundant in the Interstellar Medium

For photoabsorption of neutral carbon, the particular atomic processes of interest are the following:



Note that there are two fundamentally different Auger decay pathways. First, there is participator Auger decay, which involves the outer, valance  $np$  electron and therefore scales as  $n^{-3}$ . This is routinely incorporated into the standard R-matrix implementation by including the appropriate  $1s^22l^3 + e^-$  channels in the close-coupling equations [45]. The second, more problematic pathway is the spectator Auger decay that instead involves core Auger decay and is therefore independent of  $n$ : spectator Auger decay dominates at the Rydberg limit  $n \rightarrow \infty$ . Indeed, spectator Auger decay can dominate by orders of magnitude at even the lowest  $n$  [15, 76].

We use the Hartree-Fock [31] and multi-configuration Hartree-Fock [32] atomic structure program packages to generate radial target  $C^+$  orbitals for our calculations. The optimization procedure (HF or MCHF) that we have used to generate  $C^+$  orbitals is summarized in Table 3.4 for each orbital. Single and double electron promotions are considered to account for orbital relaxation effects due to  $1s$ -vacancy.

The core (spectator) Auger widths are calculated by performing R-matrix calculations

**Table 3.4** Criterion for determination of  $C^+$  physical  $1s$ ,  $2s$ , and  $2p$  orbitals and correlation (or pseudo)  $\overline{3s}$ ,  $\overline{3p}$ , and  $\overline{3d}$  orbitals.

---



---

$1s$ , $2s$ , and $2p$	From a HF (single-configuration) calculation for the $1s^2 2s^2 2p$ ( $^2P$ ) term.
$\overline{3s}$ , $\overline{3p}$ , and $\overline{3d}$	From a MCHF (multi-configuration) calculation for the lowest K-shell vacancy $1s 2s^2 2p^2$ ( $^4P$ ) term including single and double $n = 2 \rightarrow n = 3$ promotions.

---



---

for the electron scattering off the four electron  $C^{2+}$  target states. Auger widths are determined using the Smith time-delay method (see Sec. 2.4.1). These values are used in a Feshbach projection-operator, optical potential methodology, within our R-matrix calculations, to include Auger broadening effects. Cross sections are calculated in length and velocity gauges and agreement between the calculations is within 6.2%, which is a measure of the completeness of our wave functions (see Sec. 2.1.3). These photoabsorption cross section results are compared with those obtained using an independent-particle (IP) approximation [77] in Fig. 3.7. As is clearly seen, our background cross section is in good agreement with the IP results, but we also include the important  $1s \rightarrow np$  absorption features that are necessary for understanding abundances in the ISM, as discussed earlier in Sec. 1.2 (see Fig. 1.3).

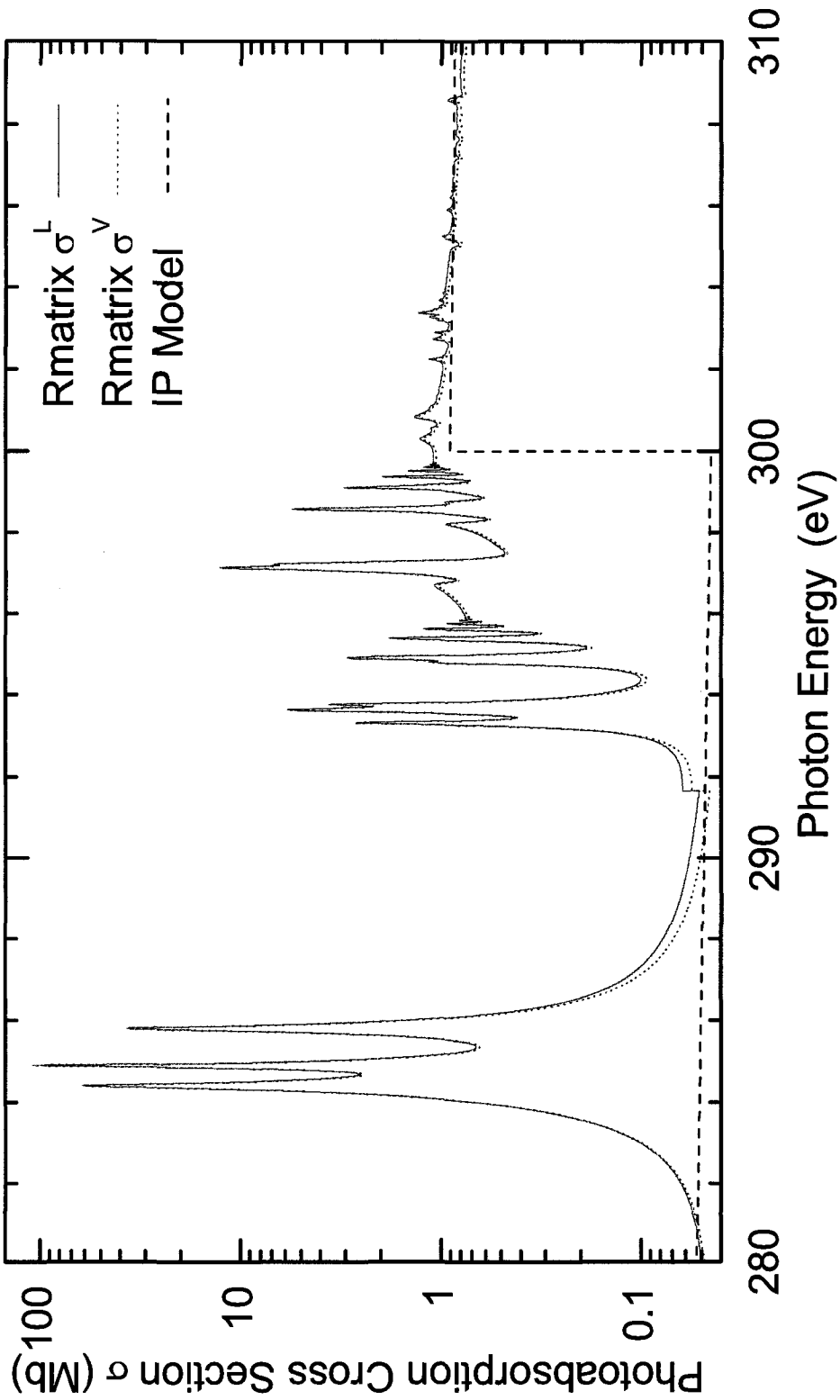


**Figure 3.7** Calculated K-shell photoabsorption cross section of carbon at the K-edge in length and velocity gauges: Logarithmic plot showing the natural-width resonance features and the oft-used, resonance-omitted, IP approximation results [77]. The discontinuity around 291.6 eV in the R-matrix results is due to the turn-off of Auger broadening at low  $n$  (for technical reasons). This discontinuity of  $1.1 \times 10^{-2}$  Mb is very small compared to important resonance features of  $10^1 - 10^2$  Mb.

A comparison of Auger widths of the lowest 17 autoionizing  $C^+$  target states is shown in Table 3.5 between the two theoretical results. Table 3.6 shows our R-matrix results for the ground state energy of C, the first 25-target threshold energies, and the resonantly-excited K-shell vacancy state energies compared to results from fluorescence yield calculations for B-like and neutral C and also to the available NIST critically evaluated data. Also shown in Table 3.6 are the photon energies with respect to the ground state of C. Overall, good agreement between our R-matrix and AUTOSTRUCTURE results is found.

**Table 3.5** Comparison of Auger widths for the 17  $C^+$  autoionizing target states above the K-shell threshold (see Table 3.6).

State	Present <sup>a</sup>	AUTO <sup>b</sup>	MCDF <sup>c</sup>
1 $1s2s^22p^2 (^4P)$	$6.45E-02$	$8.61E-02$	$6.68E-02$
2 $1s2s^22p^2 (^2D)$	$9.14E-02$	$1.16E-01$	$8.62E-02$
3 $1s2s^22p^2 (^2P)$	$4.93E-02$	$5.19E-02$	$4.75E-02$
4 $1s2s^22p^2 (^2S)$	$8.65E-02$	$1.02E-01$	$1.49E-04$
5 $1s2s(^1S)2p^3 (^4S)$	$1.55E-02$	$2.06E-02$	$5.86E-02$
6 $1s2s(^3S)2p^3 (^4D)$	$4.60E-02$	$6.42E-02$	$4.77E-02$
7 $1s2s(^3S)2p^3 (^4P)$	$3.56E-02$	$4.87E-02$	$3.73E-02$
8 $1s2s(^1S)2p^3 (^2D)$	$7.21E-02$	$9.64E-02$	$9.08E-02$
9 $1s2s(^1S)2p^3 (^2P)$	$6.42E-02$	$7.77E-02$	$8.01E-02$
10 $1s2s(^3S)2p^3 (^4S)$	$4.57E-02$	$7.15E-02$	$2.49E-02$
11 $1s2s(^3S)2p^3 (^2D)$	$7.78E-02$	$1.18E-01$	$8.23E-02$
12 $1s2s(^3S)2p^3 (^2S)$	$1.49E-02$	$1.25E-02$	$8.89E-03$
13 $1s2s(^3S)2p^3 (^2P)$	$6.56E-02$	$1.01E-01$	$7.13E-02$
14 $1s2p^4 (^4P)$	$3.89E-03$	$6.83E-02$	$5.18E-02$
15 $1s2p^4 (^2D)$	$7.24E-02$	$1.08E-01$	$8.16E-02$
16 $1s2p^4 (^2P)$	$4.60E-02$	$6.69E-02$	$5.03E-02$
17 $1s2p^4 (^2S)$	$4.90E-02$	$1.36E-01$	$5.56E-02$

<sup>a</sup> Present R-matrix results.

<sup>b</sup> MCBP AUTOSTRUCTURE results.

<sup>c</sup> MCDF results [62].

**Table 3.6** Comparison of energies of the relevant C and C<sup>+</sup> states involved in the present investigation. The term energies are given relative to the  $1s^2 2s^2 2p$  ( $^2P$ ) ground state of C<sup>+</sup>. The photon energies are given relative to the  $1s^2 2s^2 2p^2$  ( $^3P$ ) ground state of C.

State	Term Energy (Ry)			Photon Energies (eV)		
	Present <sup>a</sup>	AUTO <sup>b</sup>	OTHER <sup>c,d</sup>	Present <sup>a</sup>	AUTO <sup>b</sup>	OTHER <sup>c,d</sup>
1 $1s^2 2s^2 2p^2$ ( $^3P$ )	-0.8493	-0.7189	-0.8277 <sup>c</sup>	0.0000	0.0000	0.0000 <sup>c</sup>
2 $1s^2 2s^2 2p$ ( $^2P$ )	0.0000	0.0000	0.0004 <sup>c</sup>	11.5555	9.7810	11.2671 <sup>c</sup>
3 $1s^2 2s 2p^2$ ( $^4P$ )	0.3814	0.3746	0.3922 <sup>c</sup>	16.7449	14.8782	16.5977 <sup>c</sup>
4 $1s^2 2s 2p^2$ ( $^2D$ )	0.7128	0.7574	0.6828 <sup>c</sup>	21.2537	20.0853	20.5522 <sup>c</sup>
5 $1s^2 2s 2p^2$ ( $^3S$ )	0.9850	0.9589	0.8793 <sup>c</sup>	24.9568	22.8279	23.2256 <sup>c</sup>
6 $1s^2 2s 2p^2$ ( $^2P$ )	1.0450	1.1134	1.0083 <sup>c</sup>	25.7738	24.9295	24.9810 <sup>c</sup>
7 $1s^2 2p^3$ ( $^4S$ )	1.3104	1.3095	1.2942 <sup>c</sup>	29.3841	27.5976	28.8710 <sup>c</sup>
8 $1s^2 2p^3$ ( $^2D$ )	1.4311	1.5151	1.3711 <sup>c</sup>	31.0267	30.3957	29.9170 <sup>c</sup>
9 $1s^2 2p^3$ ( $^2P$ )	1.6792	1.7233	1.5377 <sup>c</sup>	34.4025	33.2282	32.1832 <sup>c</sup>
10 $1s 2s^2 2p^3$ ( $^3D$ )	20.0536	20.3330		284.4008	286.4270	
11 $1s 2s^2 2p^3$ ( $^3S$ )	20.0894	20.3528		284.8885	286.6974	
12 $1s 2s^2 2p^3$ ( $^3P$ )	20.1566	20.4082		285.8022	287.4509	
13 $1s 2s^2 2p^2$ ( $^4P$ )	20.9133	20.9723		296.0976	295.1257	296.07 ± 0.2 <sup>d</sup>
14 $1s 2s^2 2p^2$ ( $^2D$ )	21.1651	21.2193		299.5236	298.4867	
15 $1s 2s^2 2p^2$ ( $^2P$ )	21.1899	21.2280		299.8609	298.6048	
16 $1s 2s^2 2p^2$ ( $^2S$ )	21.3351	21.3339		301.8369	300.0456	
17 $1s 2s(^1S) 2p^3$ ( $^4S$ )	21.4753	21.4898		303.7442	302.1662	
18 $1s 2s(^3S) 2p^3$ ( $^4D$ )	21.5097	21.5616		304.2117	303.1433	
19 $1s 2s(^3S) 2p^3$ ( $^4P$ )	21.6968	21.7240		306.7575	305.3528	
20 $1s 2s(^1S) 2p^3$ ( $^2D$ )	21.8446	21.9353		308.7688	308.2281	
21 $1s 2s(^1S) 2p^3$ ( $^2P$ )	22.0355	22.0975		311.3662	310.4357	
22 $1s 2s(^3S) 2p^3$ ( $^4S$ )	22.0847	22.2193		312.0362	312.0922	
23 $1s 2s(^3S) 2p^3$ ( $^2D$ )	22.1103	22.2616		312.3834	312.6681	
24 $1s 2s(^3S) 2p^3$ ( $^2S$ )	22.2898	22.3968		314.8255	314.5076	
25 $1s 2s(^3S) 2p^3$ ( $^2P$ )	22.3180	22.4238		315.2095	314.8745	
26 $1s 2p^4$ ( $^4P$ )	22.4901	22.5995		317.5512	317.2659	
27 $1s 2p^4$ ( $^2D$ )	22.6795	22.8489		320.1276	320.6580	
28 $1s 2p^4$ ( $^2P$ )	22.7300	22.8578		320.8157	320.7795	
29 $1s 2p^4$ ( $^2S$ )	23.0860	23.2212		325.6586	325.7238	

<sup>a</sup> Present R-matrix results.

<sup>b</sup> MCBP AUTOSTRUCTURE results.

<sup>c</sup> NIST data.

<sup>d</sup> Experimental data [78].

### 3.2.2 C<sup>+</sup>: Comparison with Laboratory Experiment

The specific processes of interest for K-shell photoabsorption of ground state C<sup>+</sup> are the following:

$$h\nu + 1s^2 2s^2 2p(^2P^o) \rightarrow 1s 2s^2 2p \{np, \varepsilon p\} (^2D, ^2P, ^2S). \quad (3.11)$$

These K-shell-vacancy excited states can relax via one of the following Auger processes

$$1s 2s^2 2p np \rightarrow 1s^2 2s^i 2p^j \varepsilon \ell \quad (i + j = 2) \text{ participator Auger decay,} \quad (3.12)$$

$$\rightarrow 1s^2 2s^i 2p^j np \varepsilon \ell \quad (i + j = 1) \text{ spectator Auger decay.} \quad (3.13)$$

We have found that K-shell  $1s \rightarrow 2p$  photoexcitation of C<sup>+</sup> has been studied experimentally [79], but no higher  $1s \rightarrow np$  ( $n = 3, \infty$ ) experimental studies have been performed to our knowledge. These measurements were performed using an electron-cyclotron-resonance ion source at the Advanced Light Source (ALS) to produce the photoexcitation cross section for the energy region  $h\nu = 287 - 291$  eV. Theoretical calculations were also carried out by using an R-matrix pseudo-state (RMPS) method [79, 80]. The metastable-ion fraction in the ion beam was found to be  $(20 \pm 5)\%$  by comparing the experimental data with the theoretical cross sections. Thus, we have also studied the photoabsorption of C<sup>+</sup> metastable states.

Metastable states are excited states that cannot decay via normal (electric dipole) radiative interactions and are therefore relatively long-lived. The metastable state of C<sup>+</sup> is  $1s^2 2s 2p^2(^4P^o)$  and, since decay of a quartet state to the doublet ground state is spin-forbidden (see Sec. 2.1.3), the quartet state has a much longer lifetime than the doublet

excited states. Radiative decay of these metastable states occurs only via S.O. mixing. Population of metastable states is possible via thermal excitation of  $C^+$  or by photoionization of the  $2s$  shell of the ground state of C.

In the K-shell ( $1s \rightarrow 2p$ ) photoexcitation processes of  $C^+$ , considering that the  $2p$  subshell is initially occupied, we expect no participator Auger broadening effects for  $n = 2$  excited states. And since we are interested in metastable states only for comparison with experimental results, we are not concerned with Auger broadening effects. Instead, we artificially broaden the  $1s2s2p^2(^4S, ^4P, ^4D)$  resonances with a significantly large width and found that it has no noticeable effect as expected in this energy region due to the broad natural, predominantly participator Auger, widths.

Our procedure used to determine the  $C^{2+}$  radial orbitals, using HF [31] and MCHF [32] optimizations, is shown in Table 3.7.

**Table 3.7** Criterion for determination of  $C^{2+}$  physical  $1s$ ,  $2s$ , and  $2p$  orbitals and correlation (or pseudo)  $\overline{3s}$ ,  $\overline{3p}$ , and  $\overline{3d}$  orbitals.

$1s$ and $2s$	HF on $1s^22s^2(^1S)$ term.
$2p$	HF on $1s^22s2p(^3P)$ term with frozen-core approximations for $1s$ and $2s$ .
$\overline{3s}$ , $\overline{3p}$ , and $\overline{3d}$	MCHF calculation for the lowest K-shell vacancy $1s2s^22p(^3P)$ term including single and double $2 \rightarrow 3$ promotions.

In these calculations, an inspection of energies is often a first indicator of the accuracy of the wave function representation. We show relative energies and corresponding photon energies for those states involved in ground state and metastable state photoabsorption cal-

culations in Table 3.8 and Table 3.9, respectively. Furthermore, a comparison of photon energies for B-like and Be-like C fluorescence yield calculations in LS-coupling, and earlier published experimental and theoretical results, is shown. Good agreement is obtained between our R-matrix and AUTOSTRUCTURE results. The earlier theoretical and experimental results predict the order of the resonantly-excited states of metastable configuration as  ${}^4D$ ,  ${}^4P$ , and  ${}^4S$  (lowest to highest energy), whereas our results, using two different theoretical methods, give the order as  ${}^4S$ ,  ${}^4D$ , and  ${}^4P$ . We tracked down these states in neutral C photoabsorption calculations, where our  $C^+$  target states are for the  $e^- + C^+$  continuum; here we also found that the order is  ${}^4S$ ,  ${}^4D$ , and  ${}^4P$  (see Table 3.6).

In Fig. 3.8, a comparison of our present results with recent experimental and theoretical cross section results is shown for the energy region  $h\nu = 287$  eV-291 eV. Our present results predict more accurately the positions of the resonances at lower region to within 0.5 eV. Our present and the earlier R-matrix results both overestimate the oscillator strengths of the  ${}^2P$  and  ${}^2D$  states compared to experimental data. As for the background cross section, good agreement is found between experimental data and the two theories; this implies that the  $1s$  and  $2s$  photoionization processes are treated adequately in the present calculations.

For our ground state photoabsorption calculations, we considered Auger broadening for the 8-target states above the the first K-shell ionization threshold (see Table 3.8). The Auger lifetimes of these states are calculated by applying the Smith time-delay method [59] to electron scattering on the 5-electron system within R-matrix theory. These values are also readily available from our Be-like carbon fluorescence yields calculations. In Table 3.10, a comparison between present R-matrix, MCBP [41], and MCDF [62] Auger width results

**Table 3.8** Comparison of energies of the relevant  $C^+$  and  $C^{2+}$  states involved in the present investigation. The term energies are given relative to the  $1s^2 2s^2 ({}^1S)$  ground state of  $C^{2+}$ . The photon energies are given relative to the  $1s^2 2s^2 2p ({}^2P)$  ground state of  $C^+$ .

State	Term Energy (Ry)			Photon Energies (eV)				
	Present <sup>a</sup>	AUTO <sup>b</sup>	OTHER <sup>c</sup>	Present <sup>a</sup>	AUTO <sup>b</sup>	OTHER <sup>c</sup>	Earlier <sup>d</sup>	Experiment. <sup>e</sup>
1 $1s^2 2s^2 2p ({}^2P)$	-1.7977	-1.7125	-1.7921 <sup>c</sup>	0.0000	0.0000	0.0000 <sup>c</sup>		
2 $1s^2 2s^2 ({}^1S)$	0.0000	0.0000	0.0000 <sup>c</sup>	24.4594	23.2997	24.3835 <sup>c</sup>		
3 $1s^2 2s 2p ({}^3P)$	0.4745	0.5088	0.4777 <sup>c</sup>	30.9148	30.2227	30.8827 <sup>c</sup>		
4 $1s^2 2s 2p ({}^1P)$	0.9570	1.0378	0.9327 <sup>c</sup>	37.4803	37.4200	37.0736 <sup>c</sup>		
5 $1s^2 2p^2 ({}^3P)$	1.2649	1.3090	1.2528 <sup>c</sup>	41.6698	41.1102	41.4287 <sup>c</sup>		
6 $1s^2 2p^2 ({}^1D)$	1.3630	1.4625	1.3293 <sup>c</sup>	43.0041	43.1979	42.4700 <sup>c</sup>		
7 $1s^2 2p^2 ({}^1S)$	1.7881	1.8126	1.6632 <sup>c</sup>	48.7879	47.9619	47.0133 <sup>c</sup>		
8 $1s 2s^2 2p^2 ({}^2D)$	19.3645	21.2193		287.9289	312.0049		287.96	287.93 ± 0.03
9 $1s 2s^2 2p^2 ({}^2P)$	19.4001	21.2280		288.4137	312.1230		288.63	288.40 ± 0.03
10 $1s 2s^2 2p^2 ({}^2S)$	19.5509	21.3339		290.4649	313.5638		289.97	289.90 ± 0.03
11 $1s 2s^2 2p ({}^3P)$	21.3622	21.4315		315.1086	314.8919			
12 $1s 2s^2 2p ({}^1P)$	21.5849	21.6197		318.1394	317.4533			
13 $1s 2s ({}^1S) 2p^2 ({}^3P)$	21.9689	22.0065		323.3637	322.7163			
14 $1s 2s ({}^3S) 2p^2 ({}^3D)$	21.9997	22.0721		323.7827	323.6083			
15 $1s 2s ({}^3S) 2p^2 ({}^1D)$	22.3201	22.4594		328.1429	328.8780			
16 $1s 2s ({}^3S) 2p^2 ({}^3S)$	22.3269	22.3359		328.2346	327.1971			
17 $1s 2s ({}^3S) 2p^2 ({}^3P)$	22.4088	22.5559		329.3490	330.1908			
18 $1s 2s ({}^3S) 2p^2 ({}^1P)$	22.5674	22.6623		331.5073	331.6378			
19 $1s 2s ({}^1S) 2p^2 ({}^1S)$	22.6511	22.7227		332.6456	332.4600			
20 $1s 2p^3 ({}^3D)$	22.6802	22.7892		333.0421	333.3647			
21 $1s 2p^3 ({}^3S)$	22.7780	22.8081		334.3724	333.6218			
22 $1s 2p^3 ({}^1D)$	22.8708	22.9786		335.6354	335.9417			
23 $1s 2p^3 ({}^3P)$	22.9926	23.0742		337.2918	337.2421			
24 $1s 2p^3 ({}^1P)$	23.1865	23.2637		339.9309	339.8205			

<sup>a</sup> Present R-matrix results.

<sup>b</sup> MCBP AUTOSTRUCTURE results.

<sup>c</sup> NIST data.

<sup>d</sup> Earlier R-matrix results [79].

<sup>e</sup> ALS Experimental data [79].

**Table 3.9** Same as Table 3.8, showing the  $C^+$  metastable ground and K-shell excited states.

State	Term Energy (Ry)			Photon Energies (eV)				
	Present <sup>a</sup>	AUTO <sup>b</sup>	OTHER <sup>c</sup>	Present <sup>a</sup>	AUTO <sup>b</sup>	OTHER <sup>c</sup>	Earlier <sup>d</sup>	Experiment. <sup>e</sup>
1 $1s^2 2s 2p^2 (^4P)$	-1.8871	-1.8467	-1.8777 <sup>c</sup>	0.0000	0.0000	0.0000 <sup>c</sup>		
2 $1s^2 2s 2p (^3P)$	0.0000	0.0000	0.0000 <sup>c</sup>	25.6759	25.1260	25.5469 <sup>c</sup>		
3 $1s^2 2p^2 (^3P)$	0.7905	0.8002	0.7751 <sup>c</sup>	36.4309	36.0135	36.0929 <sup>c</sup>		
4 $1s 2s 2p^3 (^4S)$	19.2225	19.2684		287.2130	287.2880		287.73	
5 $1s 2s 2p^3 (^4D)$	19.2371	19.3402		287.4120	288.2650		287.29	287.25 ± 0.03
6 $1s 2s 2p^3 (^4P)$	19.4267	19.5026		289.9923	290.4746		289.46	289.42 ± 0.03
7 $1s 2s^2 2p (^3P)$	20.8877	20.9226		309.8698	309.7952			
8 $1s 2s (^3S) 2p^2 (^5P)$	21.0101	21.0044		311.5350	310.9080			
9 $1s 2s (^1S) 2p^2 (^3P)$	21.4944	21.4977		318.1248	317.6196			
10 $1s 2s (^3S) 2p^2 (^3D)$	21.5252	21.5633		318.5438	318.5116			
11 $1s 2s (^3S) 2p^2 (^3S)$	21.8524	21.8270		322.9958	322.1004			
12 $1s 2p^3 (^5S)$	21.9228	21.9204		323.9531	323.3703			
13 $1s 2s (^3S) 2p^2 (^3P)$	21.9343	22.0471		324.1101	325.0940			
14 $1s 2p^3 (^3D)$	22.2058	22.2804		327.8032	328.2680			
15 $1s 2p^3 (^3S)$	22.3036	22.2992		329.1336	328.5250			
16 $1s 2p^3 (^3P)$	22.5181	22.5653		332.0529	332.1454			

<sup>a</sup> Present R-matrix results.

<sup>b</sup> MCBP AUTOSTRUCTURE results.

<sup>c</sup> NIST data.

<sup>d</sup> Earlier R-matrix results [79].

<sup>e</sup> ALS Experimental data [79].

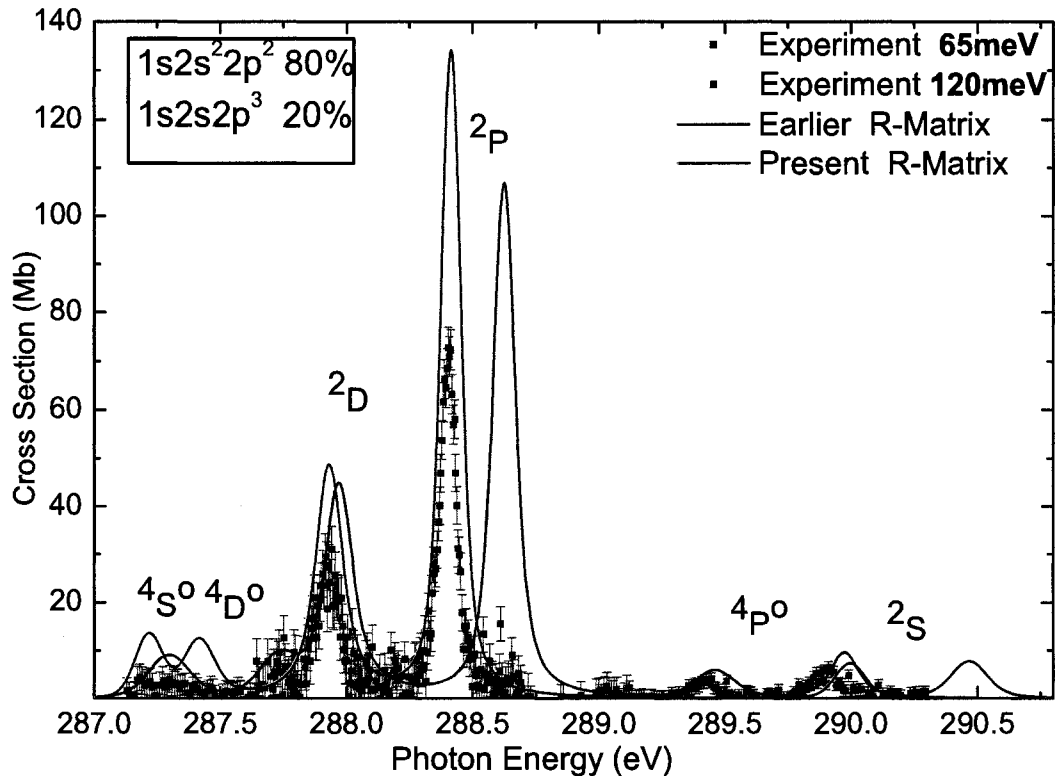


**Figure 3.8** The  $1s \rightarrow 2p$  photoabsorption for an admixture of 80% ground-state and 20% metastable state  $C^+$  ions. Experimental measurements are performed with a spectral resolution of 120 meV and 65 meV, whereas the theoretical cross sections are summed incoherently for an 80% ground-state and 20% metastable state admixture and then convoluted with a FWHM Gaussian of the same experimental width.

is shown. As seen, the Auger width of the  $1s2p^3(^3S)$  state is identically *zero* in our calculations. Considering the selection rules for Auger decay (see Sec. 2.1.3), it is found that no decay channels are coupled to the  $1s2p^3(^3S)$  state in a non-relativistic LS-approximation, whereas a fully-relativistic MCDF calculation gives a non-zero rate (but it is two orders of magnitude smaller than all other rates). Good agreement is found between all three theoretical approaches. In our calculations, we have artificially broadened this series with a width of  $\Gamma = 13.605 \times 10^{-3}$  eV, which is smaller than the best spectral resolutions of 3<sup>rd</sup>-generation synchrotron experiments and/or astrophysical observations.

**Table 3.10** Comparison of Auger widths for the relevant  $C^{2+}$  target states above the K-shell resonantly-excited states (see Table 3.8).

State	Present <sup>a</sup>	AUTO <sup>b</sup>	MCDF <sup>c</sup>
1 $1s2s^22p (^3P)$	$7.18E-02$	$7.93E-02$	$6.72E-02$
2 $1s2s^22p (^1P)$	$5.46E-02$	$5.30E-02$	$4.76E-02$
3 $1s2s(^1S)2p^2 (^3P)$	$1.10E-02$	$1.38E-02$	$2.47E-02$
4 $1s2s(^3S)2p^2 (^3D)$	$4.76E-02$	$5.17E-02$	$4.29E-02$
5 $1s2s(^3S)2p^2 (^1D)$	$9.07E-02$	$1.14E-01$	$1.13E-01$
6 $1s2s(^3S)2p^2 (^3S)$	$2.61E-02$	$2.39E-02$	$2.17E-02$
7 $1s2s(^3S)2p^2 (^3P)$	$4.64E-02$	$5.92E-02$	$4.91E-02$
8 $1s2s(^3S)2p^2 (^1P)$	$1.70E-02$	$1.17E-02$	$7.96E-03$
9 $1s2s(^1S)2p^2 (^1S)$	$7.46E-02$	$7.98E-02$	$8.36E-02$
10 $1s2p^3 (^3D)$	$5.76E-02$	$7.15E-02$	$6.08E-02$
11 $1s2p^3 (^3S)$	—	—	$1.17E-06$
12 $1s2p^3 (^1D)$	$5.99E-02$	$7.19E-02$	$6.02E-02$
13 $1s2p^3 (^3P)$	$3.56E-02$	$4.19E-02$	$3.67E-02$
14 $1s2p^3 (^1P)$	$3.60E-02$	$3.90E-02$	$3.53E-02$

<sup>a</sup> Present R-matrix calculations.

<sup>b</sup> MCBP AUTOSTRUCTURE calculations.

<sup>c</sup> MCDF calculations. [62]

A comparison of our present R-matrix results to the independent-particle approximation results, for the ground-state photoabsorption cross section of  $C^+$ , is shown in Fig.3.9. Good agreement is obtained between the present results using both length and velocity forms of the dipole operator, implying that the wave functions used to describe the atomic system are fairly converged.

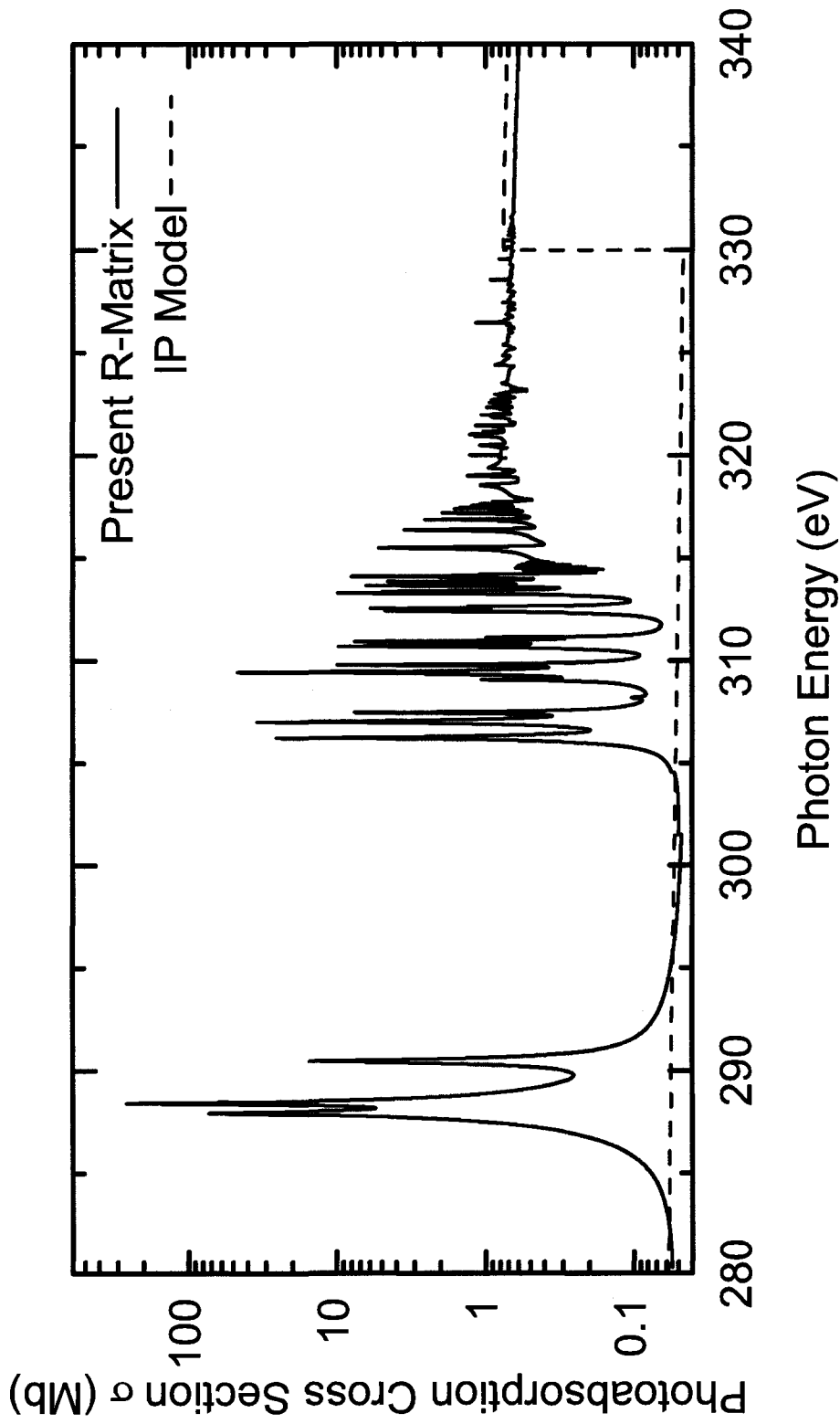


**Figure 3.9** Calculated K-shell photoabsorption cross section for the ground state of  $C^+$  at the K-edge compared to the oft-used, resonance-omitted, IP approximation results [77].

### 3.2.3 C<sup>2+</sup>: Importance of Auger Broadening

The specific process of interest for K-shell photoabsorption of ground state C<sup>2+</sup> is the following:

$$h\nu + 1s^2 2s^2 ({}^1P) \rightarrow 1s 2s^2 \{np, \epsilon p\} ({}^1P^o). \quad (3.14)$$

These K-shell excited states, as usual, can relax via two Auger processes:

$$1s 2s^2 np \rightarrow 1s^2 2s \epsilon \ell \quad \text{participator Auger decay,} \quad (3.15)$$

$$\rightarrow 1s^2 np \epsilon \ell \quad \text{spectator Auger decay.} \quad (3.16)$$

K-shell photoexcitation of C<sup>2+</sup> has been studied experimentally [81] using an electron-cyclotron-resonance ion source at the ALS. It was found that the C<sup>2+</sup> ion beam used in the experiment consists of an admixture of 62% of the ( $1s^2 2s^2 {}^1S$ ) ground state and 38% of the ( $1s^2 2s 2p {}^3P^o$ ) metastable state. Thus, we have also studied the  $1s \rightarrow 2p$  photoabsorption of the C<sup>2+</sup> metastable state.

The Hartree-Fock [31] and multi-configuration Hartree-Fock [32] atomic structure program packages are used to generate radial target C<sup>3+</sup> orbitals for our calculations. The optimization procedure (HF or MCHF) that we have used to generate C<sup>3+</sup> orbitals is summarized in Table 3.11 for each orbital.

In Table 3.12, we show the relative term energies and corresponding photon energies for the states involved in the ground state calculations compared to our MCBP results (in LS-coupling) and other available experimental and theoretical data. In Table 3.13, the term energies involved in the present metastable calculations are compared to other existing

**Table 3.11** Criterion for determination of  $C^{3+}$  physical  $1s$ ,  $2s$ , and  $2p$  orbitals and correlation (or pseudo)  $\overline{3s}$ ,  $\overline{3p}$ , and  $\overline{3d}$  orbitals.

$1s$ and $2s$	HF on $1s^2 2s$ ( $^2S$ ) term.
$2p$	HF on $1s^2 2p$ ( $^2P$ ) term with frozen-core approximation for $1s$ and $2s$ orbitals.
$\overline{3s}$ , $\overline{3p}$ , and $\overline{3d}$	MCHF calculation for the lowest $C^{2+}$ K-shell vacancy $1s 2s 2p$ ( $^4P$ ) term including single and double $2 \rightarrow 3$ promotions.

values. Good agreement between our present R-matrix and MCBP calculations is found for the state energies.

**Table 3.12** Comparison of energies of the relevant  $C^{2+}$  and  $C^{3+}$  states involved in the present investigation. The term energies are given relative to the  $1s^2 2s$  ( $^2S$ ) ground state of  $C^{2+}$ . The photon energies are given relative to the  $1s^2 2s^2$  ( $^1S$ ) ground state of  $C^{2+}$ .

State	Term Energy (Ry)			Photon Energies (eV)				
	Present <sup>a</sup>	AUTO <sup>b</sup>	OTHER	Present <sup>a</sup>	AUTO <sup>b</sup>	OTHER <sup>c</sup>	Earlier <sup>d</sup>	Experiment <sup>e</sup>
1 $1s^2 2s^2$ ( $^1S$ )	-3.5264	-3.5068	-3.5197	0.0000 <sup>c</sup>	0.0000	0.0000 <sup>c</sup>		
2 $1s^2 2s$ ( $^2S$ )	0.0000	0.0000	0.0000	47.9798 <sup>c</sup>	47.7127	47.8882 <sup>c</sup>		
3 $1s^2 2p$ ( $^2P$ )	0.5903	0.6253	0.5883	56.0108 <sup>c</sup>	56.2210	55.8921 <sup>c</sup>		
4 $1s 2s^2 2p^1$ ( $^1P$ )	18.0492	18.1128		293.9240	294.1516		294.08	293.94 ± 0.03
5 $1s 2s^2 3p^1$ ( $^1P$ )	20.1745	20.1796		322.8400	322.2721		322.84	322.93 ± 0.04
6 $1s 2s^2$ ( $^2S$ )	21.3887	21.3849		339.3608	338.6710			
7 $1s 2s$ ( $^1S$ ) $2p$ ( $^2P$ )	22.0009	22.0294		347.6898	347.4403			
8 $1s 2s$ ( $^3S$ ) $2p$ ( $^2P$ )	22.2608	22.3689		351.2252	352.0598			
9 $1s 2p^2$ ( $^2D$ )	22.4955	22.5704		354.4195	354.8012			
10 $1s 2p^2$ ( $^2P$ )	22.5767	22.5955		355.5240	355.1431			
11 $1s 2p^2$ ( $^2S$ )	23.0266	23.0505		361.6445	361.3332			

<sup>a</sup> Present R-matrix results.

<sup>b</sup> AUTOSTRUCTURE results.

<sup>c</sup> NIST data.

<sup>d</sup> Earlier R-matrix results [81].

<sup>e</sup> ALS Experimental data [81].

**Table 3.13** Same as Table 3.12, showing the  $C^{2+}$  metastable ground and K-shell excited states.

State	Term Energy (Ry)			Photon Energies (eV)				
	Present <sup>a</sup>	AUTO <sup>b</sup>	OTHER	Present <sup>a</sup>	AUTO <sup>b</sup>	OTHER	Earlier <sup>d</sup>	Experiment. <sup>e</sup>
1 $1s^2 2s 2p (^3P)$	-3.0499	-2.9981	-3.0420 <sup>c</sup>	0.0000	0.0000	0.0000 <sup>c</sup>		
2 $1s^2 2s (^2S)$	0.0000	0.0000	0.0000 <sup>c</sup>	41.4963	40.7916	41.3889 <sup>c</sup>		
3 $1s^2 2p (^2P)$	0.5903	0.6253	0.5883 <sup>c</sup>	49.5273	49.2998	49.3929 <sup>c</sup>		
4 $1s 2s (1S) 2p^2 (^3P)$	18.4423	18.5000		292.7890	292.4984		292.97	292.98 ± 0.03
5 $1s 2s (3S) 2p^2 (^3D)$	18.4624	18.5652		293.0620	293.3856		292.78	292.80 ± 0.03
6 $1s 2s (3S) 2p^2 (^3S)$	18.7927	18.8289		297.5560	296.9744		296.73	296.62 ± 0.2
7 $1s 2s (3S) 2p^2 (^3P)$	18.8845	19.0494		298.8054	299.9736			
8 $1s 2s^2 (^2S)$	21.3887	21.3849		332.8773	331.7499			
9 $1s 2s (3S) 2p (^4P)$	21.5576	21.5661		335.1741	334.2159			
10 $1s 2s (1S) 2p (^2P)$	22.0009	22.0294		341.2063	340.5192			
11 $1s 2p^2 (^4P)$	22.2378	22.2662		344.4290	343.7417			
12 $1s 2s (3S) 2p (^2P)$	22.2608	22.3689		344.7417	345.1387			
13 $1s 2p^2 (^2D)$	22.4955	22.5704		347.9360	347.8801			
14 $1s 2p^2 (^2P)$	22.5767	22.5955		349.0405	348.2220			
15 $1s 2p^2 (^2S)$	23.0266	23.0505		355.1610	354.4121			

<sup>a</sup> Present R-matrix results.

<sup>b</sup> MCBP AUTOSTRUCTURE results.

<sup>c</sup> NIST data.

<sup>d</sup> Earlier R-matrix results [81].

<sup>e</sup> ALS Experimental data [81].

Theoretical calculations and experimental measurements for the total cross sections are in good agreement in terms of the positions of the  $^3P$ ,  $^3D$ , and  $^1P^o$  resonances. Furthermore, both theoretical results show fair agreement for the line strength of the  $1s 2s^2 2p ^1P^o$  resonance.

Having analyzed our results for each partial cross section, we found the two low-lying resonances to be in energy order  $^3P$  and  $^3D$ , as shown in Fig. 3.10a. The earlier published RMPS results [81], on the other hand, order them as  $^3D$  and  $^3P$ . Our MCBP (in LS-

coupling scheme) calculation for the B-like C fluorescence yield also gives the order as  ${}^3P$  and  ${}^3D$  (see Table 3.12). Furthermore, the coupling of the  $1s2s2p^2$  configuration gives two  ${}^3P$  terms; the first one comes from the  $1s2s({}^3S)$  parent whereas the second one comes from the  $1s2s({}^1S)$  parent. We have studied the angular momentum algebra of the  $1s \rightarrow 2p$  dipole excitation of the  $1s^22s2p({}^3P)$  term to see if any of these states are forbidden and found that the  $1s2s({}^3S)2p^2({}^4P){}^3P$  term can not be populated in a SC description, but instead is populated through CI effects. We have detected this resonance in our cross section and found it strong enough to be observed with both 133 meV or 200 meV spectral resolutions (see Fig. 3.10c).

The Auger widths from R-matrix and MCBP calculations, for the six autoionizing target states above the K-shell ionization threshold, are shown in Table 3.14. These R-matrix results are obtained using the Smith-time delay method (see Sec. 2.4.1) with the electron scattering from  $C^{3+}$  target states. The resonances unaccounted for in our MCBP calcula-

**Table 3.14** Auger width results obtained from different methods for the thresholds above the K-shell excited states (see Table 3.12).

	State	Present <sup>a</sup>	AUTO <sup>b</sup>
1	$1s2s^2({}^2S)$	$6.99E - 02$	$7.12E - 02$
2	$1s2s({}^1S)2p({}^2P)$	$3.95E - 03$	
3	$1s2s({}^3S)2p({}^2P)$	$3.64E - 02$	
4	$1s2p^2({}^2D)$	$5.48E - 02$	$6.07E - 02$
5	$1s2p^2({}^2P)$		
6	$1s2p^2({}^2S)$	$8.76E - 03$	$5.22E - 03$

<sup>a</sup> Present R-matrix results.

<sup>b</sup> MCBP AUTOSTRUCTURE results.

tions are due to neglect of the coupling between the continuum and the target states within a DW calculations (see Sec 2.4 and Sec. 2.2.5). The R-matrix width results are used for the broadening of the  $1s \rightarrow 2p$  resonance series attached to these target states.

The present R-matrix results, using both length and velocity forms of the dipole operator, are found to be in good agreement. We have also calculated our cross sections without considering broadening to emphasize the effect of Auger broadening on the cross sections. A comparison of these two results is shown in Fig 3.11. The importance of the broadening is seen even at low  $n = 3$  value, where the resonance profile is obviously qualitatively affected (see Fig. 3.10c and 3.11).

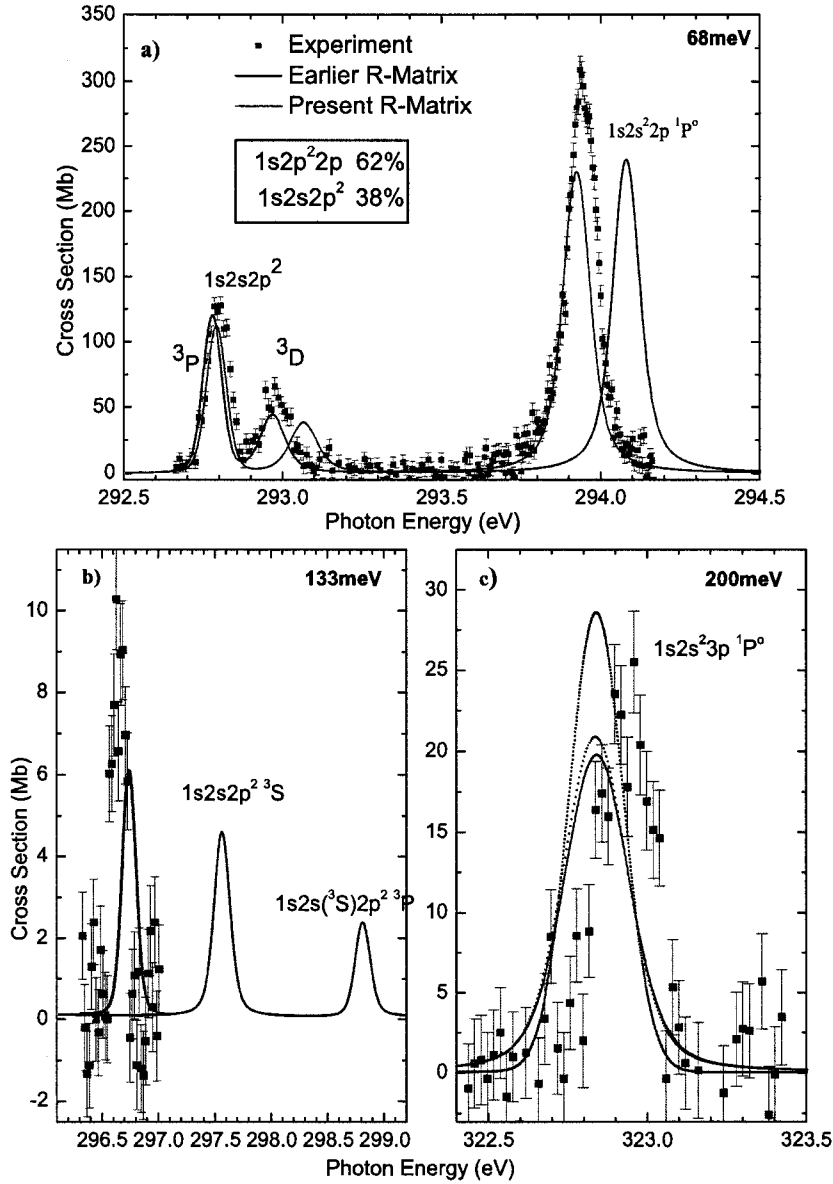


**Figure 3.10** Experimental measurements and present and earlier R-matrix theoretical calculations of  $1s \rightarrow 2p$  and  $3p$  absorption resonances of  $C^{2+}$  ions. Theoretical curves are determined by considering an admixture of 68% of the ground-state and 32% of the metastable state. These mixed cross sections are convoluted with a FWHM Gaussian given by the experiment spectral resolution. **a)** Comparison between  $1s2s2p^2$  ( $^3P$ ,  $^3D$ ) and  $1s2s^22p^2$  ( $^1P$ ) absorption cross sections at a spectral resolution of 68 meV. **b)** Comparison between the  $1s2s2p^2$  ( $^3S$ ) and  $1s2s(^3S)2p^2$  ( $^3P$ ) absorption cross sections at a spectral resolution of 133 meV. **c)** Comparison between the  $1s2s^23p$  ( $^1P$ ) absorption cross sections at a spectral resolution of 200 meV. The black curve shows our results without Auger broadening (see Fig 3.11)

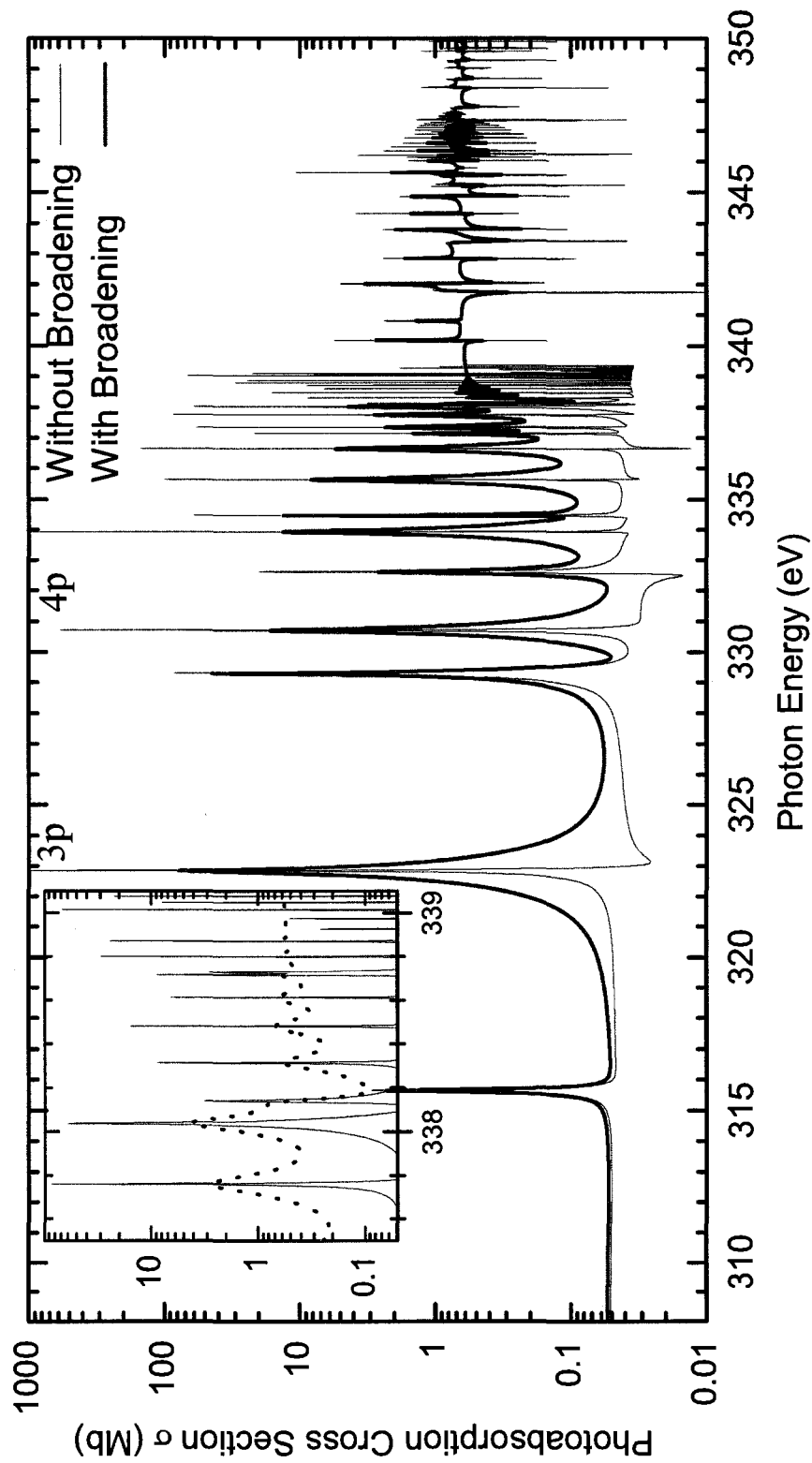


**Figure 3.11** Present R-matrix results with and without Auger broadening effects for the ground state photoabsorption of  $C^{2+}$  at the K-edge. Auger broadening becomes more important at higher- $n$ , as expected. The lowest resonances,  $n = 3, 4$ , responsible for the  $1s^2 2s^2 ({}^1S) \rightarrow 1s^2 2s^2 np ({}^1P^o)$  photoabsorptions are labeled. The effect of broadening in the vicinity of the  $1s^2 2s^2 ({}^3S) 2p ({}^2P)$  threshold is shown in the inset.

## CHAPTER IV

### SUMMARY AND FUTURE DIRECTIONS

The majority of funding for this research was provided by NASA APRA and NASA SHP SR&T programs. Thus, this dissertation focused on two astrophysically important atomic processes, K-shell X-ray photoemission (or Auger transition) and K-shell X-ray photoabsorption. Through these studies, much information has been gained both in the underlying theoretical atomic physics processes and in the necessary effects that need to be considered for computing reliable astrophysical transition rates. Such modeling by astrophysicists/astronomers aids in the interpretation, among other things, of the chemical evolution of the universe. Interesting theoretical atomic physics findings, and the necessary considerations for reliable application to astrophysics, have been discovered.

Following earlier WMU studies [12] on K-shell fluorescence yields that first investigated the presently-recommended database [3], we have conducted three new investigations aimed at producing the most reliable fluorescence yields of individual Auger and radiative rates for all 2<sup>nd</sup>-row ions. In these calculations, our results show good agreement with other sparsely-available theoretical results, giving us confidence in the accuracy of our comprehensive computed rates for the entire 2<sup>nd</sup>-row isoelectronic sequences up through ten-electron systems. In these studies, inclusion of several important effects, such as spin-orbit interaction, CI effects, initial-state populations of a K-shell vacancy state, and avoided-crossing phenomena are found to be crucial for producing reliable atomic parameters for astrophysical plasma modeling. This has resulted in three publications [40, 41, 42].

Two future publications are in progress: the first is a survey of fluorescence yields of 2<sup>nd</sup>-row ions [73], and the second is a comprehensive computation and tabulation of all transition data [74].

A secondary project, aimed at computing carbon K-shell photoabsorption cross sections, was undertaken in order to provide neutral carbon data for determining ISM abundances and the instrumental calibration [1]. Here we have used a more sophisticated R-matrix method, yielding, to our knowledge, the first carbon K-shell photoabsorption cross section spectra. Further, we continued to compute photoabsorption cross sections for the additional C<sup>+</sup> and C<sup>2+</sup> isonuclear members, for which synchrotron-facility measurements at the ALS had already studied the lowest  $1s \rightarrow 2p, 3p$  resonance transitions in C<sup>+</sup> and C<sup>2+</sup>: favorable agreement is found between our present results and the experimental measurements except for one puzzling case, which is still unresolved. In addition to these lowest resonances, we have studied the higher  $1s \rightarrow np$  resonance features that are also important for astrophysical studies. Publication of these studies along the complete isonuclear sequence is in progress [82].

**Appendix A**  
**Atomic Units**

For theoretical simplicity, atomic units are the most used system for describing the electron-ion systems. Atomic units yield the simplification that  $\hbar = m = e = 1$  and likewise based on the typical dimensions of a hydrogen atom. These are tabulated in Table A.1 (Note that fine-structure constant  $\alpha = k e^2/(\hbar c) = 1/137.03599967$ ).

**Table A.1** Fundamental atomic units and conversion factors

Physical Quantity	Unit	Name	SI Value
Mass	$m$	Electron rest mass	$9.10938215 \times 10^{-31}$ kg
Angular Momentum	$\hbar = h/2\pi$	Planck's constant divided by $2\pi$	$1.05457162 \times 10^{-34}$ J.s
Charge	$e$	Charge of proton and electron	$1.60217648 \times 10^{-19}$ C
Electrostatic force constant	$k_e = (4\pi\epsilon_0)^{-1}$	Coulomb's constant	$8.9875518 \times 10^9$ N.m <sup>2</sup> /C <sup>2</sup>
Length	$a_0 = \hbar/(m c \alpha)$	Borh radius	$0.52917720 \times 10^{-10}$ m
Velocity	$\alpha c$	Hydrogen ground state electron speed	$2.18769125 \times 10^6$ m/s
Time	$a_0/(\alpha c)$	Hydrogen ground state electron period	$2.41888432 \times 10^{-17}$ s
Energy	$E_h = m(c\alpha)^2$	Twice the binding energy for the electron in the ground state of hydrogen.	$4.359743 \times 10^{-18}$ J = 27.211 eV

**Appendix B**  
**Z-Scaling of Relevant Physical Variables**

In order to derive  $Z$ -scaling of the physical variables for hydrogenic systems with arbitrary nuclear charge,  $Z$ , let us look at the reduced form of Schrödinger equation for the radial orbitals (one-electron wave functions are considered in the form of Eq. 2.3) [2, 38, 70].

$$\left[ -\frac{1}{2} \frac{d^2}{dr^2} + \frac{1}{2} \frac{l(l+1)}{r^2} - \frac{Z}{r} - E_{nl} \right] P_{nl}(r) = 0. \quad (\text{B.1})$$

Here the *bound* solutions  $P_{nl}(r)$  must be normalized according to expression

$$\int_0^\infty P_{nl}^*(r) P_{nl}(r) dr = 1. \quad (\text{B.2})$$

To factor out the  $Z$ -dependence, we consider the transformation  $\rho = Zr$ .

### **Bound Orbitals**

To understand the  $Z$ -dependence of the radial orbitals  $P_{nl}(r)$ , we define the  $\rho$ -dependent function  $f_{nl}(\rho)$  by  $P_{nl}(r) \equiv C_{nl} f_{nl}(\rho)$ . Here,  $C_{nl}$  which can be determined from the normalization requirement in Eq. 2.26 as a function of  $Z$  by considering that

$$\begin{aligned} \int_0^\infty P_{nl}^*(r) P_{nl}(r) dr &= 1, \quad \text{so that} & (\text{B.3}) \\ \int_0^\infty C_{nl}^* F_{nl}^*(\rho) C_{nl} F_{nl}(\rho) \frac{d\rho}{Z} &= 1, \quad \text{and} \\ \frac{|C_{nl}|^2}{Z} \int_0^\infty |F_{nl}(\rho)|^2 d\rho &= 1. \end{aligned}$$

The normalization of  $F_{nl}(\rho)$  thus shows the  $Z$ -dependence is  $C_{nl} = Z^{1/2}$ , and therefore,  $P_{nl}(r) \sim Z^{1/2}$ .

### **Energies**

In order to find the  $Z$ -dependence of the energy,  $E_{nl}$ , let us start with Eq B.1. First, we multiply both sides by  $P_{nl}(r)$  and integrating from 0 to  $\infty$  as follow:

$$E_{nl} \int_0^\infty P_{nl}^*(r) P_{nl}(r) dr = \int_0^\infty P_{nl}^*(r) \left[ -\frac{1}{2} \frac{d^2}{dr^2} + \frac{1}{2} \frac{l(l+1)}{r^2} - \frac{Z}{r} \right] P_{nl}(r) dr .$$

Using the normalization in Eq. B.3 of the radial orbitals,

$$E_{nl} = \int_0^\infty P_{nl}^*(r) \left[ -\frac{1}{2} \left( \frac{d^2}{dr^2} - \frac{l(l+1)}{r^2} \right) - \frac{Z}{r} \right] P_{nl}(r) dr,$$

and since we know how  $r$  and  $P_{nl}(r)$  scale with  $Z$ , we can get the  $Z$ -scaling of the energy:

$$\begin{aligned} E_{nl} &= \int_0^\infty Z^{1/2} F_{nl}^* \left[ -\frac{Z^2}{2} \frac{d^2}{d\rho^2} + \frac{Z^2 l(l+1)}{2\rho^2} - \frac{Z^2}{\rho} \right] Z^{1/2} F_{nl} \frac{d\rho}{Z}, \\ &= Z^2 \int_0^\infty F_{nl}^* \left[ -\frac{1}{2} \frac{d^2}{dr^2} + \frac{l(l+1)}{2\rho^2} - \frac{1}{\rho} \right] F_{nl} d\rho . \end{aligned} \quad (\text{B.4})$$

The  $Z$ -independent integral expression gives us the hydrogenic ( $Z = 1$ ) energy,  $E_{nl}^H = -\frac{1}{2n^2}$  a.u (this, of course, is within a non-relativistic framework). We see that  $E_{nl} = Z^2 E_{nl}^H \sim Z^2$ .

### **Continuum Orbitals**

In contrast to bound orbitals, continuum orbitals are defined as a function of energy  $P_{en}(r)$ . Also, normalization of continuum orbitals is given instead by

$$\int_0^\infty P_{\epsilon l}(r)^* P_{\epsilon' l}(r) dr = \delta(\epsilon - \epsilon') .$$

Applying the  $\rho = Zr$  transformation and considering radial orbitals transform as  $P_{\epsilon l}(r) = C_{\epsilon l} F_{E l}(\rho)$ . In the preceding section under such transformation, we showed that energy behaves as  $\epsilon \sim Z^2$ . Performing a transformation for continuum orbitals, the normalization is instead

$$\int_0^\infty C_{E l}^* F_{E l}(\rho)^* F_{E' l}(\rho) C_{E l} \frac{d\rho}{Z} = \delta(Z^2\{E - E'\}) = \frac{1}{Z^2} \delta(E - E'),$$

$$\frac{|C_{E l}|^2}{Z} \int_0^\infty F_{E l}(\rho)^* F_{E' l}(\rho) d\rho = \frac{1}{Z^2} \delta(E - E'), \quad (\text{B.5})$$

$$C_{E l} = Z^{-1/2} \Rightarrow P_{\epsilon l}(r) \sim Z^{-1/2}.$$

### ***Auger Decay Rates***

Although, Auger processes do not occur for the one-electron hydrogenic systems, we assume that the radial orbitals in a many-electronic system scale as similar to hydrogenic orbitals, which is true considering nuclear charge as the effective charge,  $Z \rightarrow Z^{eff}$ , in the Central Field Approximation. Let us consider an *allowed* Auger process that occurs when an electron makes a radiationless-transition from a bound state  $\phi_{n l}$  to a continuum states  $\phi_{\epsilon l'}$  while another electron makes a transition from a bound state  $\phi_{n' l'}$  to a second bound state  $\phi_{n'' l''}$ . By using Eq. 2.13, the Auger decay rate of this particular process can be written as

$$A_a \sim \left| \int \phi_{n'' l''}(r_1) \phi_{\epsilon l'}(r_2) \frac{1}{r_{12}} \phi_{n' l'}(r_1) \phi_{n l}(r_2) d^3 r_1 d^3 r_2 \right|^2.$$

Using the addition theorem of spherical harmonics, defined in Eq. 2.13, and recalling that the angular and spin integrals are independent of  $Z$ , this reduces to the two dimensional

radial integral

$$\begin{aligned}
A_a &\sim \left| \sum_{k=0}^{\infty} \int_0^{\infty} \int_0^{\infty} P_{n''l''}(r_1) P_{\epsilon l}(r_2) \frac{r_1^k}{r_2^{k+1}} P_{n'l'}(r_1) \phi_{nl}(r_2) dr_1 dr_2 \right|^2 \\
&\sim \left| \sum_{k=0}^{\infty} Z^{1/2} Z^{-1/2} \frac{Z^{k+1}}{Z^k} Z^{1/2} Z^{1/2} Z^{-1} Z^{-1} \right|^2 = Z^0.
\end{aligned} \tag{B.6}$$

Thus, the Auger rate  $A_a$  is (roughly) independent of the nuclear charge,  $Z$ .

### ***Radiative Decay Rates***

The radiative decay rate of a dipole-allowed transition with energy  $\omega$  from a bound state  $\phi_{nl}$  to another bound state  $\phi_{n'l'}$  is given in Eq 2.12. This expression is proportional to the radial integral between these two states as follows:

$$\begin{aligned}
A_r &\sim \omega^3 \left| \int \phi_{n'l'}(r) r \phi_{nl}(r) d^3r \right|^2 \\
&\sim \omega^3 \left| \int_0^{\infty} P_{n'l'}(r) r P_{nl}(r) dr \right|^2 \\
&\sim Z^6 |Z^{1/2} Z^{-1} Z^{1/2} Z^{-1}|^2 = Z^4.
\end{aligned} \tag{B.7}$$

### ***Spin-Orbit Interaction***

We now consider the  $Z$ -dependence of the spin-orbit interaction presented in Sec. 2.1.2. This can be determined by looking at the expectation value of this operator. Because the states are normalized, we only need to consider the  $Z$ -dependence of the operator  $\mathcal{H}_{SO}$ :

$$\mathcal{H}_{SO} \sim Z \frac{1}{r^3} = Z Z^3 = Z^4. \tag{B.8}$$

In this appendix, we have considered hydrogenic scaling, which is exact for hydrogenic systems but only an approximation for many-electron systems. For non-hydrogenic systems with nuclear charge of  $Z$ , a more rigorous approximation can be done by defining effective charge as  $Z_{nl}^{eff} = Z - S_{nl}$ , where  $S_{nl}$  is the “screening parameter” due to all other electrons [30].

## BIBLIOGRAPHY

1. J. Drake, Private Communication, (2006).
2. R. D. Cowan, *The Theory of Atomic Structure and Spectra* (Berkeley: University of California Press, 1981).
3. J. S. Kaastra and R. Mewe, "X-ray Emission from Thin Plasmas. I. Multiple Auger Ionisation and Fluorescence Processes for Be to Zn", *Astronomy & Astrophysics Supplement Series* **97**, 443 (1993).
4. E. J. McGuire, "Atomic Photo-Ionization Cross Sections from a Semiempirical Central Potential", *Physical Review* **161**, 51 (1967).
5. E. J. McGuire, "K-Shell Auger Transition Rates and Fluorescence Yields for Elements Be-Ar", *Physical Review* **185**, 1 (1969).
6. E. J. McGuire, "K-Shell Auger Transition Rates and Fluorescence Yields for Elements Ar-Xe", *Physical Review A* **2**, 273 (1970).
7. E. J. McGuire, "Atomic L-Shell Coster-Kronig, Auger, and Radiative Rates and Fluorescence Yields for Na-Th", *Physical Review A* **3**, 587 (1971).
8. E. J. McGuire, "M-Shell Auger and Coster-Kronig Electron Spectra", *Physical Review A* **5**, 1052 (1972).
9. G. J. Ferland, K. T. Korista, D. A. Verner, J. W. Ferguson, J. B. Kingdon, and E. M. Verner, "CLOUDY 90: Numerical Simulation of Plasmas and Their Spectra", *The Astronomical Society of the Pacific* **110**, 761 (1998).
10. M. A. Bautista and T. R. Kallman, "The XSTAR Atomic Database", *Astrophysical Journal Supplement Series* **134**, 139 (2001).
11. K. J. Borkowski, W. J. Lyerly, and S. P. Reynolds, "Supernova Remnants in the Sedov Expansion Phase: Thermal X-ray Emission", *Astrophysical Journal* **548**, 820 (2001).
12. T. W. Gorczyca, C. N. Kodontuwakku, K. T. Korista, O. Zatsarinny, N. R. Badnell, E. Behar, M. H. Chen, and D. W. Savin, "Assessment of the Fluorescence and Auger Database Used in Plasma Modeling", *The Astrophysical Journal* **592**, 636 (2003).
13. N. R. Badnell, "Dielectronic Recombination of  $Fe^{22+}$  and  $Fe^{21+}$ ", *Journal of Physics B: Atomic and Molecular Physics* **19**, 3827 (1986).
14. A. M. Juett, N. S. Schulz, D. Chakrabarty, and T. W. Gorczyca, "High-Resolution X-Ray Spectroscopy of the Interstellar Medium. II. Neon and Iron Absorption Edges", *The Astrophysical Journal* **648**, 1066 (2006).

15. T. W. Gorczyca, “Auger Decay of the Photoexcited  $1s^{-1} \rightarrow np$  Rydberg Series in Neon”, *Physical Review A* **61**, 024702 (2000).
16. J. Garcia, C. Mendoza, M. A. Bautista, T. W. Gorczyca, T. R. Kallman, and P. Palmeri, “K-Shell Photoabsorption of Oxygen Ions”, *The Astrophysical Journal Supplement Series* **158**, 68 (2005).
17. T. W. Gorczyca and B. M. McLaughlin, “Inner-Shell Photoexcited Resonances in Atomic Oxygen”, *Journal of Physics B: Atomic, Molecular and Optical Physics* , L859 (2000).
18. A. M. Juett, N. S. Schulz, and D. Chakrabarty, “High-Resolution X-Ray Spectroscopy of the Interstellar Medium: Structure at the Oxygen Absorption Edge”, *The Astrophysical Journal* **612**, 308 (2004).
19. T. W. Gorczyca and F. Robicheaux, “Auger Decay of the Photoexcited  $2p^{-1}nl$  Rydberg Series in Argon”, *Physical Review A* **60**, 1216 (1999).
20. S. E. Canton-Rogan, A. A. Wills, T. W. Gorczyca, M. Wiedenhoef, O. Nayandin, C.-N. Liu, and N. Berrah, “Mirroring Doubly Excited Resonances in Argon”, *Physical Review Letters* **85**, 3113 (2000).
21. W. Eissner, M. Jones, and H. Nussbaumer, “Techniques for the Calculation of Atomic Structures and Radiative Data Including Relativistic Corrections”, *Computer Physics Communications* **8**, 270 (1974).
22. E. P. Wigner, “Resonance Reactions and Anomalous Scattering”, *Phys. Rev.* **70**, 15 (1946).
23. E. P. Wigner and L. Eisenbud, “Higher Angular Momenta and Long Range Interaction in Resonance Reactions”, *Physical Review* **72**, 29 (1947).
24. A. M. Lane and R. G. Thomas, “R-Matrix Theory of Nuclear Reactions”, *Reviews of Modern Physics* **30**, 257 (1958).
25. P. G. Burke and K. A. Berrington, *Atomic and Molecular Processes: an R-Matrix Approach* (Institute of Physics, Bristol, 1993).
26. P. G. Burke and W. D. Robb, “The R-Matrix Theory of Atomic Processes”, in *Advances in Atomic and Molecular Physics*, edited by D. R. Bates and I. Estermann, volume 11, p. 143, Academic Press, New York, 1975.
27. K. A. Berrington, W. B. Eissner, and P. H. Norrington, “RMATRIX1: Belfast Atomic R-Matrix Codes”, *Computer Physics Communications* **92**, 290 (1995).
28. T. W. Gorczyca, F. Robicheaux, M. S. Pindzola, D. C. Griffin, and N. R. Badnell, “Elimination of Electron-Ion Pseudoresonances Associated with Approximate Target Wave Functions”, *Phys. Rev. A* **52**, 3877 (1995).

29. C. Froese Fischer, *The Hartree-Fock Method for Atoms: a Numerical Approach* (Wiley, New York, 1977).
30. C. Froese Fischer, T. Brage, and P. Jönsson, *Computational Atomic Structure: an MCHF Approach* (Institute of Physics Publ., Bristol, UK, 1997).
31. C. Froese Fischer, "General Hartree-Fock Program", *Computer Physics Communications* **43**, 355 (1987).
32. C. Froese Fischer, "The MCHF Atomic-Structure Package", *Computer Physics Communications* **64**, 369 (1991).
33. E. Merzbacher, *Quantum Mechanics*, 3<sup>rd</sup> ed. (Wiley, New York, 1998).
34. G. B. Arfken and H.-J. Weber, *Mathematical Methods for Physicists*, 5<sup>th</sup> ed. (Academic Press, San Diego, 1995).
35. A. R. Edmonds, *Angular Momentum in Quantum Mechanics* (Princeton University Press, Princeton, N.J., 1996).
36. D. M. Brink and G. R. Satchler, *Angular Momentum* (Clarendon P., Oxford, 1968).
37. E. U. Condon and G. H. Shortley, *The Theory of Atomic Spectra* (Cambridge Univ. Press, Cambridge, 1959).
38. B. H. Bransden and C. J. Joachain, *The Physics of Atoms and Molecules*, 2<sup>nd</sup> ed. (Prentice Hall, New York, 2002).
39. I. P. Grant, *Relativistic Quantum Theory of Atoms and Molecules: Theory and Computation* (Springer, New York, 2007).
40. T. W. Gorczyca, I. Dumitriu, M. F. Hasoglu, K. T. Korista, N. R. Badnell, D. W. Savin, and S. T. Manson, "Importance of Configuration Interaction for Accurate Atomic Data: Fluorescence Yields of K-Shell Vacancy, Lithium-like Ions", *The Astrophysical Journal Letters* **638**, L121 (2006).
41. M. F. Hasoglu, T. W. Gorczyca, K. T. Korista, S. T. Manson, N. R. Badnell, and D. W. Savin, "Strong LSJ Dependence of Fluorescence Yields: Breakdown of the Configuration Average Approximation", *The Astrophysical Journal Letters* **649**, L149 (2006).
42. M. F. Hasoglu, D. Nikolic, T. W. Gorczyca, S. T. Manson, M. H. Chen, and N. R. Badnell, "Nonmonotonic Behavior as a Function of Nuclear Charge of the K-Shell Auger and Radiative Rates and Fluorescence Yields Along the  $1s2s^22p^3$  Isoelectronic Sequence", *Physical Review A* **78**, 032509 (2008).
43. I. I. Sobelman, *Atomic Spectra and Radiative Transitions*, 2<sup>nd</sup> ed. (Springer-Verlag, Berlin, 1992).

44. H. Friedrich, *Theoretical Atomic Physics* (Springer, Berlin, 1998).
45. M. J. Seaton, “*The Hartree-Fock Equations for Continuous States with Applications to Electron Excitation of the Ground Configuration Terms of O I*”, *Philosophical Transactions of the Royal Society of London* **245**, 469 (1953).
46. D. R. Hartree, “*The Wave Mechanics of an Atom with a Non-Coulomb Central Field. Part I. Theory and Methods*”, *Mathematical Proceedings of the Cambridge Philosophical Society* **24**, 89 (1928).
47. V. Fock, “*Näherungsmethode zur Lösung des quantenmechanischen Mehrkörperproblems*”, *Zeitschrift für Physik A Hadrons and Nuclei* **61**, 126 (1930).
48. V. Fock, “*Selfconsistent field mit Austausch für Natrium*”, *Zeitschrift für Physik A Hadrons and Nuclei* **62**, 795 (1930).
49. C. Zener, “*Analytic Atomic Wave Functions*”, *Physical Review* **36**, 51 (1930).
50. J. C. Slater, “*Atomic Shielding Constants*”, *Physical Review* **36**, 57 (1930).
51. W. Eissner and H. Nussbaumer, “*A Programme for Calculating Atomic Structures*”, *Journal of Physics B: Atomic and Molecular Physics* **2**, 1028 (1969).
52. W. Eissner, M. Jones, P. Storey, and H. Nussbaumer, “*SUPERSTRUCTURE II*”, Unpublished (1994).
53. A. Burgess, H. E. Mason, and J. A. Tully, “*Coronal Mg<sup>+9</sup>: Collisional Excitation of the 2s-2p Multiplet*”, *Astronomy and Astrophysics* **217**, 319 (1989), West Germany.
54. P. G. Burke and K. Smith, “*The Low-Energy Scattering of Electrons and Positrons by Hydrogen Atoms*”, *Reviews of Modern Physics* **34**, 458 (1962).
55. P. G. Burke, “*The R-Matrix Method in Atomic Physics*”, *Computer Physics Communications* **6**, 288 (1973).
56. K. A. Berrington, P. G. Burke, J. J. Chang, A. T. Chivers, W. D. Robb, and K. T. Taylor, “*A General Program to Calculate Atomic Continuum Processes Using the R-Matrix Method*”, *Computer Physics Communications* **8**, 149 (1974).
57. C. Bloch, “*Une Formulation Unifie de la Theorie des Reactions Nuclaires*”, *Nuclear Physics* **4**, 503 (1957).
58. A. F. Starace, “*Theory of Atomic Photoionization*”, in *Encyclopedia of Physics*, edited by W. Mehlhorn, p. 1.
59. F. T. Smith, “*Lifetime Matrix in Collision Theory*”, *Physical Review* **118**, 349 (1960).

60. M. A. Bautista, C. Mendoza, T. R. Kallman, and P. Palmeri, “*Atomic Data for the K-Vacancy States of Fe XXIV*”, *Astronomy and Astrophysics* **403**, 339 (2003).
61. M. Hsiung Chen, “*Dielectronic Satellite Spectra for He-like Ions*”, *Atomic Data and Nuclear Data Tables* **34**, 301 (1986).
62. M. H. Chen and B. Crasemann, “*K-Shell Auger and Radiative Transitions in the Boron Isoelectronic Sequence*”, *Atomic Data and Nuclear Data Tables* **38**, 381 (1988).
63. P. Palmeri, C. Mendoza, T. R. Kallman, and M. A. Bautista, “*A Complete Set of Radiative and Auger Rates for K-Vacancy States in Fe XVIII-Fe XXV*”, *Astronomy and Astrophysics* **403**, 1175 (2003).
64. M. H. Chen, K. J. Reed, D. M. McWilliams, D. S. Guo, L. Barlow, M. Lee, and V. Walker, “*K-Shell Auger and Radiative Transitions in the Carbon Isoelectronic Sequence,  $6 \leq Z \leq 54$* ”, *Atomic Data and Nuclear Data Tables* **65**, 289 (1997).
65. I. P. Grant, B. J. McKenzie, P. H. Norrington, D. F. Mayers, and N. C. Pyper, “*An Atomic Multiconfigurational Dirac-Fock Package*”, *Computer Physics Communications* **21**, 207 (1980).
66. M. H. Chen, “*Relativistic Auger and X-Ray Emission Rates of the  $1s^{2l^n}(2l')^m$  Configurations of Be-Like Ions*”, *Physical Review A* **31**, 1449 (1985).
67. D. W. Savin, S. M. Kahn, G. Gwinner, M. Grieser, R. Repnow, G. Saathoff, D. Schwalm, A. Wolf, A. Muller, S. Schippers, P. A. Zavodszky, M. H. Chen, T. W. Gorczyca, O. Zatsarinny, and M. F. Gu, “*Dielectronic Recombination of Fe XXI and Fe XXII via  $N = 2 \rightarrow N' = 2$  Core Excitations*”, *The Astrophysical Journal Supplement Series* **147**, 421 (2003).
68. D. W. Savin, S. M. Kahn, J. Linkemann, A. A. Saghiri, M. Schmitt, M. Grieser, R. Repnow, D. Schwalm, A. Wolf, T. Bartsch, A. Muller, S. Schippers, M. H. Chen, N. R. Badnell, T. W. Gorczyca, and O. Zatsarinny, “*Dielectronic Recombination of Fe XIX Forming Fe XVIII: Laboratory Measurements and Theoretical Calculations*”, *The Astrophysical Journal* **576**, 1098 (2002).
69. D. W. Savin, E. Behar, S. M. Kahn, G. Gwinner, A. A. Saghiri, M. Schmitt, M. Grieser, R. Repnow, D. Schwalm, A. Wolf, T. Bartsch, A. Muller, S. Schippers, N. R. Badnell, M. H. Chen, and T. W. Gorczyca, “*Dielectronic Recombination (via  $N = 2 \rightarrow N' = 2$  Core Excitations) and Radiative Recombination of Fe XX: Laboratory Measurements and Theoretical Calculations*”, *The Astrophysical Journal Supplement Series* **138**, 337 (2002).
70. H. A. Bethe and E. E. Salpeter, *Quantum Mechanics of One- and Two-Electron Atoms* (Academic Press, New York, 1957).

71. I. P. Grant, “*Gauge Invariance and Relativistic Radiative Transitions*”, Journal of Physics B: Atomic and Molecular Physics **7**, 1458 (1974).
72. J. V. Neumann and E. Wigner, “*Über Merkwürdige Diskrete Eigenwerte*”, Physikalische Zeitschrift **30**, 465 (1929).
73. M. F. Hasoglu, T. W. Gorczyca, K. T. Korista, N. R. Badnell, and S. T. Manson, “*Isoelectronic Trends of Radiative and Auger Rates Along 2<sup>nd</sup>-Row*”, The Astrophysical Journal , (in preparation).
74. M. F. Hasoglu, T. W. Gorczyca, K. T. Korista, S. T. Manson, and N. R. Badnell, “*K-Shell Fluorescence and Auger Transitions for 2<sup>nd</sup>-Row Isoelectronic Sequences*”, The Astrophysical Journal Supplement Series , (in preparation).
75. P. Palmeri, P. Quinet, C. Mendoza, M. A. Bautista, J. Garcia, and T. R. Kallman, “*Radiative and Auger Decay of K-Vacancy Levels in the Ne, Mg, Si, S, Ar, and Ca Isonuclear Sequences*”, The Astrophysical Journal Supplement Series **177**, 408 (2008).
76. C. D. Caldwell, M. G. Flemming, M. O. Krause, P. van der Meulen, C. Pan, and A. F. Starace, “*Near-100 Production of the Excited Be<sup>+</sup> 1s<sup>2</sup>2p Ion from Decay of Be 1s2s<sup>2</sup>2p*”, Phys. Rev. A **41**, 542 (1990).
77. R. F. Reilman and S. T. Manson, “*Photoabsorption Cross Sections for Positive Atomic Ions With Z Equal to or Less Than 30*”, The Astrophysical Journal Supplement Series **40**, 815 (1979).
78. R. Bruch, W. L. Luken, J. C. Culberson, and K. T. Chung, “*K-Shell Binding Energies of B and C*”, Physical Review A **31**, 503 (1985).
79. A. S. Schlachter, M. M. Sant’Anna, A. M. Covington, A. Aguilar, M. Gharaibeh, R. A. Phaneuf, G. Hinojosa, I. Alvarez, C. Cisneros, A. Miller, and B. M. McLaughlin, “*Lifetime of a K-shell Vacancy in Atomic Carbon Created by 1s → 2p Photoexcitation of C<sup>+</sup>*”, Journal of Physics B. **37**, L103 (2002).
80. B. M. McLaughlin, Private Communication, (2007).
81. S. W. J. Scully, A. Aguilar, E. D. Emmons, R. A. Phaneuf, M. Halka, D. Leitner, J. C. Levin, M. S. Lubell, R. Pttner, A. S. Schlachter, A. M. Covington, S. Schippers, A. Miller, and B. M. McLaughlin, “*K-Shell Photoionization of Be-Like Carbon Ions: Experiment and Theory for C<sup>2+</sup>*”, Journal of Physics B. **38**, 1967 (2005).
82. M. F. Hasoglu, D. Nikolic, K. T. Korista, B. M. McLaughlin, and T. W. Gorczyca, “*K-Shell Photoabsorption Studies of the Carbon Isonuclear Sequence*”, The Astrophysical Journal , (in preparation).